THESIS FOR THE DEGREE OF DOCTOR OF PHILOSOPHY

Surface Chemical Characteristics of Chromium-alloyed Steel Powder and the Role of Process Parameters during Sintering

DIMITRIS CHASOGLOU

Department of Materials and Manufacturing Technology
CHALMERS UNIVERSITY OF TECHNOLOGY
Gothenburg, Sweden 2012

Surface Chemical Characteristics of Chromium-alloyed Steel Powder and the Role of Process Parameters during Sintering

DIMITRIS CHASOGLOU

ISBN 978-91-7385-711-6

Doktorsavhandlingar vid Chalmers tekniska högskola
Ny serie nr 3392
ISSN 0346-718X

Department of Materials and Manufacturing Technology
Chalmers University of Technology
SE-412 96, Göteborg
Sweden
Tel: +46 (0) 31 772 1000
Fax: +46 (0) 31 772 1310
www.chalmers.se

Cover: coalescence and agglomeration of oxides enclosed inside a sinter-neck during sintering

Printed by: Chalmers Reproservice
Göteborg, Sweden 2012

«There is no royal road to science, and only those who do not dread the fatiguing climb of its steep paths have a chance of gaining its luminous summits»

-Karl Marx, March 18, 1872

To my family

Surface Chemical Characteristics of Chromium-alloyed Steel Powders and the Role of Process Parameters during Sintering

DIMITRIS CHASOGLOU

Department of Materials and Manufacturing Technology
Chalmers University of Technology

Abstract

Powder Metallurgy (PM) is a cost efficient method suitable for sustainable production of structural parts that have strict dimensional tolerances and complex geometries. It has been a common practice to utilize Ni and Cu as alloying elements in PM steels, but the high and fluctuating prices of Ni and the concerns around it associated with health hazards as well as the difficulty in recycling Cu lead the PM industry to search for effective alternatives such as Cr and Mn. However the use of Cr has been met with scepticism due to its affinity to oxygen which can lead to the formation of stable oxides on the powder surface. Such oxides can act as barriers for the development of sinter necks and as a consequence they are of major importance for the production of structural components through the press-and-sinter route. Thus particular attention is required in order to control the surface chemistry of the powder which is the key factor for the successful sintering and production of PM parts. The research work presented in this thesis was aimed at acquiring fundamental knowledge concerning the surface chemistry of metal powder and how it changes during the heating/sintering stage and finally how and why different process parameters can affect the reduction/oxidation mechanisms and thus the mechanical performance of the sintered part.

High-resolution analytical techniques (scanning electron microscopy with X-ray microanalysis, X-ray photoelectron spectroscopy and Auger nanoprobe analysis) were used to investigate the powder surface characteristics with regard to composition, morphology, size and distribution of surface oxides. It was revealed that the Cr-alloyed powder is predominantly covered by a homogeneous (~6 nm thick) Fe-oxide layer up to ~94% whereas the rest is covered by fine particulate features with size below 500 nm which were rich in strong oxide forming elements such as Cr, Mn and Si. Hence, most of the contacts between the metal particles comprising the compacted powder will be comprised of Fe-oxide rather than the more stable oxides.

Sintering trials on water atomized steel powder grades pre-alloyed with Cr using varying process parameters showed that the most critical stage is during the heating between 800-1000°C due to the risk of enclosure of surface oxide inside the developing inter-particle connections and further transformation of any residual Fe-based oxides into the more stable Cr-Mn-spinels which at elevated temperatures can coalesce into larger agglomerates. The balance between the developed “microclimate” and the mass transport phenomena is the decisive factor for the efficient reduction of the surface oxide and is greatly affected by the existing conditions such as the atmosphere composition and temperature as well as the different process parameters like the heating rate and green density. Provided that proper pre-cautions are taken in this respect, good mechanical performance of the produced component can be achieved.

Keywords: *PM steels, water atomized powder, surface oxides, XPS/AES, depth profiling, surface coverage, HR SEM+EDX, sintering, sintering atmosphere, reduction/oxidation, carbothermal reaction, Cr-Mn-spinel oxides*

Preface

This PhD thesis is based on work carried out in the Department of Materials and Manufacturing Technology at Chalmers University of Technology (Göteborg, Sweden) under the supervision of Professor Lars Nyborg and the co-supervision of Assistant Professor Eduard Hryha. The project is performed in co-operation with Höganäs AB (Höganäs, Sweden). The project as funded by Höganäs AB and KK-Stiftelsen within the framework of CAPE (Centre of Advanced Production Engineering) industrial PhD school.

The thesis consists of an introduction with information regarding powder characterization and a description of aspects related to the surface chemical interactions that take place during sintering. Additionally the following papers are appended:

I. Methodology for Evaluating the Oxide Distribution in Water Atomized Steel Powder
D. Chasoglou, E. Hryha, L. Nyborg
Proceedings of *Euro PM2009 Congress and Exhibition on Powder Metallurgy*, Copenhagen, Denmark, Oct. 12-14, 2009, Vol. 2, pp. 181-186, EPMA, U.K, 2009

II. Effect of Sintering Atmosphere on the Transformation of Surface Oxides during Sintering of Chromium Alloyed Steel
D. Chasoglou, E. Hryha, L. Nyborg
Powder Metallurgy Progress, 2009, Vol. 9(3), pp. 141-155

III. Oxide Distribution in Prealloyed Water Atomized Steel Powder
D. Chasoglou, E. Hryha, L. Nyborg
Proceedings of World PM2010: *Powder Metallurgy World Congress & Exhibition 2010*, Florence, Italy, Oct. 10-14, 2010, Vol. 1, pp.61-69, EPMA, U.K, 2010

IV. Surface Interactions during Sintering of Chromium-alloyed PM Steels in Different Atmospheres
D. Chasoglou, E. Hryha, L. Nyborg
Proceedings of World PM2010: *Powder Metallurgy World Congress & Exhibition 2010*, Florence, Italy, Oct. 10-14, 2010, Vol. 2, pp. 3-12, EPMA, U.K, 2010

V. Effect of Atmosphere Composition on the Surface Interactions during Sintering of Chromium-alloyed PM Steels
D. Chasoglou, E. Hryha, L. Nyborg
Proceedings of *Euro PM2011 Congress and Exhibition on Powder Metallurgy*, Barcelona, Spain, Oct. 9-12, 2011, Vol. 3, pp. 111-117, EPMA, U.K, 2011

VI. Fractographic Investigation of Chromium-alloyed PM Steels Sintered in Atmospheres with Varying Hydrogen Content
D. Chasoglou, E. Hryha, L. Nyborg
Powder Metallurgy Progress, 2011, Vol. 11(1-2), pp. 32-41

VII. Characterization of Surface Oxides on Water-atomized Steel Powder by XPS/AES Depth Profiling and Nano-scale Lateral Surface Analysis
D. Chasoglou, E. Hryha, M. Norell, L. Nyborg
To be submitted to Applied Surface Science

VIII. Surface Chemical Characteristics of Chromium-alloyed Steel Powder and the Role of Process Parameters during Sintering
D. Chasoglou, E. Hryha, L. Nyborg
To be submitted to Materials Chemistry and Physics

Contribution to the Appended Papers

In the research work presented in the appended papers the author's contribution consists of:

- all SEM imaging and EDX analyses with the relevant sample preparation for both powder characterization and fractographic investigations
- performing of all XPS analyses with the subsequent data evaluation and surface coverage calculations as well as the evaluation of the AES data
- all the metallographic investigation with the relevant sample preparation
- carrying out all the interrupted sintering experiments both in the laboratory tube furnace and the dilatometer and performing the thermogravimetric studies
- all the manuscripts of the appended papers were written by the author in close collaboration with my supervisors As. Prof Eduard Hryha and Prof. Lars Nyborg

A summary of the contributions by others in this research is described below:

- The AES analyses were carried out by Doc. Mats Norell
- Preparation of all samples used for the sintering trials, all the O-C bulk chemical analyses and majority of the mechanical testing was done by the laboratory of Höganäs AB, Sweden under the supervision of Dr. Ola Bergman
- Additional mechanical testing was performed at ESAB AB, Sweden

Contents

1 Introduction

The powder metallurgy (PM) process is an established method used today for the large-scale production of precision parts in a cost-efficient manner. The constant demands for improved mechanical properties of the produced structural parts are met with various routes by the PM industry e.g. by carefully introducing alloying elements [1]. Traditionally PM steels were alloyed with Ni, Mo and Cu but the high prices especially of the first two in combination with the health hazards associated with Ni and the difficulties in recycling for Cu lead the PM industry to explore the possibilities of using other alloying elements such as Cr, Mn, V, Si, etc. Especially chromium is considered a very attractive choice since it increases hardenability, it is relatively inexpensive and easily recyclable [2]. Probably the most critical aspect regarding the use of elements such as Cr, Mn and Si today is their high sensitivity to oxygen and thus their ability to form thermodynamically stable oxides.

Powder grades produced with the water atomization technique will be oxidized on the surface due to the reaction with the water vapour. Even after subsequent annealing in an appropriate reducing atmosphere, the surface will still be covered by some surface oxide. Since now the attained mechanical properties depend on the bonding developed between the adjacent metal particles during the sintering cycle. It is easily understood that oxides on the powder surface can act as barriers and thus inhibit the formation of decent inter-particle necks and consequently compromise the desired mechanical performance [3-10].

From the above it is clear that in order to ensure efficient sintering of PM steels containing oxidation sensitive elements it is essential to control the surface chemistry by considering the interactions that will take place with the sintering atmosphere. Therefore the choice and careful control of the sintering atmosphere in terms of composition and purity is one of the main factors that will ensure proper sintering of the oxidation sensitive PM steels [4-6, 10-17]. Furthermore the fundamental knowledge of how and why different process parameters like the heating rate and the green density could affect the reduction/oxidation processes during sintering is essential in order to establish the necessary requirements and create a process map for an efficient sintering. The understanding of the surface related phenomena is therefore of high importance from a technological point as well as from a scientific perspective.

This research deals with the surface characteristics of water atomized steel powders pre-alloyed with chromium. Particular attention was put into investigating the effect of different process parameters on the chemical reactions taking place on the powder surface between the surface products and the sintering atmosphere.

2 Powder Metallurgy

2.1 Brief History and Present Status

Powder Metallurgy (PM) has been one of the oldest established metal processing techniques which dates back several thousands of years[18]. At 3000B.C the inability to melt metals in the furnaces of that age was the driving force for the Egyptians to produce sponge iron powder which in turn was hammered at elevated temperatures in order to weld the powder particles together [18]. We had to reach the 19th century in order for PM to be used in larger scales for the processing of platinum powder. The next big development in the PM industry occurred at the beginning of the 20th century with the use of tungsten powder for the fabrication of filaments used for electric light bulbs and consists of one of the earliest modern applications of PM [19]. At that time several important PM products were produced such as cemented carbides for cutting tools, porous self-lubricating bearings, etc.

The large-scale production of iron powder and respectively of sintered parts started in 1935 and met intensive development in the following decade [20]. From that time and until today the main PM products have been the structural steel components which are used in applications from various fields. However the main field of application is today the automotive industry in which ~70% of the total PM tonnage produced worldwide is used (**Fig. 1**) [21].

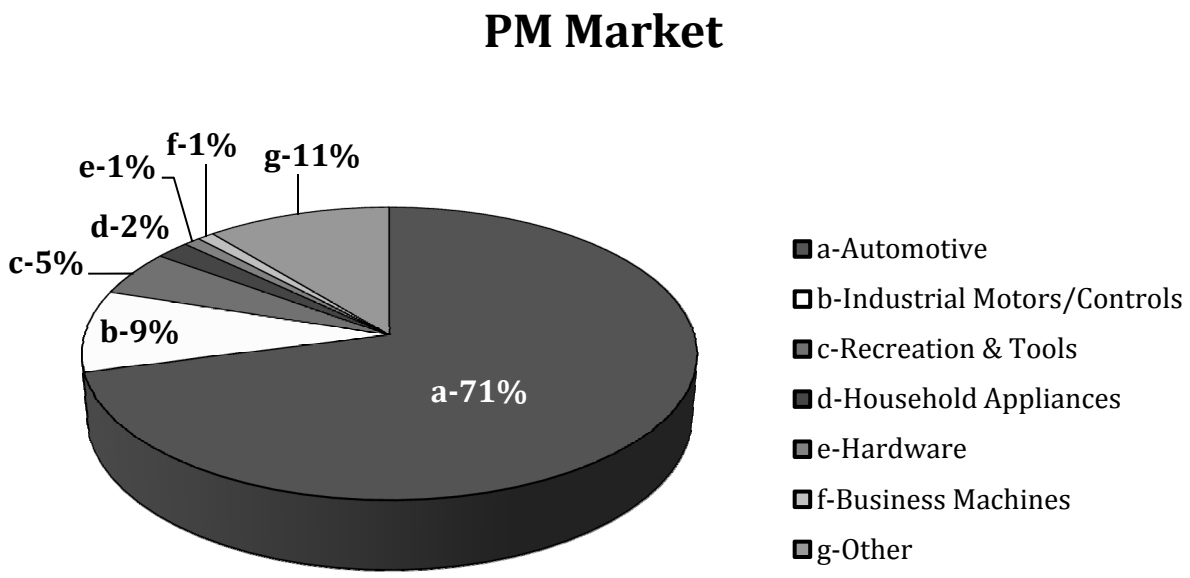

Fig. 1. *Areas of usage of PM structural parts (Source: MPIF).*

2.2 Reasons for using Powder Metallurgy

PM is an attractive choice for the production of metal parts for a number of reasons. It is uniquely versatile process and offers unique capabilities in alloy compositions and microstructural development that is extremely difficult (if not impossible) and costly to obtain with any other traditional metal forming processes. For example in PM it is possible to alloy the material in the solid state and therefore to process metals with very high melting temperatures. Furthermore, the fabrication of metal powder bymeans of atomization gives the possibility to alloy the material in the molten state (pre-alloying) prior to atomization as well as by mixing different kinds of powder. For this reasons PM parts can be manufactured from fabricated powder at temperatures lower than the melting temperature of the metal. This means that segregation or other defects which are associated with casting can be avoided. Hence PM is a particularly suitable process for the development of novel materials with tailored alloy compositions. General examples of such materials are high speed steels, oxide dispersion strengthened (ODS) alloys, hard metals (cemented carbides etc.), porous materials and soft magnetic composites (SMC) [19, 21-23].

One of the main advantages of the PM process route is the possibility to fabricate in a cost-efficient way components of complex geometries, with very good dimensional tolerances at very high productivity rates (**Fig. 2**).

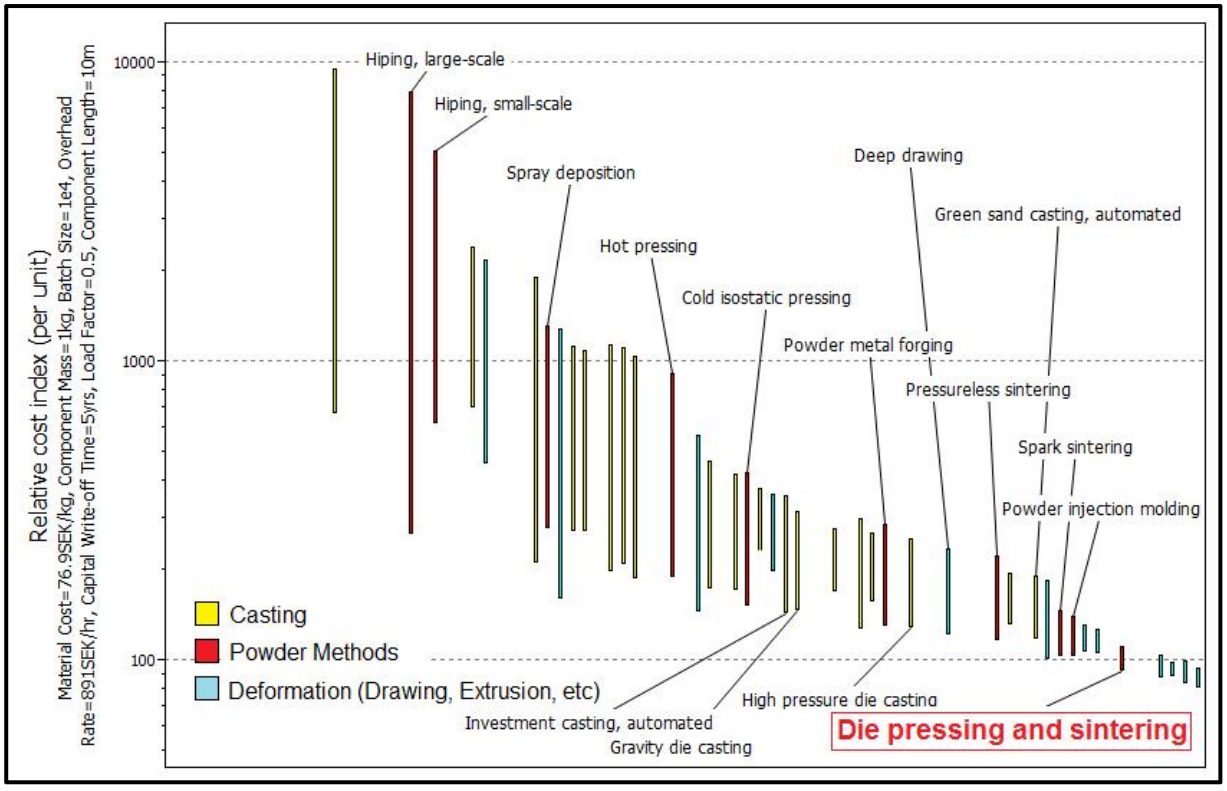

Fig. 2. *Bar chart showing the relative cost for the production of a single component by different processing techniques (Plotted with "CES EduPack 2009" software).*

Since the final PM component after e.g. sintering has basically its final dimensions and shape, further processing is often not required. Therefore the stages involved in the manufacturing of the final component are fewer in comparison with other techniques. As a consequence, the PM route means more efficient raw material utilization as well as

lower energy consumption which in turn relate not only to cost efficiency but also to environmental and sustainability concerns [21, 23]. In **Fig. 3** different metal processing techniques are compared in terms of raw material utilization and energy consumption per kg of finished part [23].

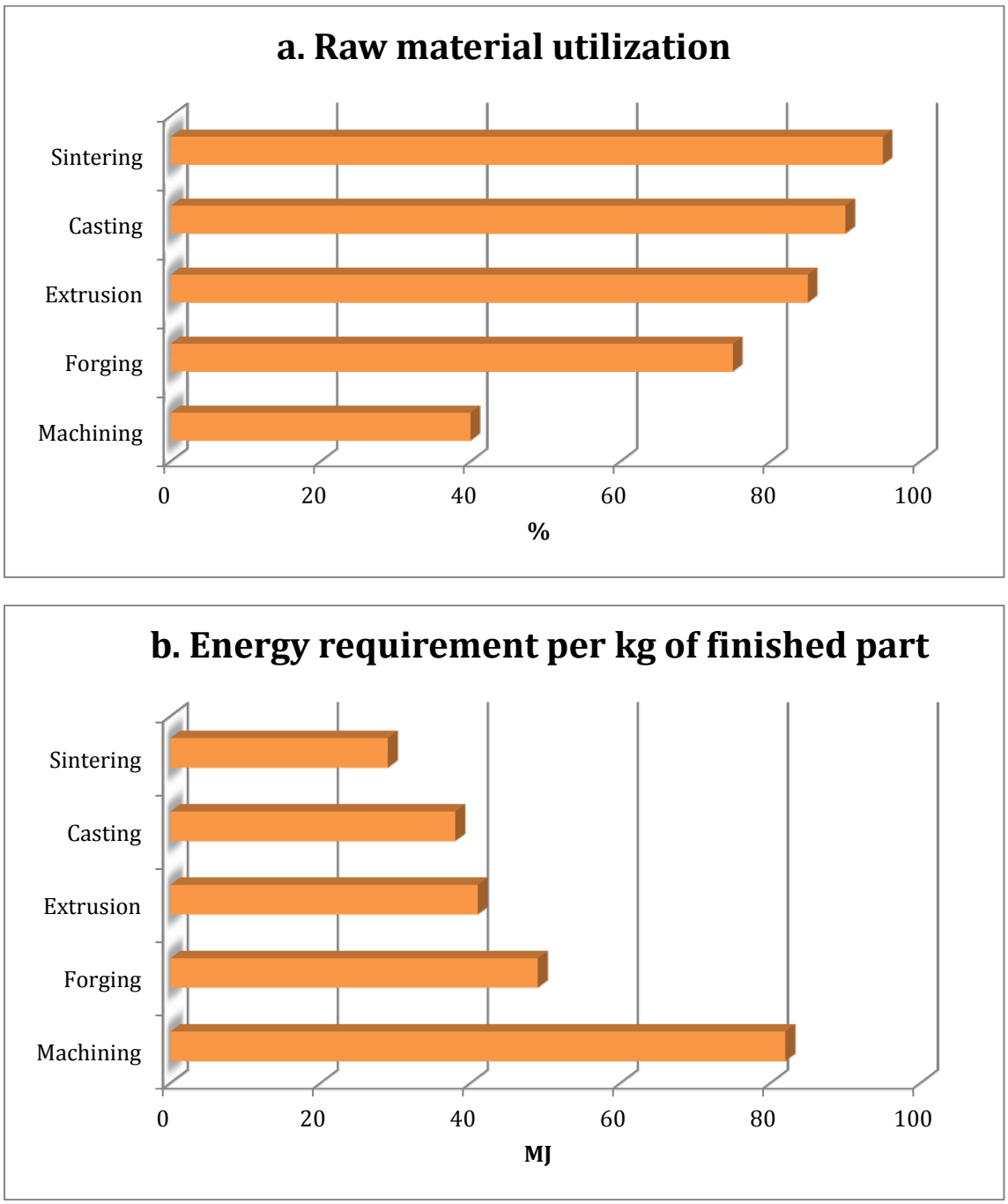

Fig. 3. *Comparison of different metal processing techniques in terms of a) raw material utilization and b) energy requirements (Source: EPMA).*

There are naturally some limitations as well for the PM in comparison with other techniques. For instance there are practical issues for achieving full density parts with the conventional die pressing and sintering. A limiting factor is also the size/weight of the component due to the compaction process stage [1, 19].

Because of the above mentioned aspects, PM research aims towards the improvement of the properties of PM products is very active today with main focus on the minimization of porosity, the optimization of the final microstructure and for the structural applications towards the improved static and dynamic mechanical properties achieved by providing developed and defect-free inter-particle necks.

2.3 The PM Process Route

During the past decades the improvement in quality of steel powder has been dramatic and a large number of powder grades are available today. In the same time the development of the compaction and sintering processes resulted in a more efficient production of PM steel parts that are implemented in a large number of applications. In the following section the stages that make the PM steel process route (**Fig. 4**) are briefly described. Special attention is given to the topics of interest for the purposes of this thesis.

Fig. 4. *Chart of the press & sinter PM process route (Author's illustration).*

2.3.1 Powder Fabrication

Several commercial routes exist today for the production of metal powders and it is possible to divide them in three major categories:

1) mechanical disintegration
2) electrolytic/chemical fabrication techniques
3) atomization techniques with water, oil or inert gas as cooling medium

For the production of steel powder though the dominant production method is the water or gas atomization. During atomization, high pressure water or gas jets hit a molten metal stream and disintegrate it into droplets that are in turn rapidly solidified (**Fig. 5**) [1, 18-20, 22]. Due to this integration into small droplets with high surface-to-volume ratio high cooling rates are obtained. Additionally the pressure of the media used affects the overall cooling rate of the droplets and the significantly higher cooling capacity of water in comparison with gas also has a profound effect on the shape of the produced powder. In general, in the case of water atomization the cooling rate is approximately 10^4-10^6 $K \cdot s^{-1}$ and the metal particles have typically an irregular and rough shape [1, 18-20, 22, 24]. Due to the nature of the fabrication technique the produced powder is oxidized. After drying, subsequent annealing in an appropriate reducing atmosphere is therefore carried out in order to lower the oxygen content of the powder.

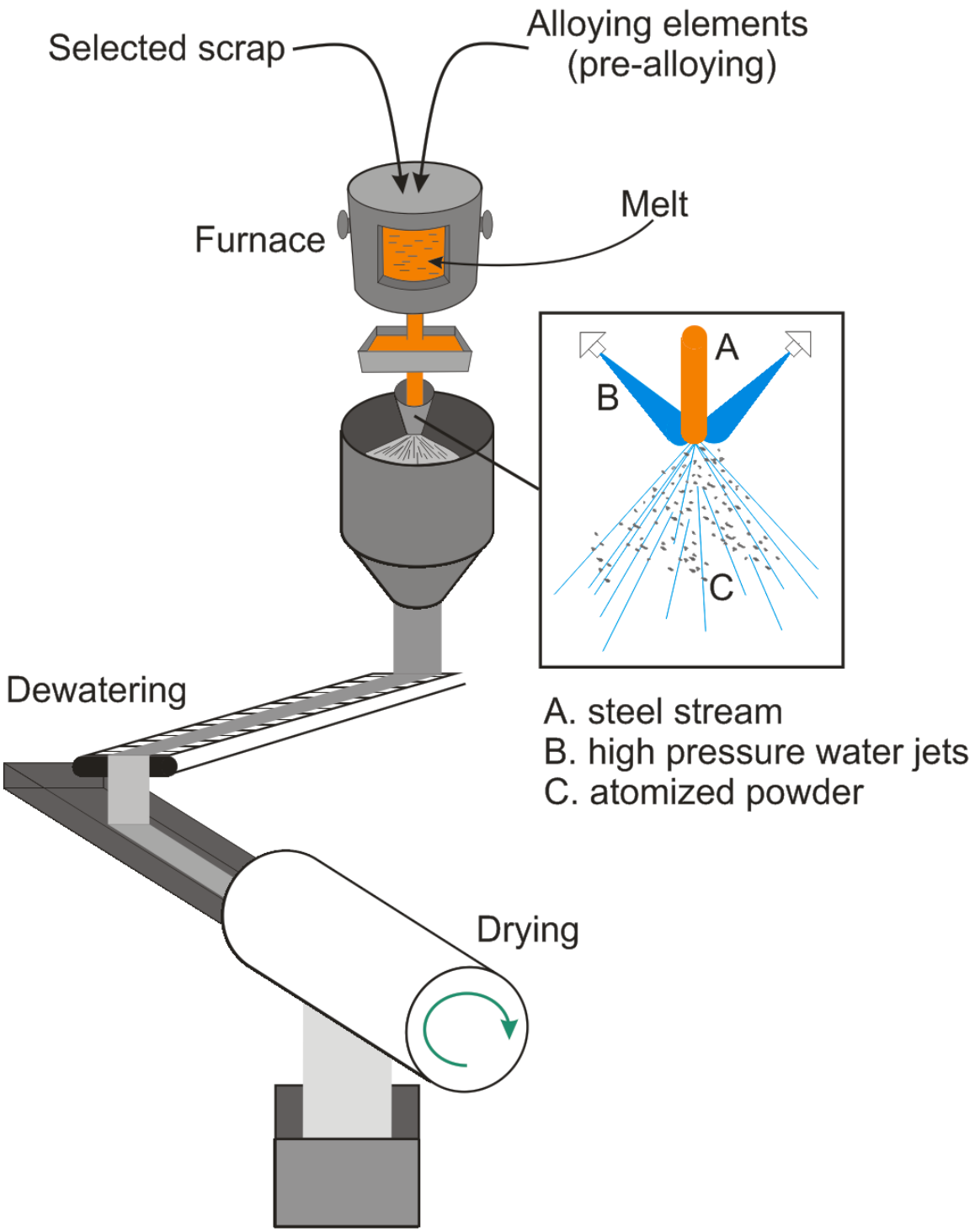

Fig. 5. *Schematic representation of the water atomization process (Redrawn from [22]).*

2.3.2 Alloying Elements and Alloying Methods

It has been a common practice in the metallurgy of steels to introduce alloying elements in order to tailor their microstructure and change their properties [18, 25]. Particularly the PM industry, due to its versatility as a metal part fabrication technique, has been taking great advantage of the incorporation of alloying elements. The enhancement of the properties of PM parts by optimization of the final microstructure is possible by

designing new alloy systems or by tailoring the microstructure development of today's alloys. The introduction of alloying elements in PM parts during the production can be performed in different ways [18-20, 22, 23]:

i) Alloying in the molten state before the water atomization *(pre-alloying)* (**Fig. 5**). The produced powders are homogeneously alloyed which in turn will provide homogeneous composition of the sintered part

ii) Mixing of base powder with elemental powder or ferroalloys *(admixing)*. The actual alloying is taking place during the sintering through diffusion processes. Admixing with graphite is the only way for introducing carbon into ferrous powders

iii) Bonding of additions to an elemental or pre-alloyed powder by metallurgical means. As in mixing, the actual alloying takes place during the sintering stage *(diffusion alloying)*

The choice of the appropriate alloying method depends on the desired final properties as well as on the properties of incorporated alloying elements. For elements such as Cr and Mn the most common technique today is pre-alloying. The reason for this is that these elements have high oxygen affinity and therefore they have a strong tendency towards the formation of thermodynamically stable oxides during the powder production. Thus if Cr and Mn are present in solid solution (as in pre-alloying) their activity is roughly lowered down to their content and the problem of the sensitivity to oxidation can be dealt with up to a certain extend [4, 7, 11, 12, 14, 15, 17, 20, 26-29]. A disadvantage of pre-alloying with Cr and Mn is the possible decrease in compressibility which can be minimized by tailoring the properties of the base powder by introducing small amounts of Cr [30].

This study was focused on water atomized pre-alloyed powder grades. Below, the most common elements encountered in such grades will be presented briefly:

Carbon: In general carbon is the cheapest and most effective alloying element and is of course essential for the production of steel parts. It can be added only as admixed graphite since if added in the pre-alloyed state it increases significantly the hardness of powder particles and thus reduces compressibility. In terms of the properties of the final component, carbon increases the hardness and the strength of the compact. Additionally carbon plays a vital role as a reducing agent in the reduction of the surface oxide during the sintering stage.

Molybdenum: Increases hardenability without reducing the compressibility as drastically as chromium. Molybdenum is suitable when surface hardening processes are required because it promotes the pick-up of some elements. Additionally Mo is a bainite stabilizer since it slows down the reactions rates for transformation.

Silicon: Is also an effective alloying element but due to its high oxygen affinity it is mainly used in small amounts as a de-oxidizer.

Manganese: Is essentially present in all conventional steels. It increases the hardenability of the steel as well as the hardness and strength due to solid solution strengthening. Its effect though is not as pronounced as that of carbons. In combination with chromium and molybdenum, manganese gives the possibility to acquire bainitic structures without any further post sintering heat treatment. Its main drawback is the

high oxygen affinity which as mentioned earlier may lead to the formation of thermodynamically stable oxides.

Chromium: For the systems under investigation, chromium is the main alloying element. Chromium increases the hardenability and at higher temperatures it contributes to increased strength and is often introduced in conjunction with molybdenum. Today chromium is used as a substitute for nickel in alloyed sintered steels due to the high costs and the health concerns associated with the latter. Chromium is also a strong oxide forming element but the oxides formed have lower stability in comparison with the respective manganese oxides.

Chromium-alloyed PM steels can be used when high performance, in terms of mechanical properties, is required. Structural parts such as synchronization hubs and gears are typical applications for the chromium pre-alloyed powder grades [22, 27-29, 31-33].

2.3.3 Compaction and Shaping

In the case of iron or steel powder, a sufficient amount of graphite powder is added during mixing, in order to acquire, after sintering, the desired composition. At this stage, also other substances such as Cu and Ni can be added in powder form. Generally the powder mixes that are ready to be used in the compaction contain additionally an organic substance which is used for lower friction between the metal particles and most of all to provide die-wall lubrication during the compaction step [1, 19, 20, 22, 23].

The next stage in the conventional press-and-sinter route involves the densification of the powder mix, with which an appropriate die is filled, with the help of a configuration (2 or more) of compacting punches that exert high pressures (600-1000 MPa). The application of pressure leads to an inter-locking of the irregularly shaped metal particles along with a degree of cold welding that takes place. A “green compact” is then produced with sufficient strength for further handling until the sintering step [1, 18-20, 22, 23].

2.3.4 Sintering

Sintering is the stage during which metal powder compacts acquire the strength needed to satisfy the requirements existing during their use as engineering components. The strengthening of the compact during sintering occurs with the bonding of adjacent metal particles by atomic diffusion and other mass transport mechanisms. From the above it is clear that the sintering stage is the most important and challenging process from technological point of view, in the production of PM components [1, 19, 20, 22, 23, 34].

The consolidation of the metal powder can take place either by performing a pressureless heat treatment on powder compacts at temperatures below the melting point of the base material (solid-state sintering), by applying, simultaneously, pressure and heat (hot pressing or pressure sintering) or by forming a limited amount of liquid phase (liquid-phase sintering) at systems which involve mixed powders[1, 19, 20, 22, 23, 34]. This work was entirely focused on the phenomena that were taking place during solid-state sintering and thus from now on any reference to the sintering process will regard the solid-state.

The bonding of metal particles occurs through the development of inter-particle necks at the particles contacts. From an energy point of view, a powder (or a porous body) has an excess amount of energy due to the existence of more surface atoms which have "unsatisfied" bonds in comparison with a fully dense and solid body of identical material and mass. Therefore the driving force behind sintering is essentially the minimization of the surface free energy. The mass transport that is required for the bonding of the metal particles takes place through various basic mechanisms [19, 20, 22, 23, 34-36]:

- Surface diffusion
- Evaporation/condensation
- Volume diffusion
- Grain-boundary diffusion
- Viscous or plastic flow

Surface diffusion and evaporation/condensation are naturally related to the mass transport on the surface whereas the rest are associated with the mass transport in the bulk. Surface diffusion is considered in general as a significantly faster process [19, 25, 34] and for ferrous powders it is considered the dominant mass transport mechanism during the heating stage. With increasing temperature generally bulk transport processes and especially volume diffusion are becoming more active [19, 20, 22, 23, 25, 34-36].

During the whole sintering process the most prominent place acting as a material sink is the neck region (**Fig. 6**) due to the large curvature difference between the regions of the metal particle, which in turn leads into large difference in vacancy concentration (a concave surface has higher vacancy concentration than the equilibrium whereas a convex one has lower). That is why the convex part of the powder surface will act as a material source (or vacancy sink) and a concave part such as the neck will act as a material sink (or vacancy source) [19, 22, 23, 25, 34-36].

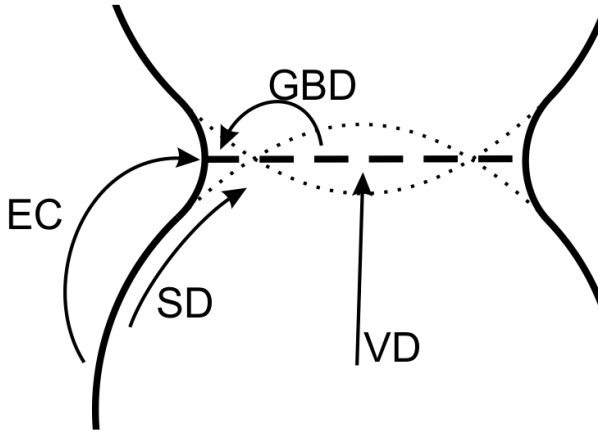

Fig. 6. *Mass transport processes in the neck region: EC) Evaporation-Condensation, SD) Surface Diffusion, VD) Volume Diffusion, GBD) Grain Boundary Diffusion (Author's illustration).*

With respect to time, the sintering process can be divided into three stages (**Fig. 7**). The characteristic of the initial stage is the formation and growth of inter-particle necks during a non-isothermal heating [19, 20, 22, 34]. During this stage surface diffusion is more enhanced compared to the other transport mechanisms. As soon as the sintering temperature is reached an isothermal dwelling at this temperature is carried out. The intermediate stage is characterized by pore rounding, grain growth and sometimes densification. Surface transport is still active during this stage and if densification takes

place, this is accomplished by volume and grain boundary diffusion [19, 20, 22, 34]. The final stage consists of the pore isolation and spherodization by bulk diffusion. It should also be noted that phenomena taking place during the intermediate and final stages can only be active on local scale in the normal sintering of ferrous powder at the inter-particle contacts developed between the irregular water-atomized metal particles. Normally there is hardly any shrinkage and the porosity level is basically set by the extent of prior powder compaction.

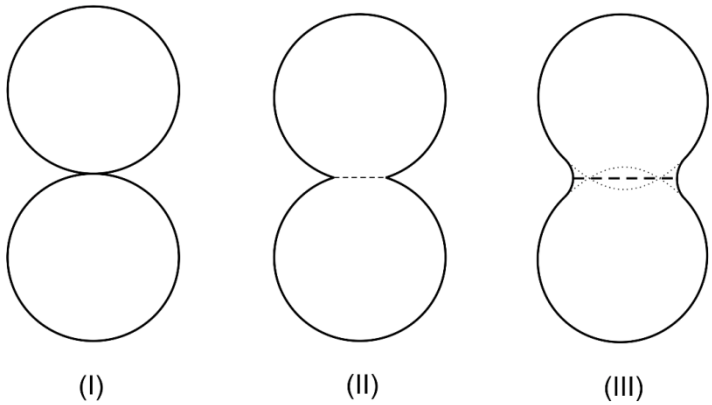

Fig. 7. *Model of sintering of two spherical particles: I) after compaction, II) initial stages of sintering with neck formation, III) intermediate and final stage (Author's illustration).*

Generally it is difficult to distinguish between the different stages, especially between the intermediate and final stage. However it is essential to evaluate the efficiency of the processes related to the neck formation and growth in correlation with the applied conditions which will determine the final properties of the sintered body. The inter-particle neck formation and growth can be efficiently evaluated by examining the fracture surfaces of processed and tested specimens [20, 37, 38]. Therefore in this study great focus was given in performing fractographic investigations on samples processed in different conditions (see also section 5.3).

Practical considerations and factors influencing the properties of sintered components

A typical sintering operation taking place in a continuous sintering furnace can be divided into three stages (**Fig. 8**):

i) *Heating stage:* the compacts are reaching the desired sintering temperature with an appropriate heating rate. During this stage the lubricant which was added in the mixing burns off (de-lubrication). Proper de-lubrication is essential for the production of good quality parts [39, 40]. After de-lubrication, surface oxides are reduced and inter-particle necks are beginning to form. Graphite dissolution is taking place during this stage as well.

ii) *Sintering stage:* the parts are held at the constant temperature (isothermal holding) for sufficient time in order for the bonding of the metal particles to take place and consequently the desired mechanical properties to be obtained.

iii) *Cooling stage:* the sintered parts are cooled down to room temperature with an appropriate cooling rate which will determine the final microstructure of the material.

In **Fig. 8** a typical continuous mesh belt furnace is shown. This type of furnace is commonly used for the production of high volumes of structural parts at temperatures of up to 1150°C. Other types of furnaces exist that can operate at higher temperatures but normally with lower production outputs.

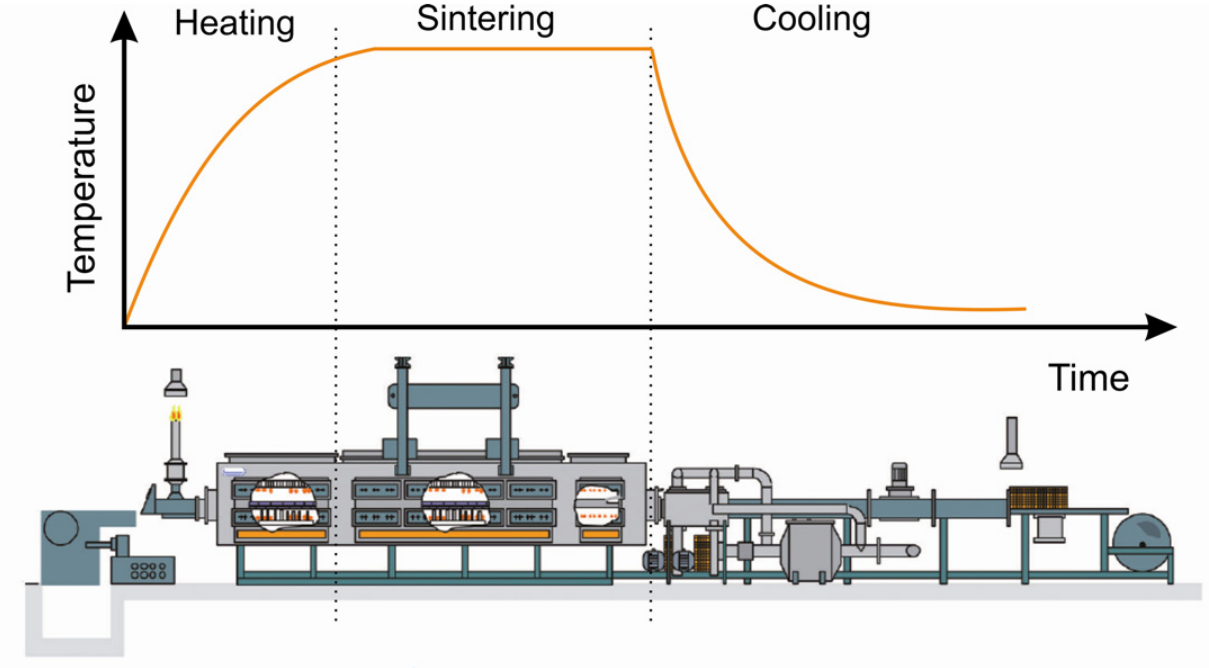

Fig. 8. *Characteristic sintering process for PM parts and correlation with a continuous mesh belt sintering furnace (Redrawn from [41]).*

It has been made clear until now that the sintering of PM parts is a very complicated and challenging process which can be greatly affected by a number of factors. Below some of these factors which are also related to this study will be briefly presented:

Sintering temperature and time

Since the bonding of metal particles in a compact is directly related to the mass transport mechanisms that take place, it can be easily understood that increased sintering temperature will increase the diffusion rates which in turn will enhance the strength of the inter-particle bonds with a direct effect on the mechanical properties of the consolidated material [6, 8-10, 12, 26, 27, 33, 42-44]. Additionally larger sintering temperatures can ensure, from thermodynamic point of view, the reduction of more stable oxides which could obstruct neck formation and growth (see also Chapter 3). Experimental data are plotted in **Fig. 9** showing the dependence of sintering temperature on the mechanical properties (in this case impact energy) of sintered specimens. Naturally other mechanical properties will be also affected by the sintering temperature as shown in the literature [9, 10, 12, 33, 45, 46].

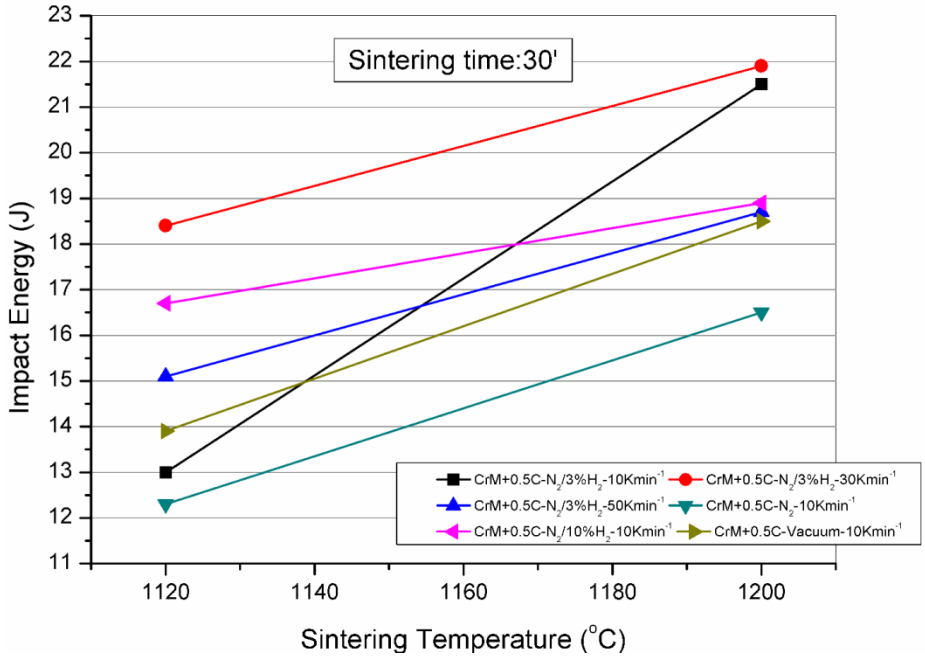

Fig. 9. *Impact energy of AstCrM+0.5%C sintered for 30' at different temperatures and conditions (Author's experimental results).*

Considering the diffusion processes that take place during sintering it is established that the total amount of atoms that diffuses into the neck area at a given temperature will be directly dependent on the time spent on that temperature. Therefore longer sintering times will result in stronger inter-particle connections and thus improved mechanical properties (**Fig. 10**).

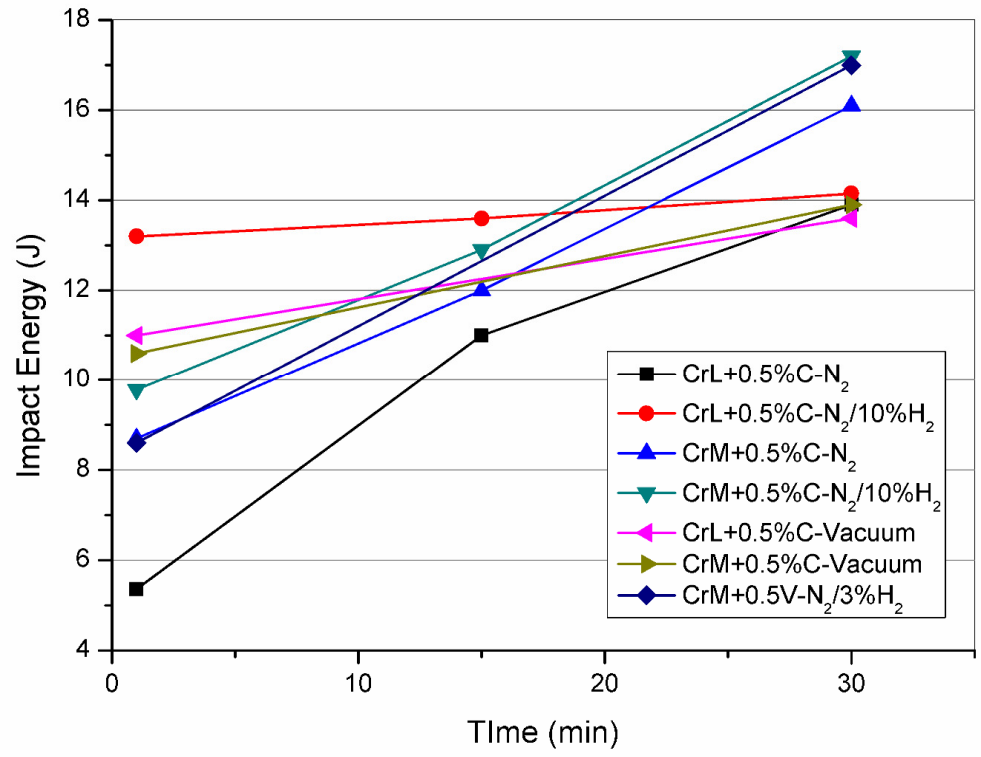

Fig. 10. *Impact Energy as a function of the sintering time for samples of different pre-alloyed grades sintered at 1120°C in different conditions (Author's experimental results).*

Sintering atmospheres

The presence of a suitable sintering atmosphere is of vital importance in the production of PM components [1, 3-7, 9-17, 19, 20, 22, 31, 41-43, 47-57]. The specific functions of the atmosphere during the sintering process are:

- To protect the compact from oxidation
- To assist in the reduction of the surface oxide in order for inter-particle contacts to be developed
- To ensure that proper de-lubrication takes place
- To prevent carburization/decarburization of the compact

Especially in the case of oxidation sensitive PM steels the choice and careful control of the sintering atmosphere in terms of composition and purity [4-6, 10-17] is of paramount importance in order to control the surface chemistry. Hence it is crucial to consider the interactions that will take place between the different gas species and the component and their dependence of the applied temperature. The importance of the above is particularly significant for the processing of PM steels i.e. in comparison with the heat treatment of "bulk" steels since [17]:

- the applied temperatures are significantly higher which in turn results in the occurrence and evolution of chemical reactions on the surface
- additionally high temperature results in increased chemical reaction speeds as well as accelerated mass transport phenomena
- the surface area in the case of PM steels is higher by 10^3-10^4 times due to the porosity of the parts which in turn will further enhance the reaction rates

In the overall process the flow must be adjusted accordingly to prevent air from entering the furnace or to prevent the lubricant decomposition products to enter the sintering zone.

Today there are different types of atmospheres used for the sintering process with the material being the determining factor for the choice of the proper one [1, 4, 11, 17, 19, 20, 22, 41]. The main categories and gases used are:

- Pure gases
    - Hydrogen (H_2) – is the most commonly used pure active gas due to its reducing effect. The danger of explosion and its high cost are issues that need to be considered with its use.
    - Nitrogen (N_2) – is basically an inert gas and can be used in sintering due to its high purity and low price. More often though nitrogen is used for the dilution of more expensive and reducing gases like H_2 and CO. These blends are suitable for steels containing elements sensitive to oxidation such as chromium and manganese. Nitrogen is also used nowadays in modern furnaces for rapid cooling.
- Dissociated ammonia – contains high amounts of hydrogen (~75%) and thus has high reducing activity. Important disadvantage with this gas is its high content of water vapor, therefore if not dried it can be highly decarburizing.

Other drawbacks with dissociated ammonia are connected to environmental and safety issues.

- Gases produced from burning of hydrocarbons – Careful attention must be given in order to have the proper "carbon potential" and generally to have good carbon control. Sintering of steels containing strong oxide forming elements is impossible because the conditions when using such types of gases are highly oxidizing.
    - Endogas – endothermic burning of hydrocarbons – higher content of reducing species (CO and H_2)
    - Exogas – exothermic burning of hydrocarbons – more oxidizing than endogas due to higher amount of produced CO_2 and water vapor
- Vacuum – sintering in vacuum is performed when oxidation sensitive materials are used and offers very good conditions in terms of protection from oxidation and reduction of oxides (due to the very low oxygen partial pressure). The main disadvantage is that it is a slow and therefore costly process although today large vacuum furnaces with capabilities of production in high volume outputs exist.

More details on thermodynamic issues and reactions occurring during the sintering process which are associated with the sintering atmosphere will be given in Chapter 3.

Green density

A number of studies [26, 28, 42, 58, 59] has shown that increasing the compaction pressure and consequently the green density results in improvement of mechanical properties such as impact energy, tensile strength and hardness of the sintered part (**Fig. 11**). Elongation as well as fatigue strength also benefit from increasing green density up to a certain level but densities above that level will have a negative impact on the afore mentioned properties. The increase in mechanical performance can be attributed to the larger amount of initial contact points and consequently sinter necks between the adjacent metal particles [42]. Furthermore increasing green density has a direct effect on the porosity of the compacted and afterwards sintered part. With increasing density the pore structure changes from open and interconnected to more close and isolated. This in turn of course has a positive impact on the mechanical performance of the material but in the same time it could create implications for the interaction of the sintering atmosphere with the powder surface such as difficult atmosphere penetration, insufficient removal of reduction products [42, 60].

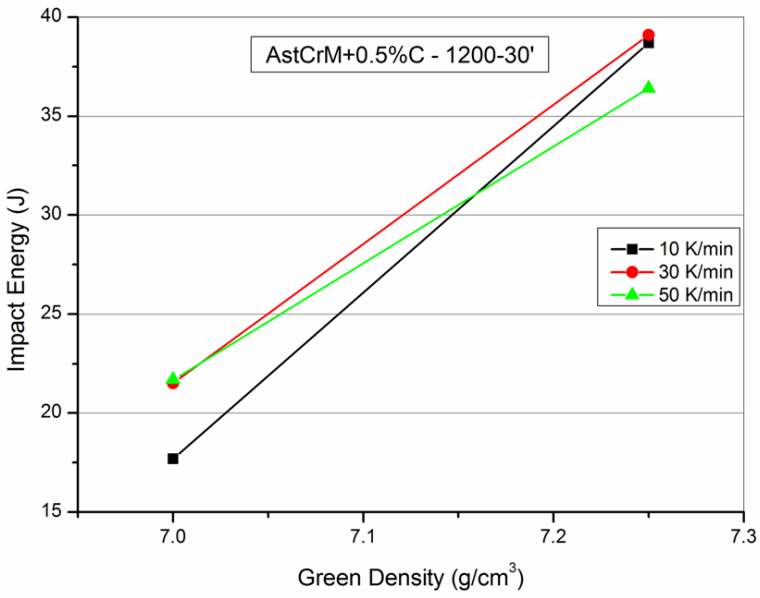

Fig. 11. *Impact energy as a function of green density for AstCrM+0.5%C samples sintered at 1200°C for 30' in N_2/3%H_2 atmosphere with different heating rates (Author's experimental results).*

3 Theoretical Considerations

From the description of the sintering process given in the previous section it becomes clear that the surface of the powder is the key aspect for the efficient consolidation of PM materials. Consequently it is of paramount importance to control the surface chemistry of any features observed on the powder surface and their interaction with the present sintering atmosphere in given conditions. In the next sections some theoretical considerations that are relevant to the aspects of interest of this study will be presented in a more detailed and analytical manner.

3.1 Surface Oxides on Metal Powder and Effect on the Mechanical Properties of Sintered PM Steels

Due to the nature of the water atomization technique as a metal powder production method, the interaction of molten metal droplets with water vapour or steam will lead to the oxidation of the powder fabricated. Thus the initial surface oxide layer which is formed (**Fig. 12**) must be reduced and thus the produced metal powder, after drying, undergoes a subsequent annealing treatment in a reducing atmosphere. However since the powder has very large specific surface area it is very reactive [61] and therefore a thin surface oxide layer will be formed even during handling [54, 61-71].

Studies by Karlsson et al. [54, 61] on water atomized chromium pre-alloyed steel powder showed that the surface of the powder was covered by a thin (6-7nm) Fe-oxide layer and some particulate oxide features of larger size (>100nm) which were rich in strong oxide forming elements such as Cr, Mn and Si. The proposed model as was investigated and revised in this study is shown in **Fig. 13** [54, 61-63].

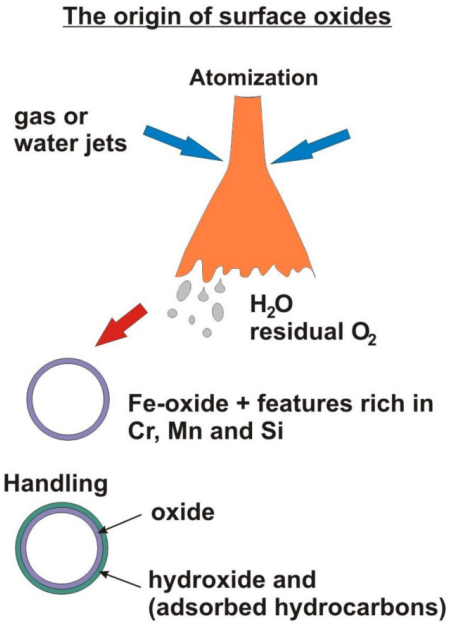

Fig. 12. *Schematic representation of the origin of the surface oxides (Author's illustration).*

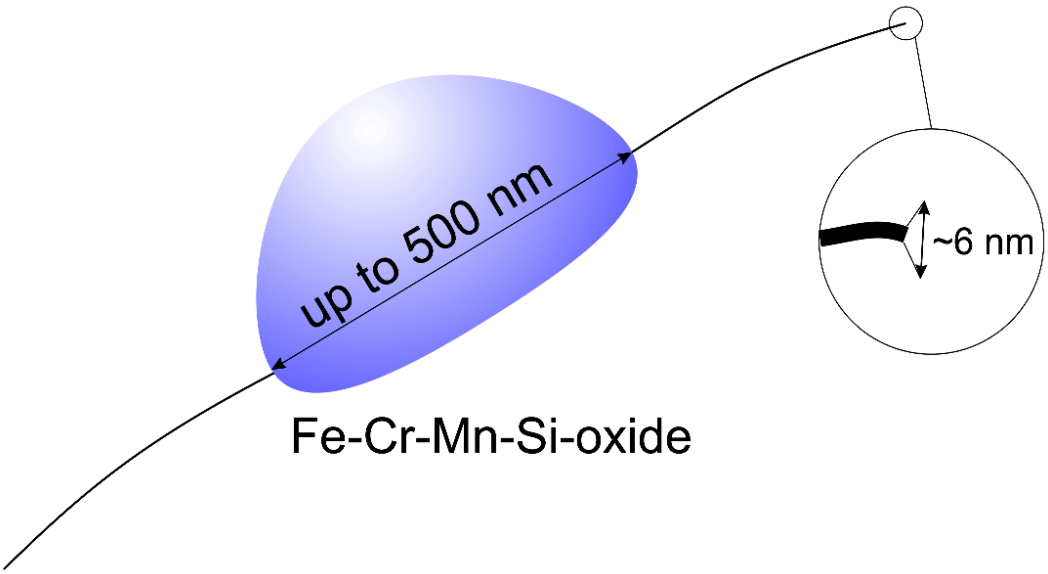

Fig. 13. *Schematic representation of the proposed model of the surface oxide covering the metal particle (Author's illustration).*

The surface oxide on the powder particles will act as a barrier and hinder the mass transport phenomena occurring during the sintering process which in turn will have a retarding effect on the sinter neck development and thus play a role on achieving the desired final properties of the component (**Fig. 14**) [4, 7, 9, 10, 13, 15, 19, 20, 36, 49, 52, 64, 72]. Therefore it is of paramount importance to reduce the surface oxide, at least partially in the inter-particle contact area, in order to enable the onset of sintering.

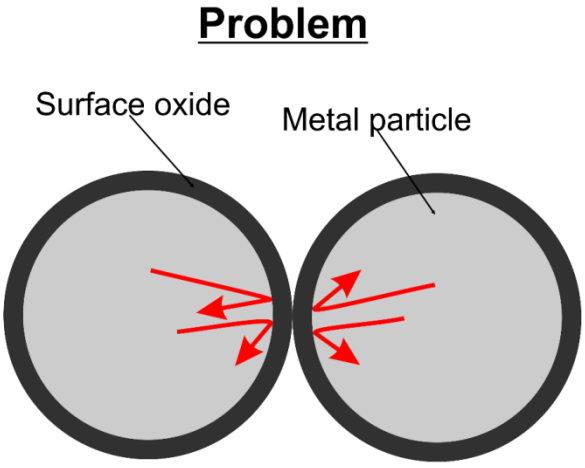

Fig. 14. *The problem created from the presence of surface oxide layer on metal particles (Author's illustration).*

From the above it was made clear that the presence of a surface oxide layer can create significant implications in attaining the desired mechanical performance from a sintered part. It will be demonstrated in the following chapters as well as in the results of this research that the thin (~6 nm) surface Fe-oxide can be easily reduced. On the other hand more stable oxides such as the ones shown in **Fig. 13** could be enclosed in the neck region and have a serious effect especially on the ductility and fatigue properties of the sintered component [73, 74]. This is also illustrated in **Fig. 15** where the impact energy of samples sintered at 1200°C for 30' is plotted versus their oxygen content. In **Fig. 15**

the amount of observed inclusions is increasing with increasing oxygen content even though the total oxygen content for each sample cannot be attributed entirely to oxide inclusions. In the next paragraph a very brief introduction will be given on the effect of the presence of secondary phases (such as the stable oxides mentioned above) on the fracture of sintered steels.

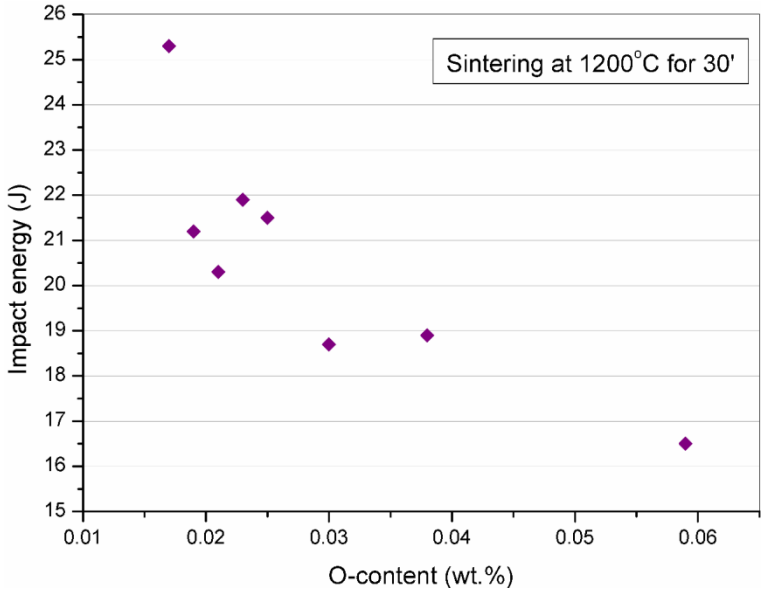

Fig. 15. *Impact energy versus the oxygen content of samples sintered at 1200°C for 30' (Author's experimental results).*

In general fracture will be induced by small particles of sub-micron size when the material is under continuous loading. These particles are not as easily deformed as the surrounding matrix and thus they lose their coherence with the latter when intensive plastic flow is occurring in their vicinity [38, 74, 75]. This results in the formation of tiny voids which in turn will grow and coalesce until final separation takes place (**Fig. 16**). The necking which takes place between the small particles is of the micro-scale and thus the resulting elongation remains small [38, 74, 75]. Consequently the number, the size, the distance and distribution of second phase particles will affect significantly the fracture toughness (K_{Ic}) and the elongation to fracture (ε_f) [74, 75].

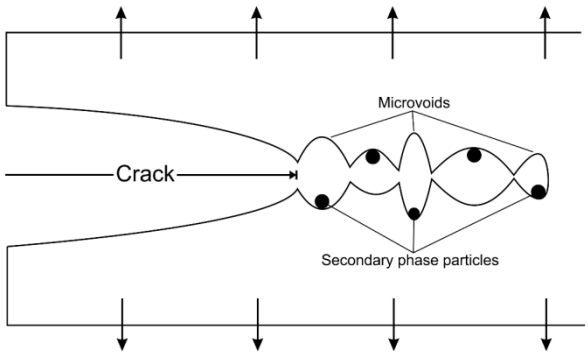

Fig. 16. *Effect of secondary phase particles and dimple formation during ductile crack propagation (Redrawn from [74]).*

3.2 Thermodynamic Description and Stability of Oxides

As mentioned earlier the key factor of the process that essentially controls the surface chemistry and its changes is the sintering atmosphere in terms of both composition and purity.

The chemical reactions of interest, which will be described in the next section, generally take place under constant temperature and pressure and thus for their thermodynamic description, the Gibbs free energy (G) must be considered which by definition is:

$$G = H - TS \quad (1)$$

Therefore at constant temperature and pressure the only reactions that can occur spontaneously are the ones in which the change in Gibbs free energy (ΔG) is negative (**Eq. 2**). Consequently the more negative is the change in the Gibbs free energy, the stronger the tendency for a reaction to take place.

$$\Delta G = \Delta H - T\Delta S \quad (2)$$

The above is a general expression for the criteria of equilibrium condition in a system. It is possible to derive the "standard[1] Gibbs free energy change" ΔG^0 [76] which can then be used as a measure of the thermodynamic stability of certain compounds such as metal oxides and consequently the potential for reduction/oxidation reactions to take place under defined conditions during the sintering process [4, 11, 17, 76, 77].

In the absence of a reducing agent the oxide reduction is occurring through its dissociation according to:

$$\frac{2}{y} Me_x O_y = \frac{2x}{y} Me + O_2 \quad (3)$$

Where Me and Me_xO_y denote the metal and its oxide respectively. Now since the standard Gibbs free energy change is basically:

$$\Delta G^0 = \sum G^0_{(reaction\ products)} - \sum G^0_{(reactants)} \quad (4)$$

Then if **Eq. 3** is considered then the standard Gibbs free energy change becomes:

$$\Delta G^0_1 = \frac{2x}{y} G^0(Me) + G^0(O_2) - \frac{2}{y} G^0(Me_x O_y) \quad (5)$$

A reaction is characterized by the equilibrium constant K which is related to the change in standard Gibbs free energy:

$$\Delta G^0 = -RTlnK \quad (6)$$

Where R is the gas constant ($R=8.314 J \cdot mol^{-1}K^{-1}$) and T is the temperature in Kelvin. In the case of **Eq. 3** the equilibrium constant is given by:

$$K = \frac{a^{\frac{2x}{y}}(Me) \cdot a(O_2)}{a^{\frac{y}{2}}(Me_x O_y)} \quad (7)$$

[1] The standard state of the component of a system is chosen as being the pure component in its stable state at the pressure and temperature of interest and is basically a reference state to which the component in any other state is compared

Where α are the activities of the substances which take part in the reaction. The activity is defined as the ratio between the vapor pressure of a substance in a given condition divided by the vapor pressure of the pure substance under the same conditions. For pure solid or liquid substances the activity is unity whereas for ideal gases the activity is equal to their partial pressures [11, 17]. From the above **Eq. 7** becomes:

$$K = p(O_2) \qquad (8)$$

And by combining **Eq. 6**, **7** and **8** we get:

$$\Delta G_1^0 = -RTln[p(O_2)] \leftrightarrow p(O_2) = exp\left(-\frac{\Delta G_1^0}{RT}\right) \qquad (9)$$

In essence **Eq. 9** describes the temperature dependence of the equilibrium oxygen partial pressure between metal/metal oxide and atmosphere. **Fig. 17** illustrates the above for some oxides of interest. The equilibrium data were calculated using thermodynamic software (HSC Chemistry 7.1). Below each curve in **Fig. 17** the oxide is reduced to its respective metal whereas above the opposite reaction takes place – metal oxidizes to its respective oxide. Therefore **Fig. 17** can be read in two ways:

- By lowering the oxygen partial pressure accordingly it is possible to dissociate an oxide at a chosen temperature
- By increasing the temperature it is possible to dissociate an oxide at lower oxygen partial pressures

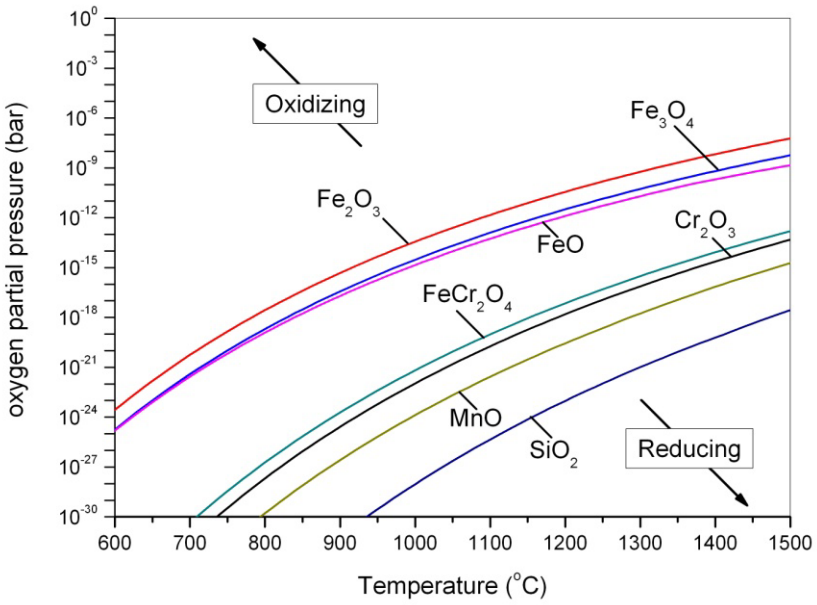

Fig. 17. *Equilibrium oxygen partial pressure of some oxides (Plotted with HSC Chemistry 7.1).*

These points of course are relevant to the thermodynamic stability of the oxide under consideration. It is clear that more stable oxides require significantly lower oxygen partial pressures and higher temperatures in order for their dissociation to occur. At intermediate temperatures i.e. during the heating stage the existing conditions are not sufficient for the reduction of those stable oxides. Considering the above, sintering in vacuum in combination with other reducing mechanisms (see next section) could provide reducing conditions even for stable oxides. On the other hand, vacuum sintering is considered a costly option and is used basically for the production of expensive PM parts i.e. hard metals and not for conventional PM steels nowadays [4, 11, 17, 76, 77].

3.3 Reduction/Oxidation Processes during Sintering

In the previous section the general reduction reaction through dissociation of an oxide was described and the issues related with the usage of vacuum as a sintering atmosphere condition were mentioned. Therefore the use of a suitable sintering atmosphere, which will enable the reduction of stable oxides, is beneficial from both economic and metallurgical points of view. Such sintering atmospheres contain reducing agents like hydrogen and carbon monoxide, the latter being a product of the carbothermal reaction taking place due to the presence of admixed graphite or a component of the processing atmosphere. The reduction by hydrogen is given by [3-7, 9, 11, 13-16, 47, 48, 50-52, 55, 76-79]:

$$\frac{2}{y}Me_xO_y + 2H_2 = \frac{2x}{y}Me + 2H_2O \qquad (10)$$

If now we work in the same way as for **Eq. 3** the equilibrium constant for **Eq. 10** will be:

$$K = \frac{\alpha^{\frac{2x}{y}}(Me)\cdot a^2(H_2O)}{\alpha^{\frac{2}{y}}(Me_xO_y)\cdot\alpha^2(H_2)} \rightarrow K = \frac{p^2(H_2O)}{p^2(H_2)} \qquad (11)$$

Consequently the equilibrium between oxidation and reduction in hydrogen-containing atmospheres is given by:

$$\frac{p(H_2O)}{p(H_2)} = exp\left(\frac{\Delta G_2^0}{2RT}\right) \qquad (12)$$

Where ΔG_2^0 is the Gibbs free energy change for the oxide reduction by hydrogen:

$$\Delta G_2^0 = \frac{2x}{y}G^0(Me) + 2G^0(H_2O) - \frac{2}{y}G^0\left(Me_xO_y\right) - 2G^0(H_2) \qquad (13)$$

Considering **Eq. 12** it is possible to plot the equilibrium partial pressure ratio of hydrogen and water vapour content as a function of temperature (**Fig. 18**). In the diagram of **Fig. 18** above each curve the oxide is reduced whereas below each curve the metal is oxidized.

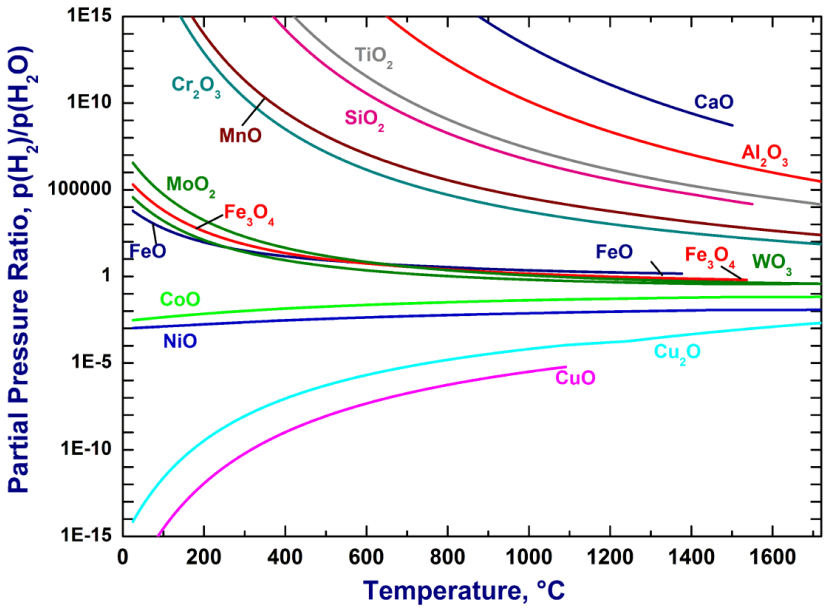

Fig. 18. *Equilibrium partial pressure ratio of hydrogen and water vapour for some metal-oxides systems (Plotted with HSC Chemistry 7.1).*

The powder mixes which are used in the production of PM steel parts contain carbon in the form of admixed graphite. Carbon participates in the oxide reduction in essentially two stages. The first involves the reduction of surface oxides which are in contact with graphite during the heating stage. This reaction is the so called direct carbothermal reduction (**Re. 14**). The produced carbon monoxide can further react with the existing oxides towards the formation of carbon dioxide (**Re. 15**). This reaction in turn is called indirect carbothermal reduction [3-7, 9, 11, 13-16, 47, 48, 50-52, 55, 76-79].

$$\frac{2}{y}Me_xO_y + 2C = \frac{2x}{y}Me + 2CO \qquad (14)$$

$$\frac{2}{y}Me_xO_y + 2CO = \frac{2x}{y}Me + 2CO_2 \qquad (15)$$

The direct carbothermal reduction commences in accordance with **Re. 14** when the temperature is high enough in order for the graphite to become more active. Above ~700°C the presence of CO is ensured due to the Boudouard (**Re. 16**) which favours the formation of CO at high temperatures:

$$C + CO_2 \leftrightarrow 2CO \qquad (16)$$

A large amount of studies has shown that the main reducing mechanism is the indirect carbothermal reaction [3-7, 9, 11, 13-16, 47, 48, 50, 52, 55, 76-79]. The equilibrium constant for **Re. 15** becomes:

$$K = \frac{\alpha^{\frac{2x}{y}}(Me)\cdot a^2(CO_2)}{a^{\frac{2}{y}}(Me_xO_y)\cdot \alpha^2(CO)} \rightarrow K = \frac{p^2(CO_2)}{p^2(CO)} \qquad (17)$$

And the equilibrium between oxidation and reduction in atmospheres containing carbon monoxide is given by:

$$\frac{p(CO_2)}{p(CO)} = exp\left(\frac{\Delta G_3^0}{2RT}\right) \qquad (18)$$

Where ΔG_3^0 is the standard Gibbs free energy change for the oxide reduction by carbon monoxide:

$$\Delta G_3^0 = \frac{2x}{y}G^0(Me) + 2G^0(CO_2) - \frac{2}{y}G^0\left(Me_xO_y\right) - 2G^0(CO) \qquad (19)$$

In a similar manner as before it is possible to plot the equilibrium between the metal, oxide and the partial pressure ratio CO/CO_2, see **Fig. 19**. Again above each curve the oxide is reduced and below the metal is oxidized.

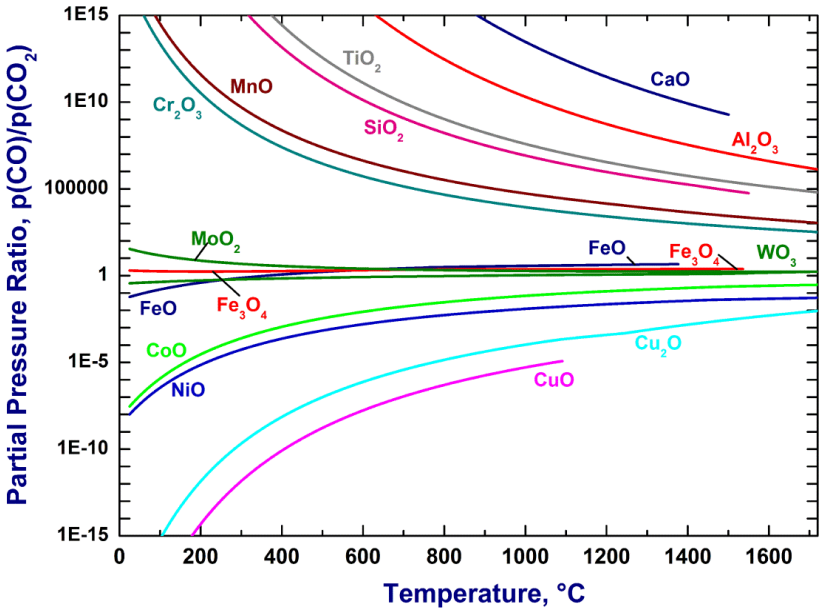

Fig. 19. *Partial pressure ratio of CO and CO_2 in equilibrium with metal oxides (Plotted with HSC Chemistry 7.1).*

All the above review information is summarized in an Ellingham-Richardson diagram (**Fig. 20**) where the standard Gibbs free energy change *(ΔG^0)* is plotted as a function of temperature and the equilibrium conditions can be determined with respect to the pressure balance of the existing gas species: $p(O_2)$, CO/CO_2 and H_2/H_2O.

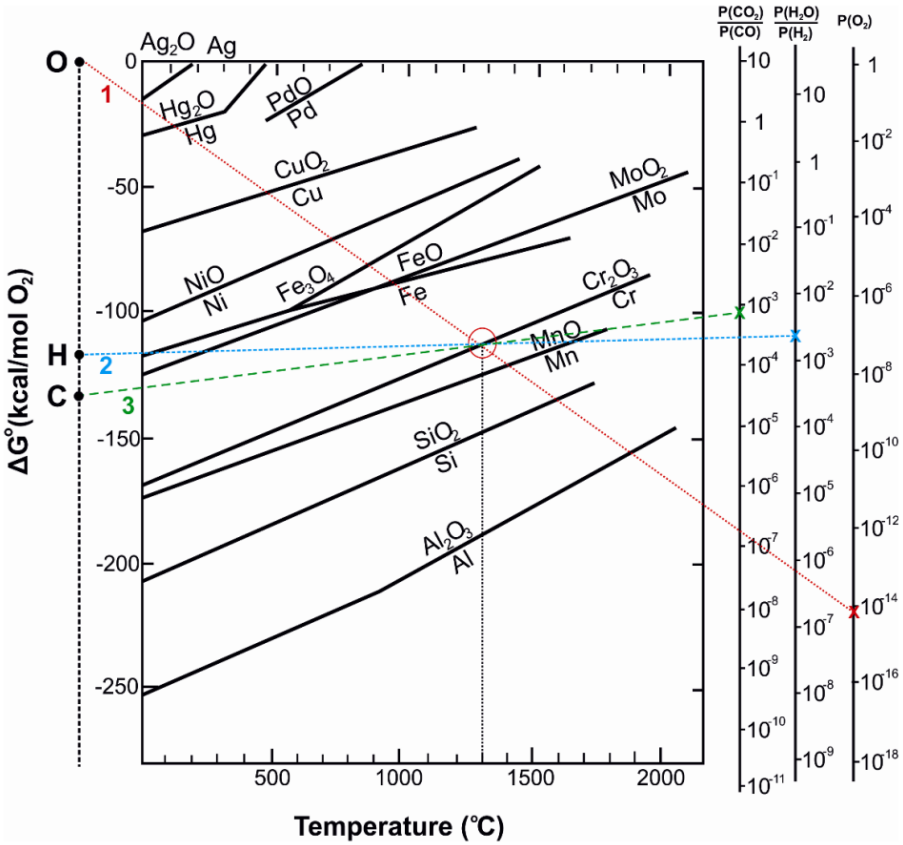

Fig. 20. *Ellingham-Richardson diagram for selected oxides (Redrawn from [22]).*

In order to calculate the critical oxygen partial pressure for a specific oxide (e.g. Cr_2O_3) at a given temperature, a line (line 1-red in **Fig. 20**) can be drawn from the point "O" to the ΔG line of the oxide of interest at the relevant temperature and then by continuing until reaching the $p(O_2)$ axis on the right hand side of the diagram. The intersection with the $p(O_2)$ axis gives the critical pressure for the reduction of the oxide of interest. The same procedure can be followed in order to estimate the critical partial pressure ratios of H_2/H_2O (line 2-blue) and CO/CO_2 (line 3-green) but in these cases the lines must be drawn from points "H" and "C" respectively and then regard the intersections with the relevant axes. [11, 15, 17, 22, 76, 77, 80].

As mentioned in the previous chapter, due to the high cost of using pure reducing atmospheres, it is a common practice today to dilute the reducing gas constituents with less expensive inert gases such as high purity nitrogen which has very low water vapor content (<1ppm) that corresponds to a dew point[2] of below -90°C. However the improvement of the atmosphere, in terms of lowering the water vapor content due to the dilution with nitrogen, does not correspond necessarily in improvement of the reducing ability of the atmosphere [11, 15, 17, 22, 76, 77]. The reason for this is that one has to consider the partial pressure ratio of hydrogen and water vapor and thus consider the hydrogen content as well. Due to the dilution, the total hydrogen content decreases as well and so does the partial pressure ratio which in turn is translated into lower reducing ability of the atmosphere. Therefore it is necessary at this point to emphasize that the proper evaluation of the quality of the sintering atmosphere can only be done on the base of the partial pressure ratios of active gases $p(H_2)/p(H_2O)$ or $p(CO)/p(CO_2)$ [11, 15, 17, 22, 76, 77].

For the systems of interest all the gaseous species mentioned earlier (H_2, H_2O, CO and CO_2) exist and at elevated temperatures they interact with one another according to the so-called "water gas" reaction:

$$2H_2 + 2CO_2 \leftrightarrow 2H_2O + 2CO \qquad (20)$$

The equilibrium constant for **Re. 20** is given by:

$$K_w = \left[\frac{p(H_2O)\cdot p(CO)}{p(H_2)\cdot p(CO_2)}\right]^2 \qquad (21)$$

The standard Gibbs free energy change associated with the water gas reaction is connected with the equilibrium constant with the following relationship:

$$K_w = exp\left(-\frac{\Delta G_w^0}{2RT}\right) \qquad (22)$$

Thus it is possible to arrive in a temperature dependent proportionality between the pressure ratios of the reducing and oxidizing constituents:

$$\frac{p(CO)}{p(CO_2)} = K_w \cdot \frac{p(H_2)}{p(H_2O)} \qquad (23)$$

The conclusion of **Eq. 23** is essentially that in atmospheres containing both H_2 and CO, the equilibrium partial pressures cannot be changed independently from one another. For example if the water vapor content of an atmosphere is decreased then the

[2] *Dew point is the temperature to which an atmosphere must be cooled down in order for the water vapour that is contained in to it, to condense into liquid water. It is essentially a measure of the water vapour content (humidity) of an atmosphere. Today there are many tables converting values of p(H2O) into dew point temperature.*

$p(CO)/p(CO_2)$ ratio will be automatically raised under equilibrium conditions [11, 15, 17, 22, 76, 77].

For the material systems of interest a number of studies [3, 6, 7, 12, 14, 15, 52, 54, 81] have shown that the Fe-oxide can be efficiently reduced by hydrogen at temperatures between 300-500°C according to **Re. 10**. At higher temperatures though the reducing activity of hydrogen is decreased and thus there is a need for another reducing agent. More stable oxides like Cr- and Mn-based oxides will be reduced at higher temperatures (>800°C) mainly by the carbothermal reduction mechanisms (**Re. 14** and **15**) which become more pronounced at such temperatures [3, 4, 6, 7, 11-17, 20, 43, 44, 50, 52, 54, 55, 78, 81, 82]. It was also concluded that the main reduction mechanism is the indirect carbothermal (**Re. 15**). Gas analysis of the products formed at elevated temperatures showed that the CO peak associated with the carbothermal reduction shows a maximum between 800-1000°C and is connected to the reduction of Fe-rich oxide. Due to the Bouduard reaction (**Re. 16**), the CO_2 through the indirect carbothermal reaction (**Re. 15**) will further react with the graphite still present on the pores thus leading to the formation of more CO. For Cr-containing oxides the reduction starts above 1000°C but with the maximum of the gas analyses peaks for this reaction appearing above 1120°C. Additionally, the observed peaks at this temperature range are also associated with the reduction of oxides from internal pores that are at least partially open to the surface [3, 7, 9, 12, 14, 15, 52, 54, 83].

4 Research Topic and Aim of the Study

One of the main aims of the PM steel industry today is to continuously improve the mechanical properties of the produced structural parts in a cost efficient manner. This can be achieved by:

- Minimizing the porosity i.e. by applying higher compaction pressures
- Tailoring the final microstructure of the consolidated material by careful alloying with elements such as Cr, Mo, Mn, V, Si etc.
- Optimizing the sintering process in order to provide stronger inter-particle necks

It was explained in previous chapters that especially when introducing alloying elements like Cr, Mn and Si, the most critical aspect is the high sensitivity of those elements to oxygen which leads to the possible formation of thermodynamically stable oxides. Oxide "islands" rich in these oxidation sensitive elements, were found to be distributed on the surface of water atomized steel powder along with a thin Fe-oxide layer [61]. It is therefore essential to reduce, as much as possible, the surface oxides in order for efficient sintering to take place and consequently to attain the desired mechanical properties. The main factor that will influence the reduction of the surface oxides and will ensure the development of strong inter-particle necks is the choice of the sintering atmosphere and its strict control in terms of composition and purity during the sintering process.

The fundamental knowledge concerning the surface chemistry of metal powder and how it changes during reduction/oxidation processes that take place during the heating/sintering stage is of paramount importance for the successful manufacturing of PM steel parts. Furthermore it is essential to understand the basic phenomenology of how and why different process parameters could affect the mechanisms for reduction/oxidation in order to establish the necessary requirements and create a process map for efficient sintering.

The aim of this performed study was to explore the key aspects described above by:

- Characterization of chromium pre-alloyed powder grades both on the surface and the interior of metal particles using high resolution analytical techniques
- Study of the mechanisms of reduction/transformation of the surface oxides during the heating and sintering stages
- Investigation of the effect of atmosphere composition, heating rate and green density on the afore mentioned reduction/oxidation processes and correlation with mechanical performance

During this study special interest was taken in investigating the oxide phases observed on both surface and interior of the powder and how varying process parameters would affect their behaviour during the sintering process.

5 Experimental Work

The experimental approach which was followed in this study in terms of chosen material and experimental setup is described briefly in this chapter. Additionally the analytical techniques used for this investigation are explained in a very general way in order to understand the reasoning behind their choice and consequently correlate with the obtained results. Since the main focus of this work is towards the changes in the surface chemistry of metal powders with varying process parameters, special attention was put into utilizing surface sensitive analytical techniques as well as to perform thermal analysis. Finally, due to the fact that fracture surfaces of heated/sintered samples were extensively studied a brief introduction in the fractography of PM steels explaining some basic principles is also included in this chapter.

5.1 Materials and Experimental Setup

Two different material systems were studied during this research work. Both systems are based on commercially available water atomized steel powder pre-alloyed with Cr and Mo, provided by Höganäs AB, Sweden. In **Table 1** the nominal composition of the powder materials is given.

Table 1. *Nominal chemical composition (in wt.%) of the powder grades under investigation*

Powder Grade	Cr	Mo	Mn	Si	C	O	Fe
Material A	3	0.5	<0.1	<0.03	<0.01	<0.2	Bal.
Material E	1.5	0.2	<0.15	<0.01	<0.01	<0.15	Bal.

The main efforts of this work were put into material A (commonly known as Astaloy CrM) because, due to its composition, is the one that has the highest requirements in terms of atmosphere control during the sintering process in comparison with other pre-alloyed grades. Since though the experimental setup, which will be described later on, was conceived and realized for the first time in our laboratory, it was necessary to have a test material for benchmarking of our systems and thus material E (known as Astaloy CrL) was also investigated up to a certain extent.

At first both kinds of powders were investigated in their “as-received” state. For this reason a small amount of powder was placed between soft aluminium plates and using low pressure (1-2 MPa) the metal particles were “mechanically” impregnated into the plates. In turn the plates were separated and the adhered powder was used for the investigation.

For the powder characterization a variety of analytical techniques, which are described in the next section, were used. A brief summary of the applied techniques and their use in the investigation is given in **Table 2** below.

For the internal inclusions study special attention to sample preparation was required. A detailed description can be found in Paper II. The investigation was performed with the use of the SEM and detailed EDX mapping. The processing conditions were adjusted

according to the sample characteristics in order to have the highest possible accuracy with these techniques.

Table 2. *Summary of the applied experimental techniques*

Experimental technique	Use in the investigation
X-ray photoelectron spectroscopy (XPS) combined with Ar-ion sputtering	- *Surface chemical analysis* - *Chemical state identification* - *Compositional depth profiling*
High resolution scanning electron microscopy (HR-SEM) combined with energy dispersive X-ray spectroscopy (EDX)	- *Morphology of the powder surface* - *Chemical microanalysis* - *Imaging of powder cross-sections* - *Elemental mapping* - *Fractographic investigation*
Auger electron spectroscopy (AES)	- *Characterization of individual particulate features on the powder surface* - *Compositional depth profiling*
Thermogravimetry (TG)	- *Thermal analysis of loose powder*

For the interrupted sintering trials mixtures consisting of the powder under investigation, 0.5wt.%C in the form of natural graphite (UF4) and 0.6 wt.% Kenolube® as lubricant were prepared. The mixture was then uniaxially compacted with 600MPa into un-notched Charpy test bars with the following dimensions: 10x10x55mm (ISO 5754) and green density of ~7.0 g·cm^{-3} (**Fig. 21**). In order to evaluate the effect of the density of the green compact, samples of higher density (7.25 g·cm^{-3}) of the same geometry were also prepared using 800MPa compaction pressure and heated die (80°C) but only for the material A. The high density samples contained 0.5 wt.% EBS-based lubricant instead of Kenolube® .

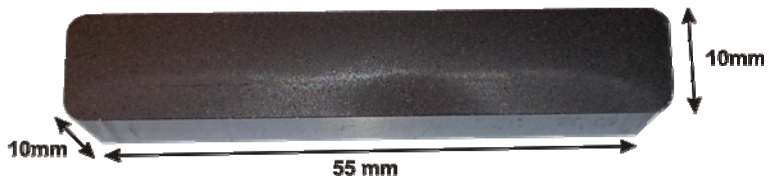

Fig. 21. *Geometry of the samples used for the sintering trials.*

Prior to the sintering experiments the specimens were de-lubricated at 450°C for 30 min in pure N_2 flowing atmosphere. The effects of the sintering atmosphere composition were evaluated by using nitrogen-based atmospheres with varying hydrogen content (0, 3% and 10% of hydrogen) as well as by performing vacuum sintering.

Sintering in the nitrogen-hydrogen blends was performed in an *Entech* laboratory tube furnace with a tube diameter of 43mm (see **Fig. 22**). The gas flow was ~12 lt·min^{-1} and the dew-point (DP) was monitored inside the tube furnace directly above the container with the samples. Before each sintering experiment the furnace was purged, with the gas used for the sintering, until a dew-point of ~-50°C was reached. Vacuum sintering

experiments were done in pilot high vacuum furnace (10^{-5} mbar working pressure) built by *Parkburn Controls Ltd* according to *Vacuatherm Sales* specification.

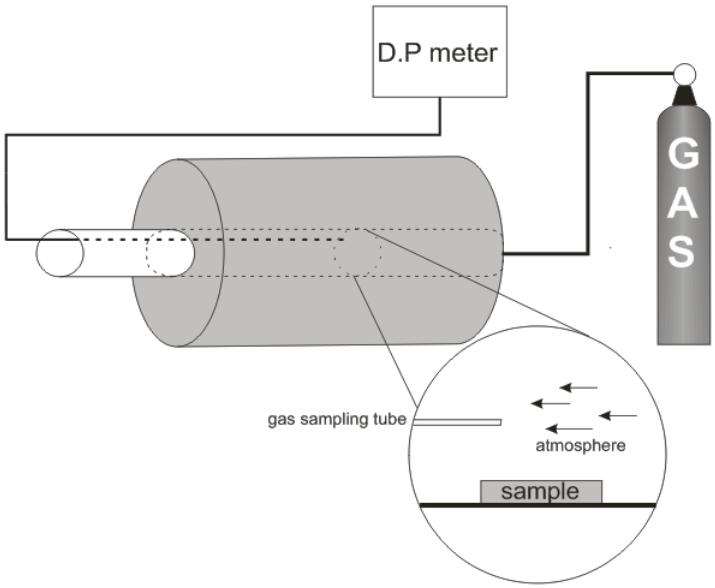

Fig. 22. *Experimental setup for the interrupted sintering trials performed in the tube furnace (Author's illustration).*

In the experimental setup shown in **Fig. 22** samples of 7.0 g·cm^{-3} green density of both powder grades, A and E, were sintered with a constant heating rate of 10°C·min^{-1}. The specimens were then sampled at different temperatures: 700, 800, 900, 1000, 1120 (1, 15 and 30min), 1200°C (1 and 30min) (**Fig. 23**). The specimens were rapidly cooled using pure N_2 with high flow rate. The cooling rate was approx. 150-200°C·min^{-1} for the specimens sintered in N_2/H_2 blend and in pure N_2. For the samples sintered in vacuum the cooling rate was approx. 100°C·min^{-1}. All the samples after the heating/sintering were annealed at 200°C for 1 hour in a pure N_2 atmosphere with the moderate flow rate of 5lt·min^{-1}.

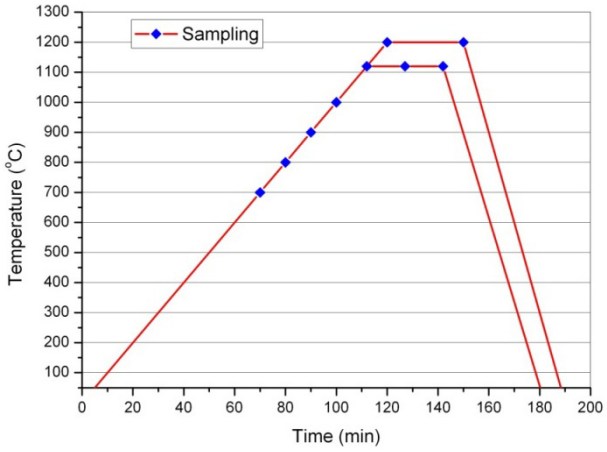

Fig. 23. *Temperature profile for the interrupted sintering trials experiments.*

Additional sintering trials were performed, only for material A, in a *Netzsch DIL 402C®* (**Fig. 24**) pushrod dilatometer which had a sample carrier system specifically designed for the samples used in this investigation. The aim of this study was not to perform dilatometric studies of the specific material since this has been already done very

thoroughly [7, 9]. On the other hand this experimental setup offers the capabilities of a very well controlled environment in terms of temperature profile and atmosphere flow which in turn ensure the good repeatability and consistency of the experiments.

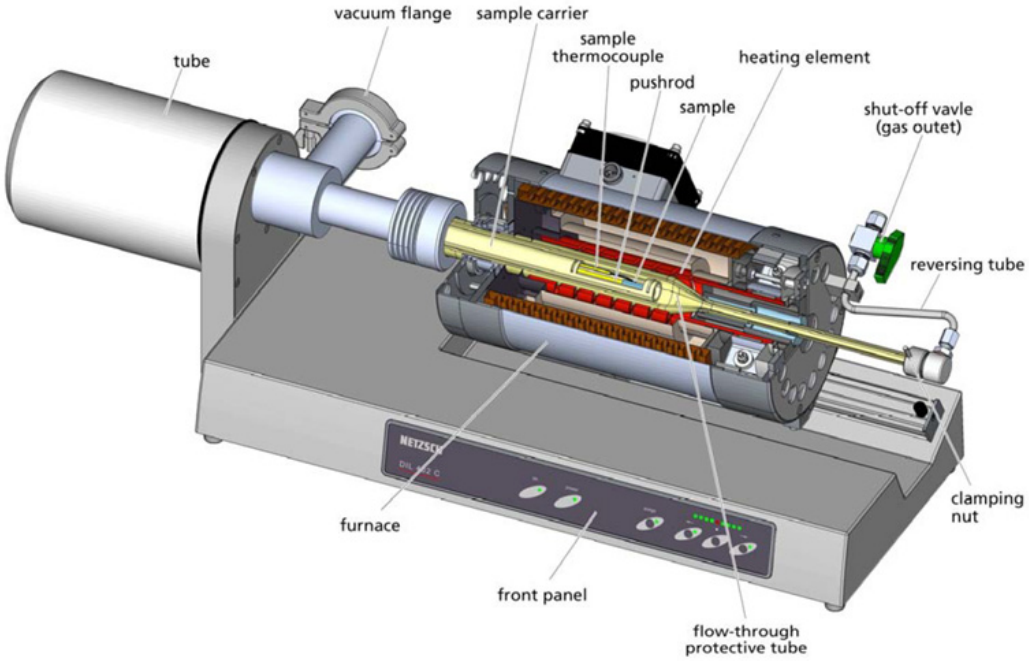

Fig. 24. *Illustration of the Netzsch DIL 402C dilatometer unit used for interrupted sintering trials (from [84], courtesy of NETZSCH-Gerätebau GmbH).*

Prior to every experiment the dilatometer was evacuated and purged with high purity argon for 3 times. The same atmospheres as the ones used in the previous experimental setup were also employed in the dilatometer as well and the same sintering trials were performed for consistency purposes. In the dilatometer though each sample was processed separately and as soon as the temperature of interest was reached the sample was cooled down to room temperature with an average cooling rate of 30° C·min^{-1}. Typical temperature profiles for the sintering trials in the dilatometer are shown in **Fig. 25**. The used flow was 220 ml·min^{-1}, which was the highest possible, with the diameter of the dilatometer furnace being 26 mm. Sintering trials on high density samples were also performed but only in N_2/3%H_2 atmosphere. Additionally for all the experiments performed in N_2/3%H_2, for both normal and high density compacts, three different heating rates were investigated: 10, 30 and 50° C·min^{-1}. It must be noted at this stage that the samples processed in the dilatometer were not subjected to an annealing treatment afterwards. All the performed interrupted sintering trials are summarized in **Table 3**.

Thermogravimetric (TG) studies were performed in a simultaneous thermal analyzer Netzsch STA-449F1 Jupiter® in order to evaluate the extent of oxidation/reduction processes in different atmospheres in quantitative terms. The behaviour of material A was studied by analyzing de-lubricated samples as well as loose powder of ~2g each in different atmospheres. The samples were heated up to 1200°C with 10°C·min^{-1} heating rate and holding at that temperature for 30min. In this way it was possible to study the reactions that were taking place as a function of temperature with respect to the used

atmosphere. The same atmosphere compositions as the ones used in the interrupted sintering trials were used for TG experiments as well with the difference that now instead of nitrogen, the atmospheres were argon-based due to the instrumental setup.

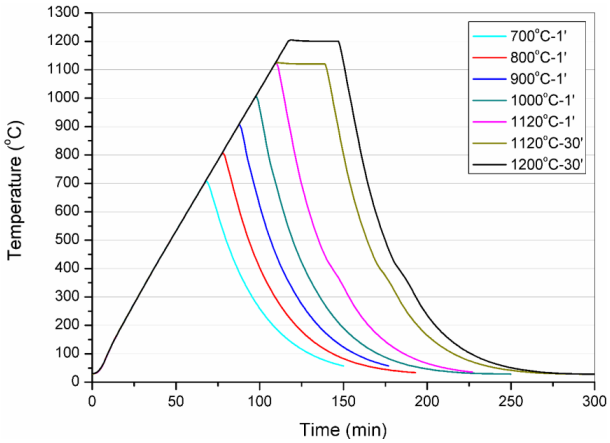

Fig. 25. *Temperature profile of performed sintering trials in the DIL 402C dilatometer furnace.*

Table 3. *Summary of the applied conditions for the performed interrupted sintering trials (T.F signifies the trials performed in the tube furnace and DIL the ones performed in the dilatometer)*

	Atmospheres				**Heating rate**	**Green density**
	N_2	**N_2/3%H_2**	**N_2/10%H_2**	**Vacuum**		
Astaloy CrL	T.F		T.F	T.F	10° C·min^{-1}	7.0 g·cm^{-3}
Astaloy CrM	T.F + DIL	T.F + DIL	T.F + DIL	T.F + DIL	10° C·min^{-1}	7.0 g·cm^{-3}
		DIL			30° C·min^{-1}	
					50° C·min^{-1}	
		DIL			10° C·min^{-1}	7.25 g·cm^{-3}
					30° C·min^{-1}	
					50° C·min^{-1}	

Impact testing was performed using an *Instron*® instrument according to the standard SS – EN 10045-1 in order to acquire information concerning mechanical properties and relate to the performance of the compact. The produced fracture surfaces were then examined under a *LEO*® *Gemini 1550* high resolution scanning electron microscope (HR-SEM) in combination with *INCA*®*-Energy* energy dispersive X-ray analyzer (EDX). Additionally bulk oxygen and carbon chemical analyses were performed in a *LECO*® instrument in Höganäs AB, Sweden, for all the specimens in order to track the changes of O- and C-content during the sintering process. It has to be pointed out that all the sintering trials have been performed 3 times in order to get statistically correct values for the impact energy and the O- and C-content. Finally metallographic investigation was performed in some cases in order to examine the obtained microstructures.

5.2 Analytical Techniques

5.2.1 High Resolution Scanning Electron Microscopy (SEM) and Energy Dispersive X-ray Spectroscopy (EDX)

Today the Scanning Electron Microscope (SEM) is the most commonly used advanced analysis technique for the purposes of material science. The basic principle of an SEM involves the bombardment of a sample by a convergent beam of electrons in ultra high vacuum (UHV) and the detection of the signals emitted by the area of the sample where the electron beam is irradiating. The incident beam of electrons is produced from an electron source and it is manipulated by a system of electromagnetic lenses [85, 86]. In **Fig. 26** a typical schematic representation of the SEM is shown.

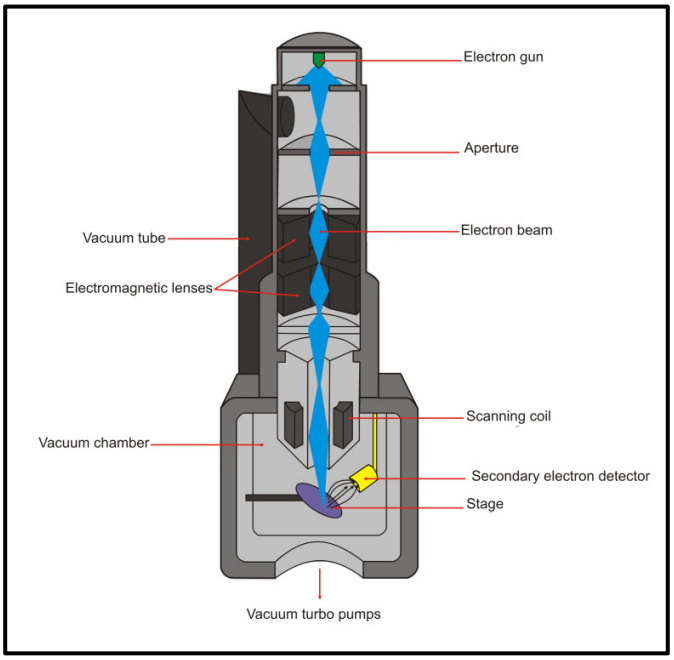

Fig. 26. *Schematic representation of an SEM (Author's illustration).*

There are many types of interactions that can occur between the electron beam and the specimen which consequently lead to the production of various detectable signals that can be used in different imaging modes. As the electrons of the primary beam penetrate the specimen they will undergo scattering which will result in an "effective beam diameter" which is larger than the actual diameter of the incident beam. The size of the produced interaction volume is dependent on the energy of the incident beam (the higher the energy the larger the penetration depth will be) and the elemental composition of the specimen (**Fig. 27**).

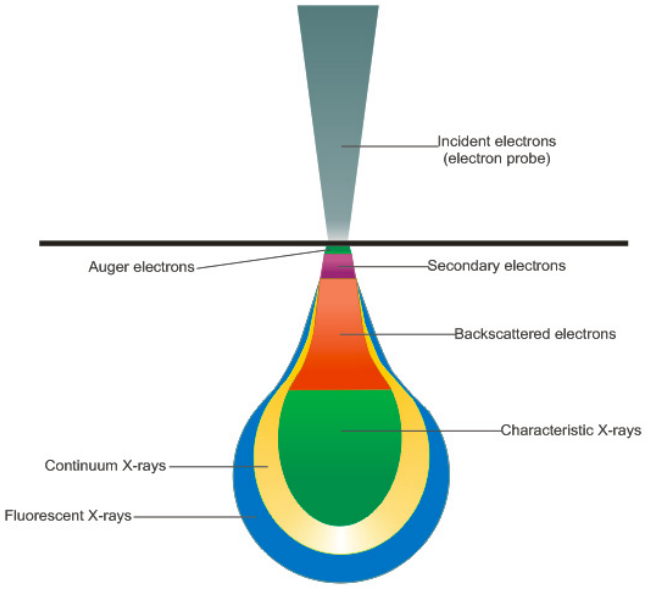

Fig. 27. *Example of interaction volumes for different types of signals (Redrawn from [86]).*

One of the main advantages of the SEM is the extremely large depth of focus which helps to produce "3D-like" images which give a significant amount of topographical information. Additionally the SEM offers high spatial resolution (5-10nm for a conventional SEM) which gives the possibility to get reliable information of microscopic features.

For the purposes of this study the instrument used was a LEO 1550 Gemini equipped with a Field Emission Gun (FEG-SEM). For experimental consistency reasons the same set of parameters was used throughout the whole study: Accelerating Voltage=15kV, Aperture=20μm and working distance: WD=9mm. This set of parameters was regarded suitable in the frame of this study and is relevant with the experimental configuration and the material under investigation.

The main imaging mode used was based on the signal acquired from the emitted secondary electrons (SE). The secondary electrons are emitted from the surface region (**Fig. 27**) and they offer i) higher resolution and ii) higher signal-to-noise ratio which results in higher quality images and better topographical contrast in comparison with other imaging modes. The instrument used in this study is equipped additionally with an InLens Secondary Electron Detector which is placed inside the lens system and offers even better contrast and therefore superior image quality especially at low beam voltage.

The interaction of a sufficiently high energy electron beam with the atoms of the sample may result in knocking out a core electron and this in turn will leave the atom in an excited state. The de-excitation process involves the transition of an electron from a higher energy state to the ground state. The excess energy is then released in two possible ways:

i) By emitting an Auger electron (see section 5.2.3)

ii) By emitting a characteristic X-ray photon

Since the emitted X-rays have energies that are uniquely indicative of the elements of origin (**Fig. 28**), they can be used to identify the present elements as well as their amounts [85-87]. The incident electrons can also decelerate due to the interaction with the atom core which will result to the production of X-rays with energies from zero to the incident electron beam energy. These X-rays are appearing as a continuous spectrum and are known as "X-ray continuum" or "Bremsstrahlung". For the purposes described above a Link ISIS energy dispersive X-ray spectroscope (EDX) that was attached to the SEM, was also used.

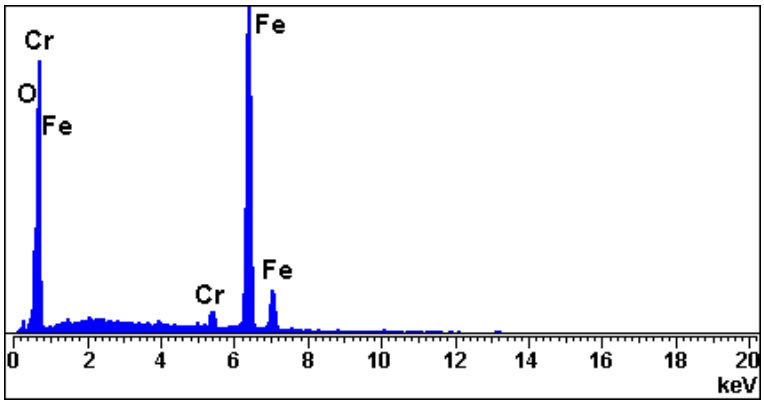

Fig. 28. *EDX spectrum of the free surface of Cr-alloyed steel powder (Author's experimental result).*

5.2.2 X-ray Photoelectron Spectroscopy (XPS)

Significant part of this research has been devoted to the surface analysis of metal powders where one of the principal surface sensitive analytical techniques used was the X-Ray Photoelectron Spectroscopy (XPS), otherwise known as electron spectroscopy for chemical analysis (ESCA) [88-90]. The basic principle behind XPS involves the ejection of an electron from a core level of an atom by an X-ray photon of energy hv (**Fig. 29**).

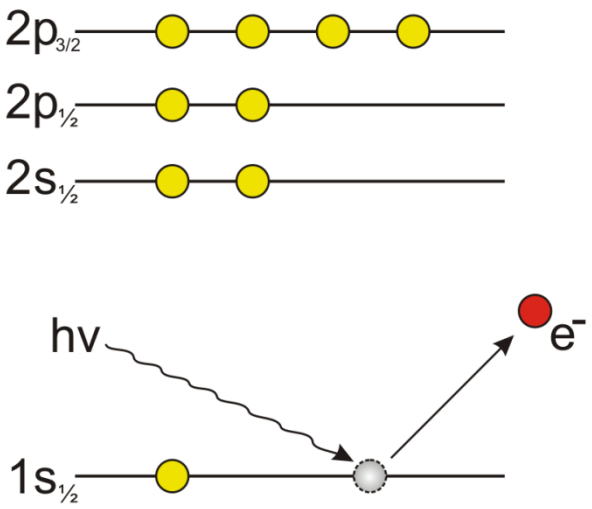

Fig. 29. *Schematic representation of the XPS process showing the photoemission of an electron from the 1s state (Author's illustration).*

The experimental quantity measured by the spectrometer is the kinetic energy (E_K) of the photoelectron which in turn depends on the energy of the X-ray photon. The intrinsic property that relates to the analyzed material is the binding energy (E_B) of the

electron which identifies the both the parent element and the atomic energy level. Therefore the E_K is given by:

$$E_K = hv - E_B - \varphi \qquad (24)$$

Where φ is the spectrometers work function and is characteristic of its experimental configuration. The acquired spectrum basically reproduces the electronic structure of the analyzed element since all the electrons with a binding energy smaller than the energy of the X-ray photon will appear in the spectrum. The characteristic peaks appearing in an XPS spectrum are associated with photoelectrons that escape without energy loss whereas the background contribution of the spectrum is associated with the photoelectrons which have undergone inelastic scattering and thus suffered energy loss (**Fig. 30**).

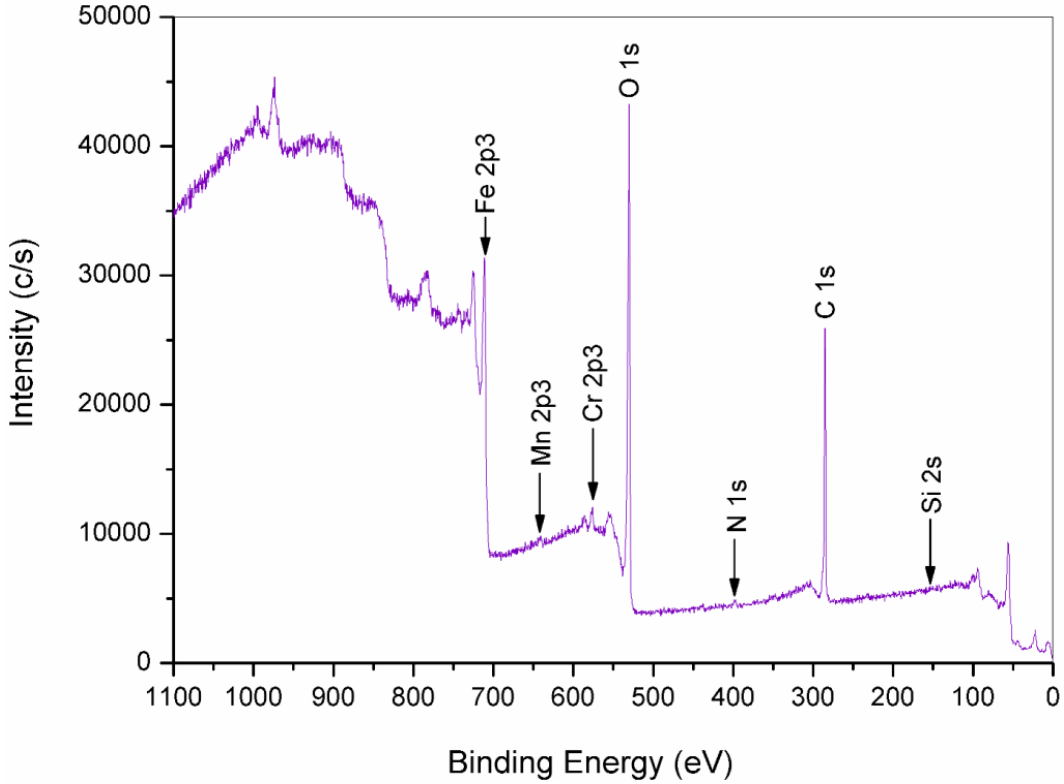

Fig. 30. *XPS survey spectrum of Cr-alloyed steel powder in the as-received state (Author's experimental result).*

In the early days of the XPS it was discovered that if atoms of the same element are "non-equivalent" due to i.e. different oxidation states then this will result in a measurable difference in their binding energies. This "chemical shift" can be analyzed and the information concerning the chemical state of the analyzed compound is considered to be the main advantage of the XPS technique.

A schematic representation of the configuration of an XPS system is given in **Fig. 31**. The system used in this study is a PHI 5500 spectrometer. The X-ray source was an $Al_{K\alpha}$ source with hv=1486.6 eV. The produced X-rays are monochromatized and then they irradiate approximately 0.8mm^2 of the sample surface which corresponds to more than 100 powder particles.

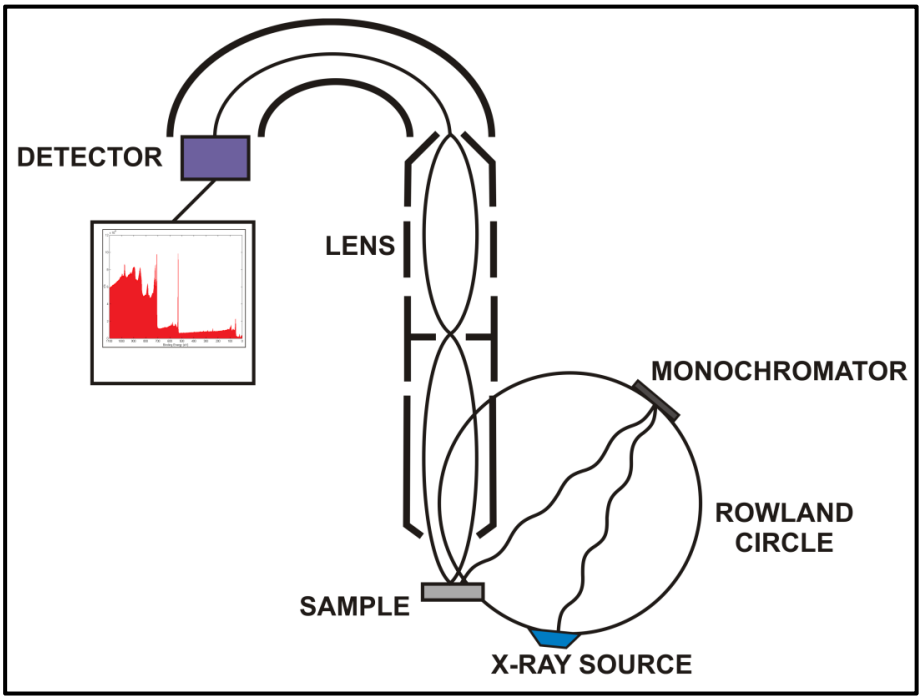

Fig. 31. *Schematic representation of the XPS instrument (Author's illustration).*

For the purposes of this study, XPS was used in order to identify the chemical states of the elements present on the surfaces of the steel particles, to determine the surface oxide composition and thickness and to acquire depth profiles of the elements of interest.

5.2.3 Auger Electron Spectroscopy (AES)

Another surface sensitive technique which was used during this study is the Auger electron spectroscopy (AES) which was used in order to overcome the handicap of the large interaction volume of the EDX technique and therefore to be able to analyse more accurately the features encountered on the powder surface.

As mentioned earlier (see section 5.2.1) the emission of Auger electrons is an alternative de-excitation process when an atom has become ionized. In more details, the vacancy created in the core shell after ionization can be filled by an electron coming from one of the outer shells which of course have higher energy state. Therefore in order to comply with the principle of the energy conservation, the excess energy that comes from the transition of the electron from a higher to a lower energy state is absorbed by another electron which then escapes the attraction of the nucleus and leaves the atom (**Fig. 32**) [88, 89, 91]. The Auger emission is the dominant de-excitation process in comparison with the X-ray fluorescence for relatively shallow core levels i.e. with binding energies below ~2 keV. The same applies for the other atomic levels (L, M, N, etc) as well. Basically this means that the Auger emission is the most probable relaxation process for elements with atomic number Z<30 and thus more efficient analysis can be performed in those elements [88, 89].

The kinetic energy of the Auger electron is expressed by the following:

(25)

Where E_K, E_{LIII}, and E_{LI} are the binding energies of the energy shells involved in the process [88, 89, 91].

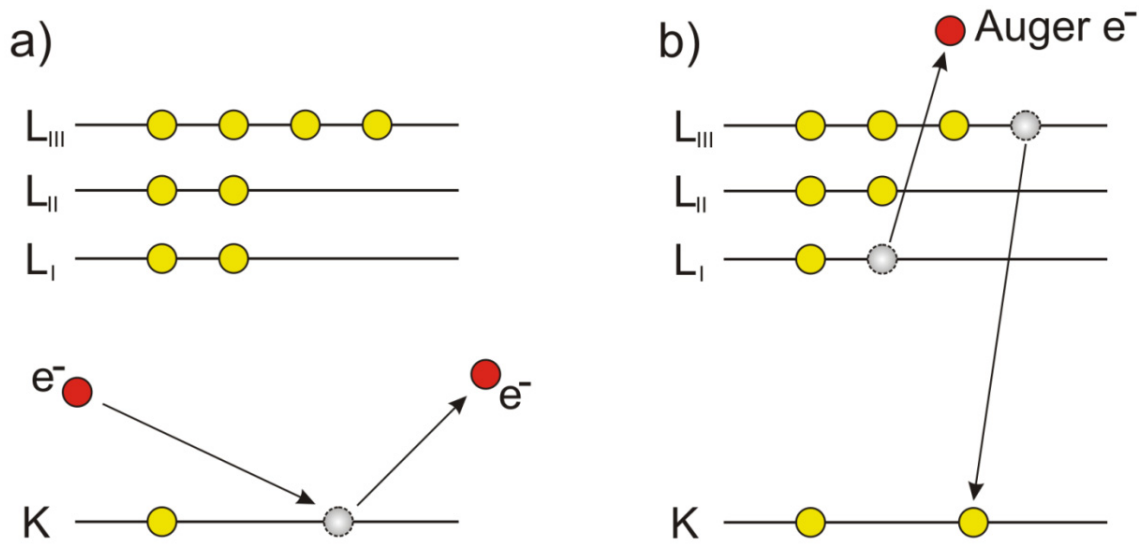

Fig. 32. *The Auger process for the $KL_{III}L_I$ transition (Author's illustration).*

The energy of the ejected Auger electron, as described in **Eq. 25**, is a function of only the energy levels of the atom. For each element in the Periodic Table there is a unique set of Auger energies. Therefore, the Auger analysis can be used directly for elemental identification. The kinetic energy of the Auger electron is the intrinsic quantity of the investigated material and is independent on the primary beam in terms of both composition (X-rays, electrons etc.) and energy.

The use of an electron beam, which can be manipulated and be very finely focused, in the case of AES gives the possibility to perform surface analysis at very high spatial resolution and consequently to analyse features that are not possible to do so with other surface sensitive analytical techniques.

The Auger electrons have low kinetic energies (<1000 eV) therefore similarly to the photoelectrons in XPS, only those coming from the outermost surface layers of the material can escape and be detected. This depth of analysis for both methods varies with the kinetic energy of the considered electrons. It is basically determined by the electron attenuation length λ which is related to the inelastic mean free path. Generally if we consider the electrons that are emitted at 90° angle to the sample surface then 95% of the intensity of the recorded signal will originate from a depth<3λ. This in turn can be translated into an analysis depth of 3-10nm depending on the material and experimental setup [88, 89].

In this investigation the high spatial resolution of the AES technique was exploited in order to analyze observed features on the powder surfaces. AES was used in a complementary way along with the XPS. It was possible to analyze individual particulate oxides and performing depth profiling on both the particulate oxides and the surface layer. This way it was possible to check the homogeneity of the particulate oxides and also to perform accurate estimation of the oxide layer thickness for verification of the XPS results. The instrument used in this investigation was a Thermo Microlab 350 that gives spatial resolution of approx. 20 nm at 10 kV beam energy.

Depth profiling and determination of oxide layer thickness

One additional feature that was used both in the XPS and in the AES was the possibility to perform compositional depth profiling. This happens by repeating the removal of material by bombarding the sample with noble gas ions (Ar^+) for some time and then analyzing the exposed material.

By performing AES depth profiling on homogeneous oxide layer, on a flat substrate it is possible to determine the oxide layer thickness by considering:

$$t^{OX} = \frac{I_{max}^{OX} - I_{min}^{OX}}{2} \qquad (26)$$

Where I_{max}^{OX} and I_{min}^{OX} are the maximum and minimum recorded intensities of the signal from the oxide. However this method gives a systematic error in the estimation of the oxide layer thickness due to the effect of depth resolution[3]. This error decreases with increasing t^{OX} [92]. The variation of the etch rate due to the irregular shape of the powder was considered and according to [65] the etch rate is rather constant in a band with a width corresponding to about 15-20% of the radius which for particulates with radii 200-300 nm this gives a band width of about 30-60 nm. Due to the high spatial resolution of the Auger nano-probe it was possible to place the analysis points with precision thus ensuring that the analyzed area was essentially "flat" in the microscopic scale which in turn provided reliable depth profiles where the oxide layer thickness could be calculated according to **Eq.26**.

In the case of XPS, **Eq.26** is not valid, since the analyzed area is significantly larger and the irregularity of the powder surface creates a variation in the etch rate due to the variation of incidence angles. This variation was taken into account in a model developed for spherically shaped particles [67-70] when calculating the normalized metal intensity (I^{MET}/I_{∞}^{MET}) which can then be plotted as a function of the etch depth for various thicknesses of oxide layers. Of course, different metal oxide systems will have different metal intensity profiles [68, 69]. As indicated in [68] in the case of $20 \geq t^{OX}/\lambda^{OX} \geq 3$, where λ^{OX} is the electron mean free path in the oxide, then the I^{MET}/I_{∞}^{MET} value is in the narrow range of 60 to 72%. Thus in plots of the normalized metal intensity ratio (I^{MET}/I_{∞}^{MET}) versus the etch depth the value where the ratio is 65% gives a good estimate of the oxide layer thickness. This method was also used for the irregularly shaped metal particles of the powder grades of this investigation and gave reliable and consistent results.

The reliability of the determination of the thickness of an oxide layer using surface sensitive analytical techniques has been verified in various studies with other methods [92]. In this study both XPS and AES depth profiling were performed on material A with similar results for the thickness of the surface Fe-oxide layer.

[3] Depth resolution in a compositional depth profile is a measure of the broadening of an abrupt interface which is caused by physical (mainly due to λ) o instrumental effects

5.2.4 Thermogravimetry (TG)

Thermogravimetry (TG) is a thermal analysis experimental technique in which the mass change of a sample is measured as a function of temperature when the sample is subjected to a controlled temperature program [93-96]. The TG essentially consists of a highly accurate balance on which a crucible containing the sample is placed which in turn is put inside a furnace. The furnace then can be programmed to reach the desired temperature and any mass change occurring during this temperature program, due to different reactions, is recorded [93-96]. It is possible to utilize different atmospheres and thus study the interaction of the sample with the process gas.

The instrument used in this study was a simultaneous thermal analyzer Netzsch STA-449F1 Jupiter® (**Fig. 33**). The system was equipped with a silicon carbide furnace and a tungsten/rhenium sensor thermocouple in order to have the possibility to work with hydrogen-containing atmospheres [93].

Thermal analysis techniques such as TG have been extensively used in metallurgy in order to investigate a large range of phenomena like oxidation and reduction processes, corrosion studies etc [93-96]. In this study the purpose of using TG was to determine the temperature range and the extent of the reduction/oxidation reactions taking place as a function of temperature in relation with the atmosphere composition and purity. These measurements were straightforward since reduction or oxidation of the specimen will lead to decrease or increase in sample mass, respectively.

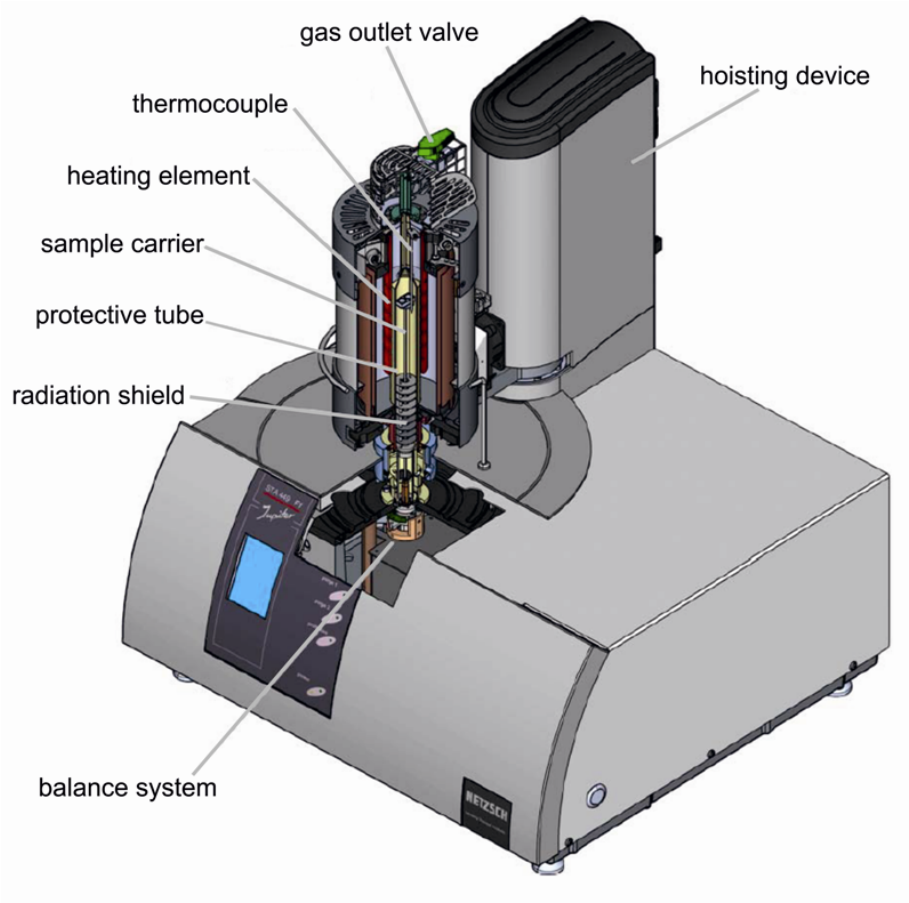

Fig. 33. *Simultaneous Thermal Analyzer: Netzsch STA-449F1 Jupiter®(from [93], courtesy of NETZSCH-Gerätebau GmbH).*

5.3 Fractography of PM Steels

The purpose of fractographic investigation is to determine how and why a component fails and in this respect to gather information concerning the cause of failure or the existing conditions and respectively to avoid similar situations in the future [38]. The main source of information is the fracture surface of a failed component.

In principal there are only two possible modes of fracture from a macroscopic point of view – ductile or brittle. This distinction has to do with the amount of plastic deformation that the component has undergone prior to failure. If the material is ductile it can undergo extensive plastic deformation whereas the absence of deformation indicates a brittle failure [38].

By examining closer a fracture surface with the help of a light optical microscope or by means of SEM it is possible to further categorize the fracture mechanisms in four categories:

1. Dimple Rupture (Ductile Dimple Fracture) – it consists of the nucleation, growth and coalescence of microvoids. It is the typical type of failure for the most common metals. Defects such as particles, inclusions, grain boundaries etc. can be the starting point for areas with high stress concentration which in turn will lead to the steps described above. If this failure occurs along the grain boundaries then it is characterized as "Intergranular Dimple Rupture (or Ductile Fracture)" (**Fig. 34a**) whereas if the microvoids nucleate inside the grain then the fracture mode is called "Transgranular Dimple Rupture".
2. Decohesive Rupture (Brittle Intergranular Fracture) – brittle fracture along grain boundaries. It is also called "Grain Boundary Separation".
3. Cleavage (**Fig. 34b**) – low energy fracture mode that takes place in specific crystallographic planes, also known as cleavage planes. Cleavage occurs either when dislocation movement is impossible or heavily blocked on slip planes or when slip cannot take place. Cleavage has different features like river patterns, tongues etc. which depend on the materials microstructure.
4. Fatigue – failure that occurs as a result of a repetitive or cyclic loading and has three stages, i) crack initiation, ii) crack propagation and iii) final fracture.

In principal one has to remember that the morphology of the fracture surface is determined by the local fracture micromechanism which is strongly dependent on the microstructure, local stress state and conditions (temperature etc.).

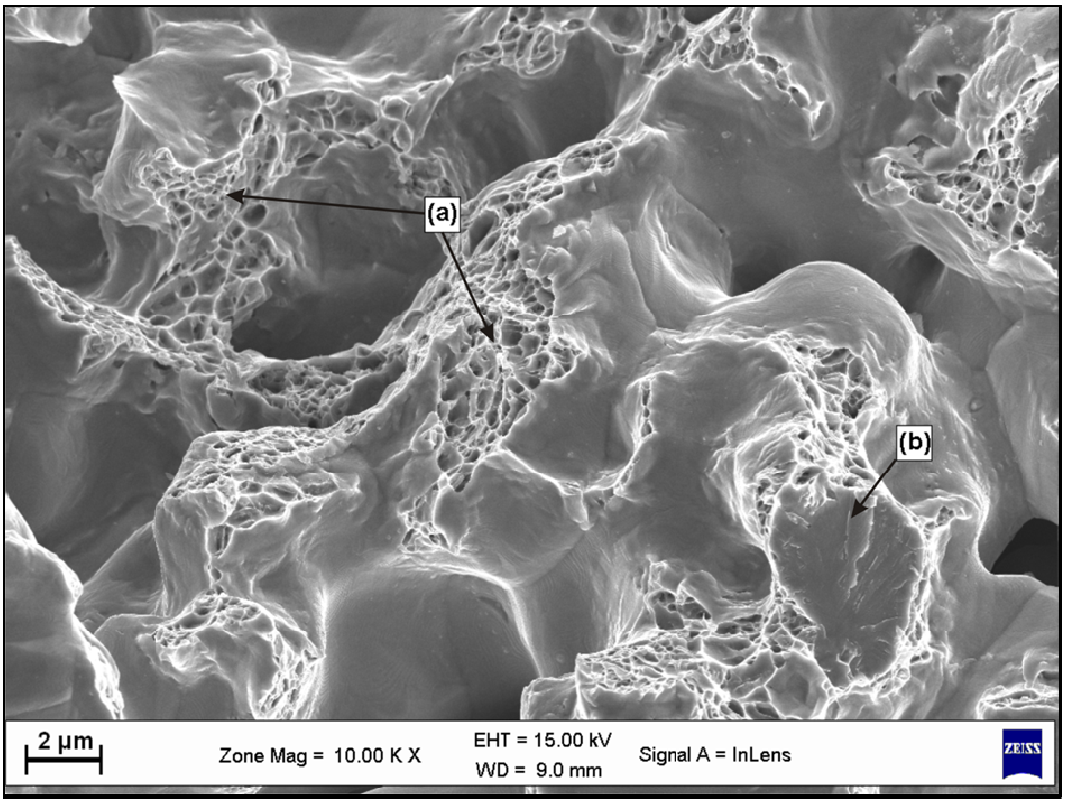

Fig. 34. *Micrograph of a fracture surface of a sintered low-alloyed Cr-Mo PM steel showing a) inter-particle dimple ductile fracture and b) trans-granular cleavage (Author's experimental result).*

The fracture of sintered steels in general resembles the behaviour of wrought steels with the major difference being that of the presence of pores and residues from the original powder surface along with the more complex microstructures. For low to intermediate densities the plastic strain is concentrated at the inter-particle necks which can deform significantly during loading. This deformation is much larger in comparison with the material of the metal particle volume. Therefore the plastic deformation in the sinter necks (microscopically) is high and thus the fracture is ductile whereas macroscopically the elongation to fracture is low and the material fractures in a brittle manner.

Since the development of sinter necks is the result of mass-transport processes it is possible to evaluate how readily these processes are taking place by examining the development of the inter-particle connections during the sintering process. The strength and the area related to the inter-particle connections can be correlated with the efficient reduction of oxides that could hinder the development of sinter necks. An example is given in **Fig. 35** where the strength of the inter-particle connections increases with increasing temperature during the sintering process.

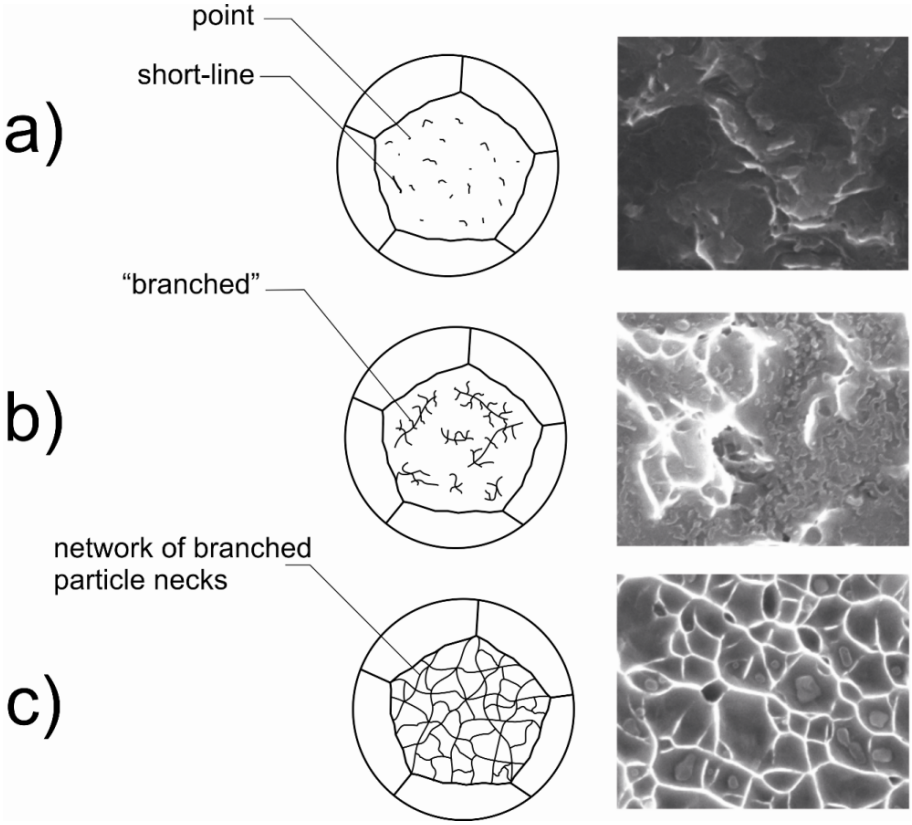

Fig. 35. *Development of inter-particle connections in the early stages of the sintering process – the temperature increases from a-c and so does the strength of the connections (Author's illustration).*

6 Summary of Results and Main Conclusions

This thesis is based on the results from 8 appended papers (Papers I – VIII). The main focus of the study was placed on the analysis of the surface characteristics of Chromium-alloyed metal powder and how the surface chemistry of those powders would change during the sintering process if different conditions are applied. Paper I, III and VII deal with the establishment of a methodology for evaluating the surface characteristics of water atomized Cr-Mo pre-alloyed powder by means of surface sensitive analytical techniques. Papers II, IV-VI and VIII focus on the effect of the sintering atmosphere on the evolution of the surface characteristics of Cr-Mo pre-alloyed powder during the sintering process and how different process parameters will affect them. The investigation was carried out by examining the fracture surfaces of powder compacts of different green densities which were heated/sintered in different atmospheres with different heating rates in the temperature range of 700-1200°C and for a time interval of 1-30min. Thermogravimetric analyses were also performed in order to mark the differences in the reduction/oxidation processes between the different atmosphere compositions. The amount of residual oxides was correlated with the mechanical performance of the produced specimens by performing Charpy impact testing. Finally investigation of optical micrographs was also performed in order to examine the extent of the efficient oxide reduction and to verify the obtained microstructure.

6.1 Powder Characterization

Water atomized Cr-Mo pre-alloyed steel powder (Astaloy CrM: Fe-3Cr-0.5Mo) was chosen as the model material for developing a consistent method for evaluating the oxide distribution both on the surface and interior of the powder. High resolution scanning electron microscopy in combination with EDX analysis, X-ray photoelectron spectroscopy and Auger electron spectroscopy were used in order to study the type, composition, morphology and distribution of oxide products.

The XPS analysis revealed that the metal particles were mainly covered by a thin homogeneous Fe-oxide layer and some nano-sized particulate features that were complex Fe-Cr-Mn-Si-oxides. The thickness of the Fe-oxide layer was estimated independently by using both XPS and AES in combination with Ar^+ etching (**Fig. 36**). One very important observation made with the AES was the fact that the chromium signal appeared only after sufficient removal of the surface oxide layer. This indicates that it originates from the bulk and that no chromium is contained in the surface oxide layer.

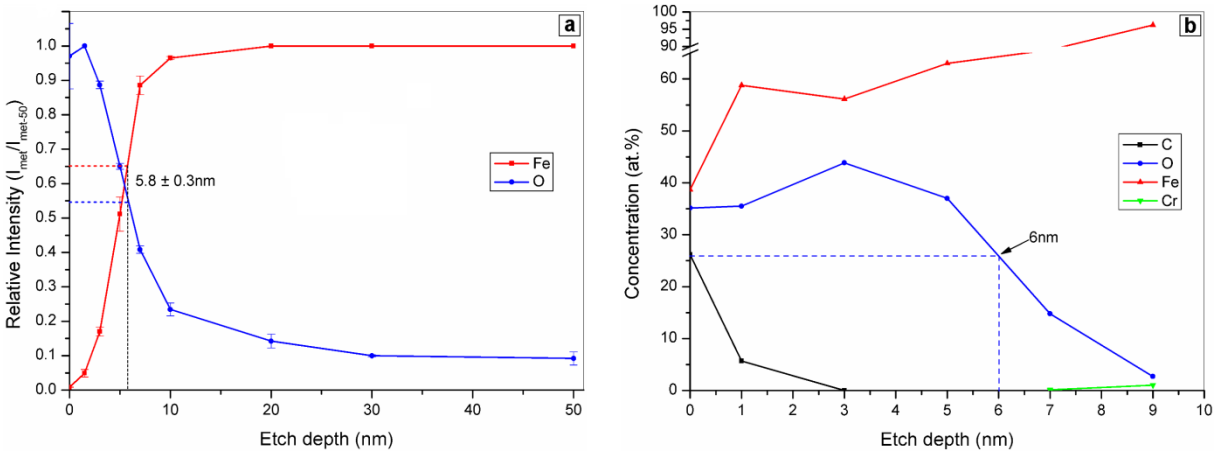

Fig. 36. *Estimation of the Fe-oxide layer thickness with a) XPS and b) AES (Paper VII).*

By following the methodology presented in previous studies [64, 70, 71] the oxide surface coverage was calculated using the extracted intensities of oxides and their respective densities (See also **Appendix A**). The results are presented in the table below and show that 93.5% of the surface is covered by Fe-oxide.

Table 4. *Surface coverage (A) in (%) of the respective oxide phases present of the surface of Astaloy CrM powder after 1.5nm of ion etching*

	$A^{OX}_{Fe_2O_3}$(%)	$A^{OX}_{Cr_2O_3}$ (%)	A^{OX}_{MnO} (%)
Material A	93.45±0.27	5.68±0.29	0.88±0.03

The appearance of the powder surface (**Fig. 37**) along with the morphology and size of the particulate features (**Fig. 38**) was verified by high resolution SEM observations combined with EDX analysis and complemented by AES analysis of the powder surfaces.

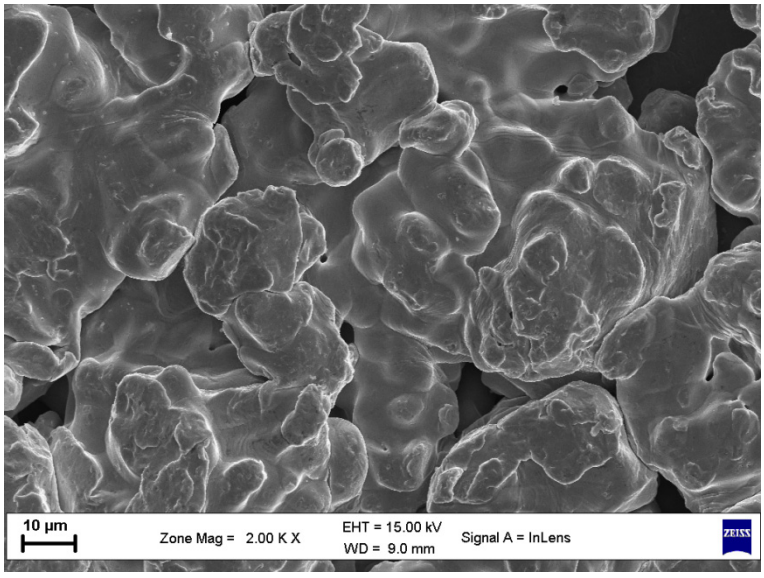

Fig. 37. *SEM micrograph of the powder surface (Paper VII).*

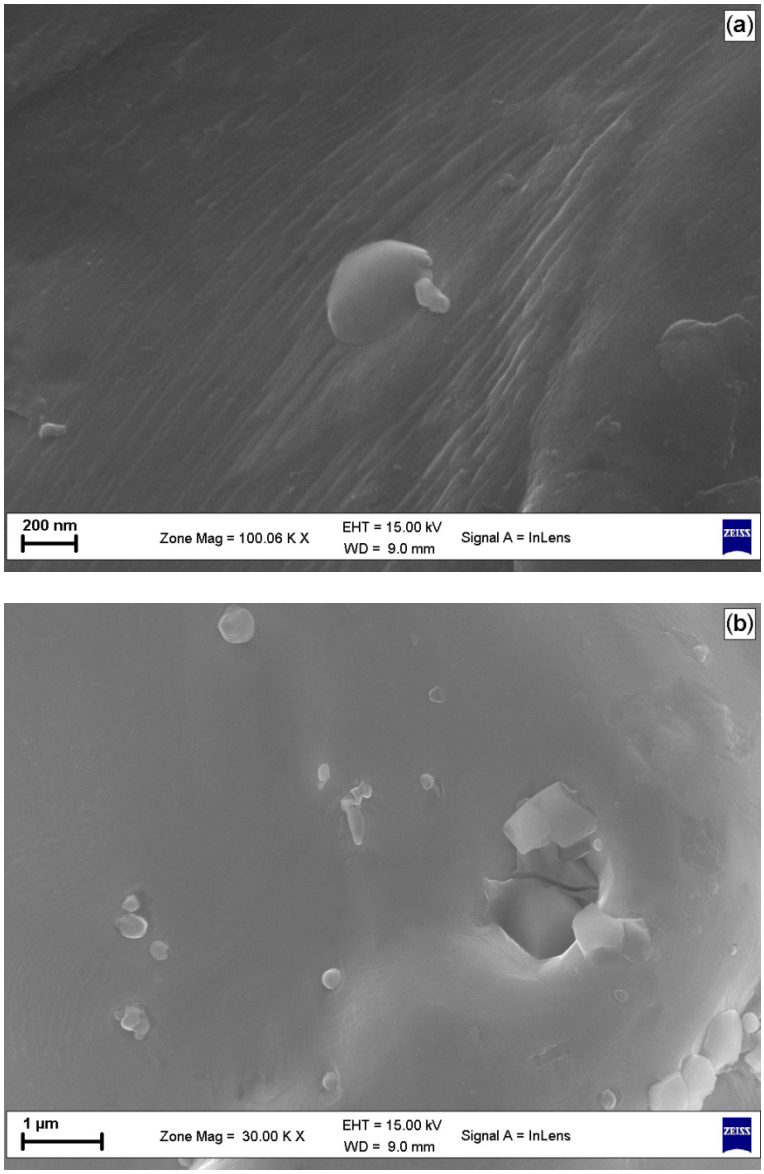

Fig. 38. *High resolution SEM micrographs showing a) typical particulate oxide and b) particulate oxides and more rarely observed agglomerate (Paper VII).*

In Papers I and III the proposed model for the types of features which were observed was: i) typical spherically shaped ones with size up to ~200nm (**Fig. 38a**) and ii) rarely registered larger agglomerates of irregular shape and with size of a few microns (**Fig. 38b**). However more extensive AES studies in combination with compositional depth profiling indicated that the typical individual particulate oxides have basically a "hemispherical" shape and thus a revised model for the surface oxide was proposed (**Fig. 39**).

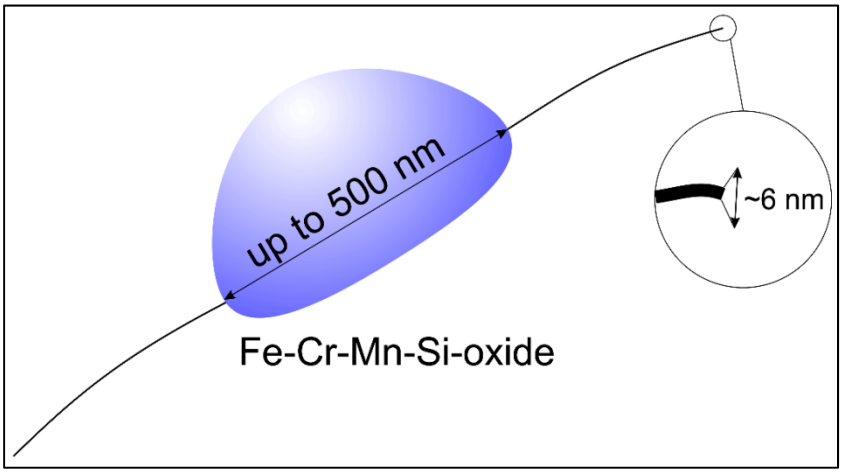

Fig. 39. *Revised model for the surface oxide covering the powder particles (Author's illustration).*

The EDX analysis performed on the observed particulates (**Fig. 40**) showed high content of strong oxide forming elements like Cr, Mn and Si on both the fine particulates and their agglomerates. The strong oxygen signal in combination with the detected enrichment of strong oxide formers suggests that the observed particulates could be complex oxides.

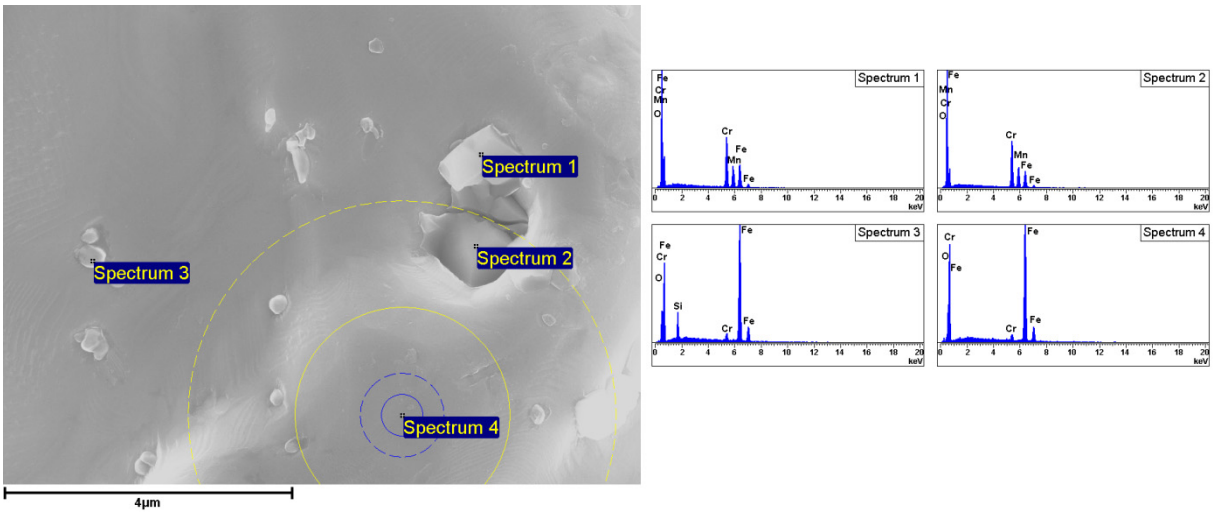

Fig. 40. *EDX analysis of particulate features, agglomerate and matrix (reference)(Paper VII).*

The high resolution capabilities of the AES were taken advantage in order to analyze individual surface features by performing compositional depth profiling on them. It has to be noted though that this analysis required great effort with the main challenge being in fine tuning the instrument and finding the proper setup in order to perform accurate analysis. Nevertheless for the first time it was possible to carry out dedicated high resolution studies on individual surface features (Paper VII). It was verified that the individual particulate feature were basically Si-based oxides or Cr-based oxides with the additional presence of nitrogen being observed for the first time (traces of nitrogen were also detected with the XPS) (**Fig. 41**). The larger features were heterogeneous in composition and were basically agglomerates of the afore mentioned oxides but with the oxide phases being present more as adjacent particulates "glued" together and not as a layered structure.

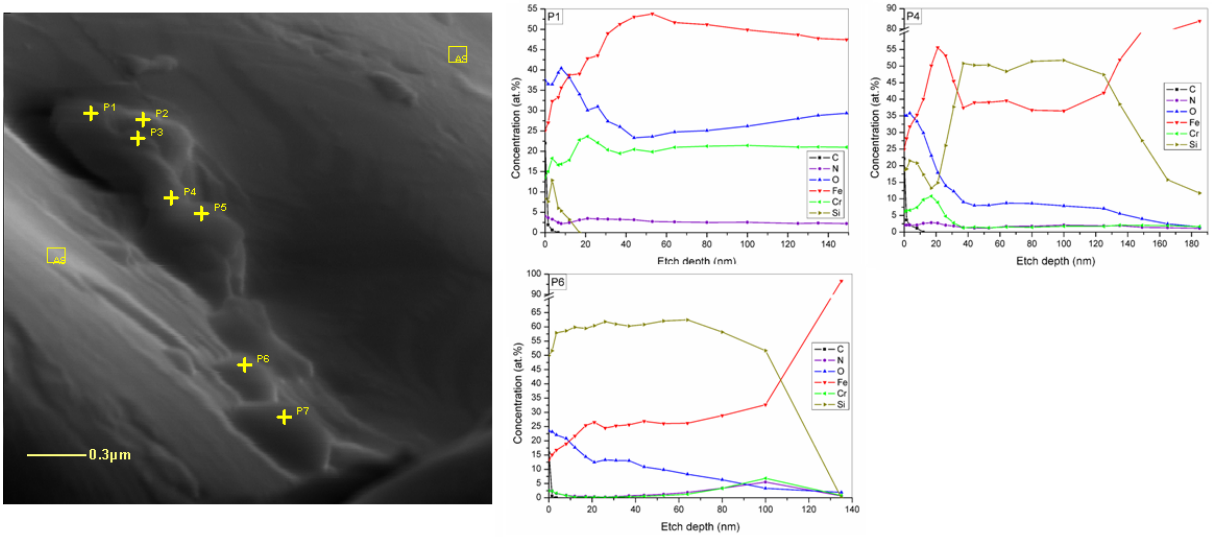

Fig. 41. *AES analysis area showing individual particulate features and agglomerate and the compositional depth profiles corresponding to selected analysis points (Author's experimental results).*

Finally in Paper I a novel method was developed for the investigation of internal inclusions using EDX mapping on cross-sections of powder particles (**Fig. 42**). This study revealed the occasional presence of internal oxides with high contents of Cr and Mn and with size below 1µm.

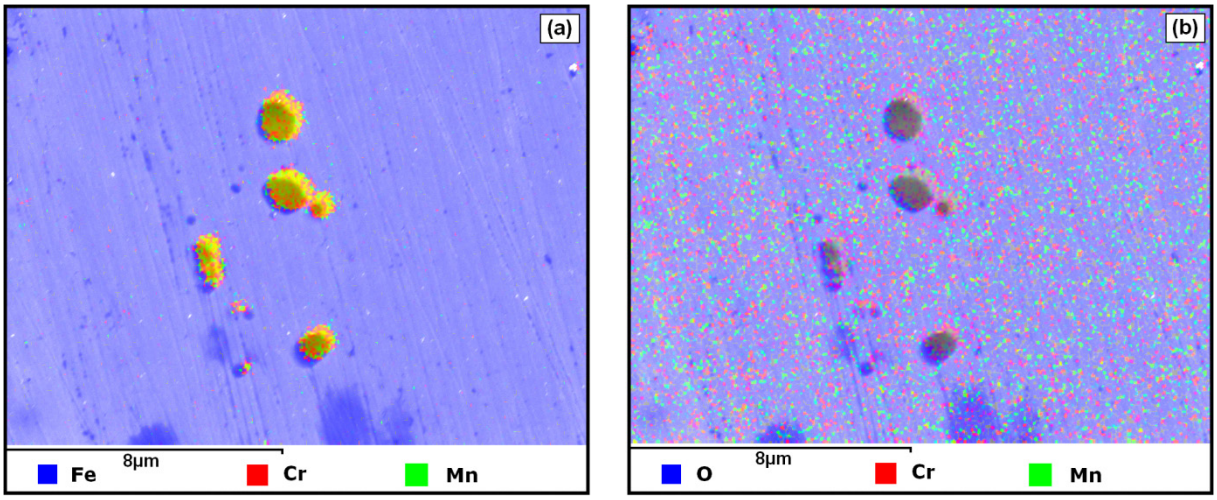

Fig. 42. *EDX mapping of powder particle cross-section showing the relevant elemental distribution (Paper I).*

This part of the research work dealt with the characterization of the type, composition, morphology and distribution of the particulate features in both the surface and the interior of Cr-alloyed water-atomized powder and indicated that a full picture concerning particulates characteristics can be drawn only by combining surface sensitive analytical techniques and high resolution imaging.

6.2 Surface Reactions during Sintering

The effect of the sintering atmosphere composition on the surface chemistry of Cr-alloyed steel powders during the sintering process was investigated in Papers II and IV-VI. Impact testing was performed on specimens heated/sintered in nitrogen-based atmospheres with varying hydrogen content as well as vacuum and the produced fracture surfaces were examined by means of high resolution SEM. For Paper VIII additional experiments were carried out where higher heating rates were employed on specimens of normal (7.0 g/cm^3) and higher (7.25 g/cm^3) green density in a selected atmosphere.

In Papers II and IV the investigated material system was water atomized Cr-Mo alloyed powder of nominal composition Fe-1.5Cr-0.2Mo (Material E) whereas in Papers V, VI and VIII the focus was put on Material A with composition Fe-3Cr-0.5Mo. For both material systems the fractographic investigation revealed the positive effect of the presence of hydrogen in the atmosphere – even in small amounts – on the reduction of the less thermodynamically stable Fe-oxide according to **Re. 10** during the heating stage and up to 800°C. This was reflected on the inter-particle connections which were much better developed in comparison with pure nitrogen atmosphere (**Fig. 43**) or vacuum as well as on the thermogravimetric studies performed for Material A (**Fig. 44**).

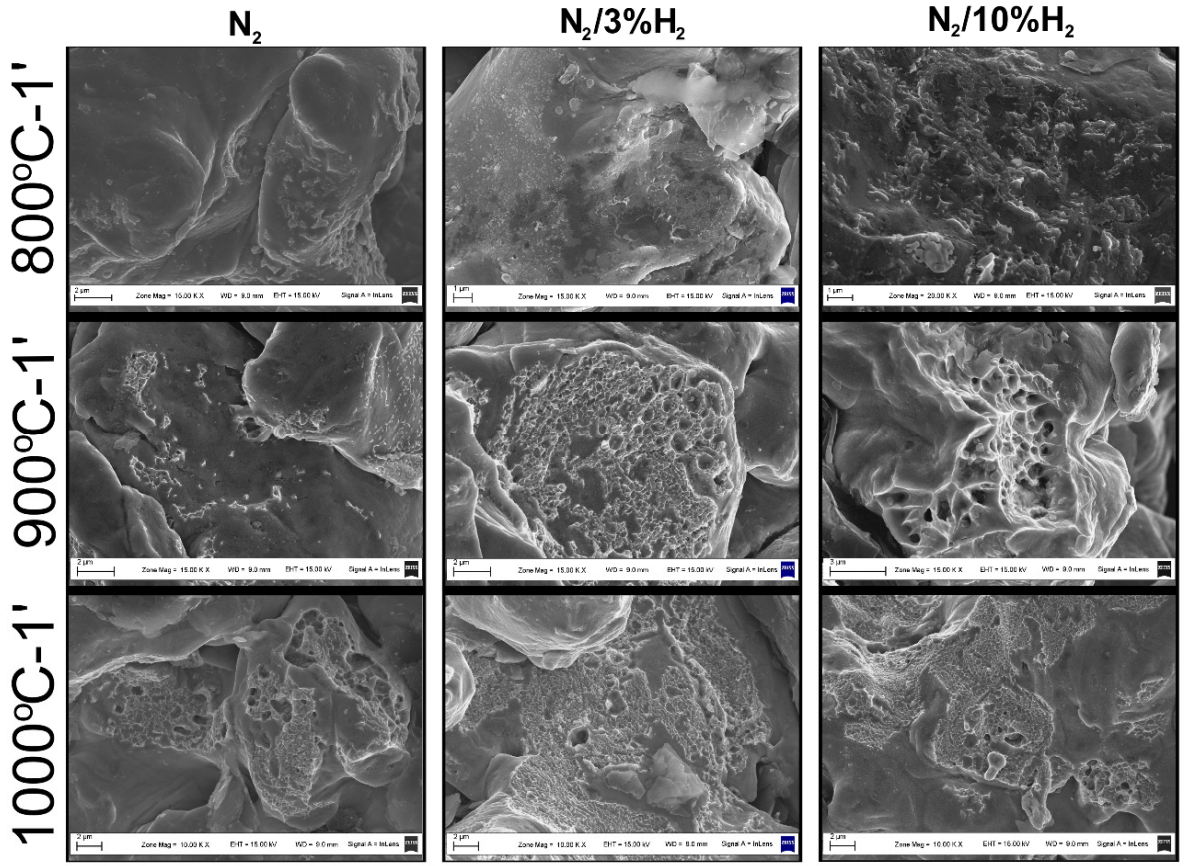

Fig. 43. *Appearance of fracture surfaces of material A+0.5C in the temperature range of 800-1000°C (Paper V).*

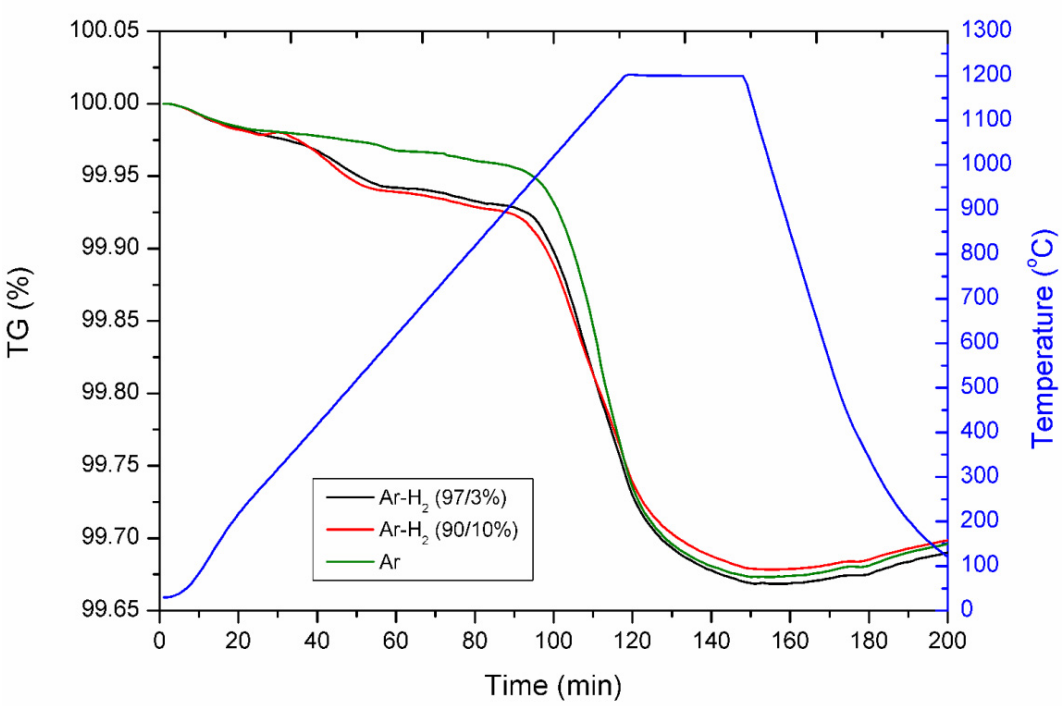

Fig. 44.*TG curves for samples of material A+0.5C simulating a sintering cycle at 1200°C for 30' in atmospheres with varying hydrogen content (Paper VIII).*

The temperature range between 800 and 1000°C is of paramount importance for the efficient reduction of the surface oxide and respectively for the proper sintering of such materials. If now the gas containing atmospheres (N_2, N_2/3%H_2 and N_2/10%H_2) are compared then the presence of hydrogen offers an additional advantage since apart from acting as reducing agent, it also participates in the water gas reaction (**Re. 24**) and shifts the reaction towards the CO formation which in turn makes the conditions more reducing in comparison with pure nitrogen.

Rapid and pronounced development of inter-particle connections takes place for the vacuum heated samples as soon as 900°C is reached (**Fig. 45**). The reason for this is the better "microclimate" inside the compact due to the dynamic vacuum which removes all the reaction products as well as the increase of the reducing activity of carbon with increasing temperature. Consequently, surface oxide is enclosed inside the inter-particle necks during vacuum sintering (**Fig. 46**). This rapid enclosure of surface oxide is also reflected in the high temperature sintered specimens that show larger amount of oxide inclusions or their agglomerates in the case of vacuum which in turn result in lower impact energy values.

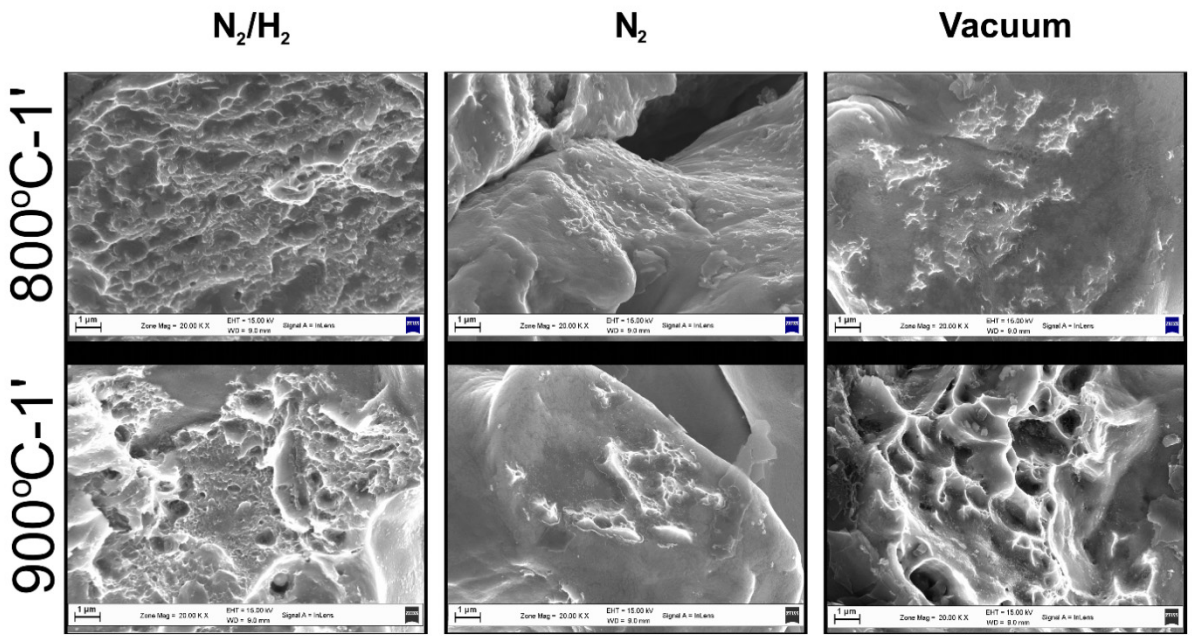

Fig. 45. *Change in the appearance of the fracture surfaces of material E in the critical temperature range of 800-900ºC – effect of the local microclimate (Paper IV).*

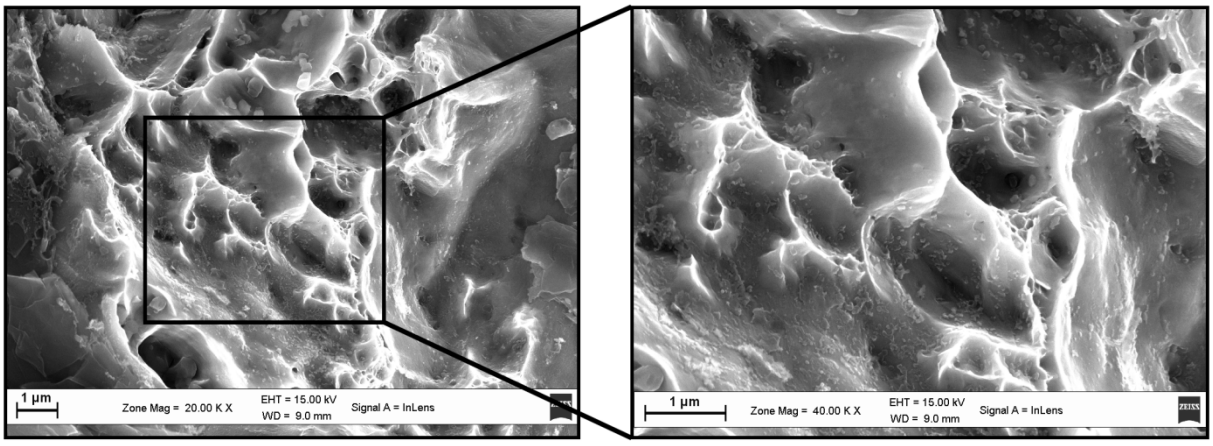

Fig. 46. *Developed inter-particle connections for sample of material E heated up to 900°C in vacuum (Paper IV).*

The development of the inter-particle necks leads to enclosure of the surface oxide layer inside them (**Fig. 46**). The particulate features originating from the initial powder surface are growing at the expense of the thermodynamically less stable Fe-oxide layer by consuming the released oxygen (in any form). The growth mechanisms of the particulates could be related either to the intensive mass-transfer of strong oxide forming elements (Cr and Mn) with increasing temperature, from inside the powder to its surface and a net transfer of surface bound oxygen connected with Fe-oxides to form more stable particulates. The balance between these two kinds of mechanisms supposedly depends decisively on the heating rate. The above was the driving force for investigating the effect of different heating rates (Paper VIII) and it will be discussed further below.

The extent of the reduction of the surface oxide which is connected with the carbon dissolution will determine the microstructure, as was observed from the metallographic

investigation of sample cross-sections (**Fig. 47**). Graphite was encountered up to 1000°C, especially in the interior of the samples.

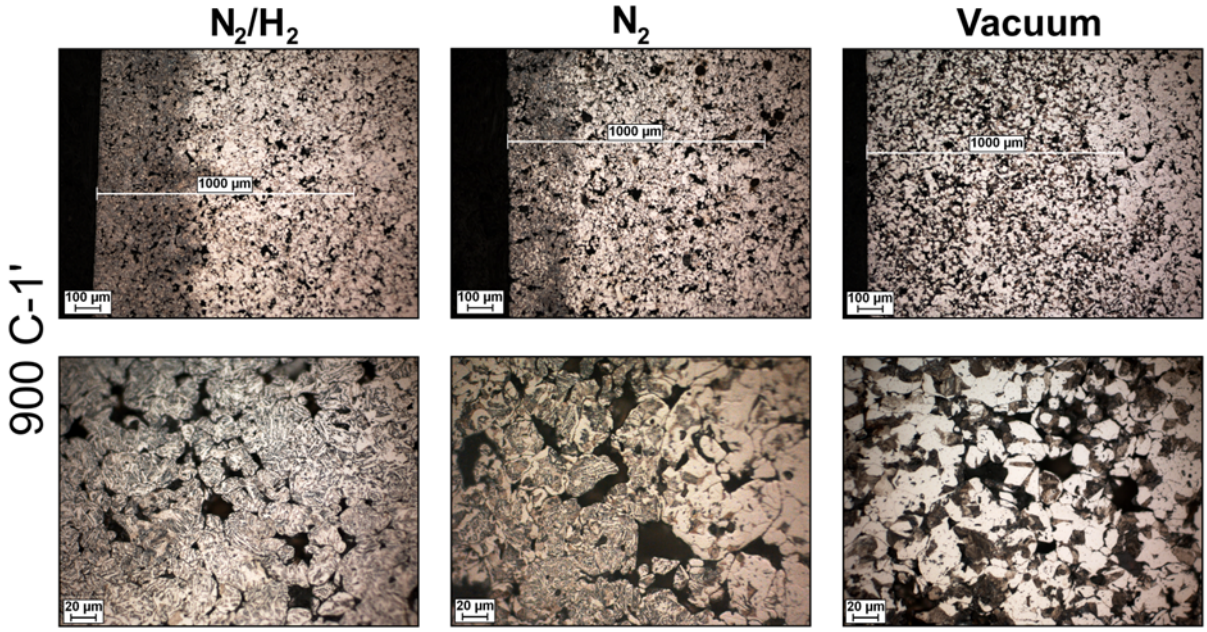

Fig. 47. *Etched microstructure of material E+0.5%C after heating at 900°C – In the case of the gas containing atmospheres and vacuum respectively bainite and pearlite were present. The extend of the surface oxide reduction and consequently the carbon dissolution can be seen from the micrographs of the upper row (Paper II).*

Comparing the gas containing atmospheres (Paper VI) the area of efficient surface oxide reduction differs for the different atmospheres, it is larger for the samples heated in the $N_2/10\%H_2$ blend, smaller for the $N_2/3\%H_2$ and even smaller for the pure nitrogen.

The extend of the efficient surface oxide reduction was significantly decreased when the green density of the compact increased (Paper VIII) as it was observed for samples of higher density ($7.25 g \cdot cm^{-3}$) sintered in $N_2/3\%H_2$. Consequently graphite remained undissolved even after reaching 1120°C. This implies that even though at such densities the porosity cannot be considered closed, the penetration of the atmosphere in the interior of the compact and the removal of the reaction products is not sufficient, and thus it is not possible to develop the desired "microclimate" that will enable the efficient reduction of the surface oxide.

Concerning the particulate oxides which were included inside the developing necks during the heating stage a change in their morphology and size is observed with increasing temperature and after sintering they are mostly spherical and small (<1µm). The amount of oxide inclusions in the neck region is far greater than the amount of particulate features on the surface of the original powder. This implies that inside the neck, in addition to the existing enclosed particulate features, particulate oxides of high thermodynamic stability are also formed by transformation of the Fe-oxide residues due to the transfer of Cr and Mn through various mechanisms [36], to the neck area. By performing some basic calculations it was shown that the amount of Mn available in a considered "effective" volume is not a limiting factor for the formation and growth of oxide inclusions in the neck region (Paper VIII).

As soon as 1120°C is reached the coalescence and agglomeration of these inclusions is registered for all conditions (**Fig. 48**) but further increase in the sintering time and temperature leads to their partial reduction. The highest amount of residual oxides is observed for the vacuum processed samples whereas the ones sintered in hydrogen containing atmospheres show the smallest. As was mentioned earlier the above was a result of the intensive development of the inter-particle connections during the heating stage for the vacuum processed samples.

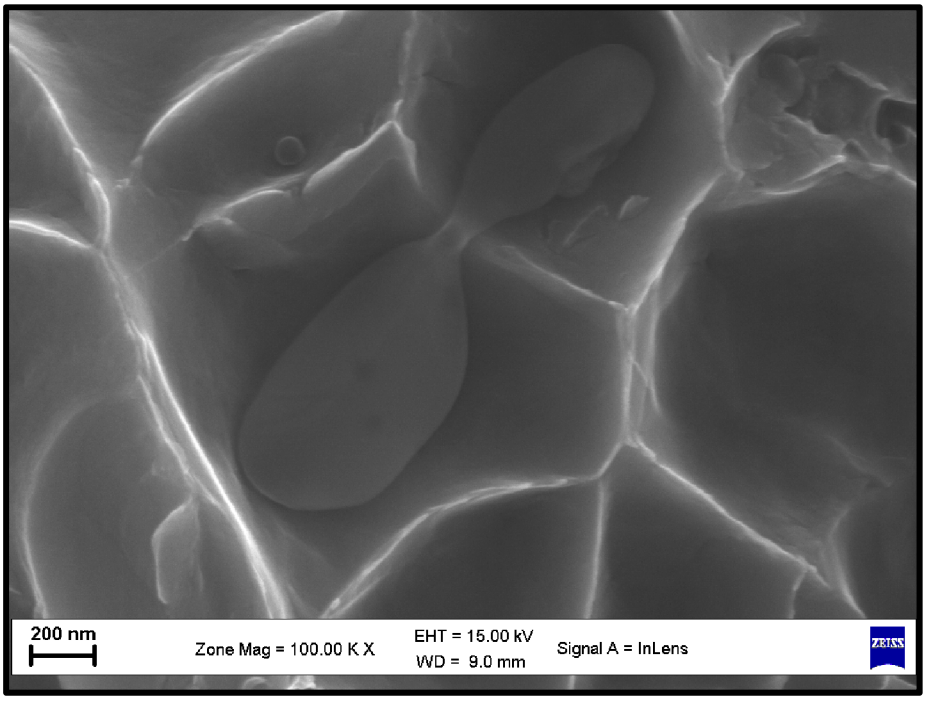

Fig. 48. *SEM micrograph showing the coalescence and agglomeration of oxides enclosed inside a sinter-neck (Paper VII).*

The particulate oxides observed through all the experimental series are rich in strong oxide forming elements (Cr and Mn) with their relative content remaining the same with increasing temperature, showing a Cr:Mn ratio equal to 2:1 even after sintering at 1200°C (**Fig. 49**). It is therefore assumed that these oxide inclusions are Cr-Mn spinel oxides which have among the highest thermodynamic stability for the system under investigation. Although the EDX analyses cannot be used quantitatively due to the large interaction volume of the technique and the local surface roughness of the sample it is observed that the oxide inclusions are changing in chemistry in accordance with the thermodynamic stability of the oxides (**Fig. 50**) [3, 53, 64, 97, 98]. The initial iron oxide is essentially Fe_2O_3 [63] which is reduced in metallic iron and partially to FeO-oxide. Transformation to Fe-based spinels (Fe_2MnO_4 and Cr_2FeO_4) could be expected up to a certain extent as well as it was shown in [12, 42]. The iron part of those spinels will be reduced with increasing temperature (above 1000°C) and in combination with the more intensive transport of Cr and Mn they transform to $MnCr_2O_4$. Further increase in temperature and time (above 1120°C) leads to partial reduction of the Cr-Mn-spinel and the seldom observed oxides can be enriched in Si.

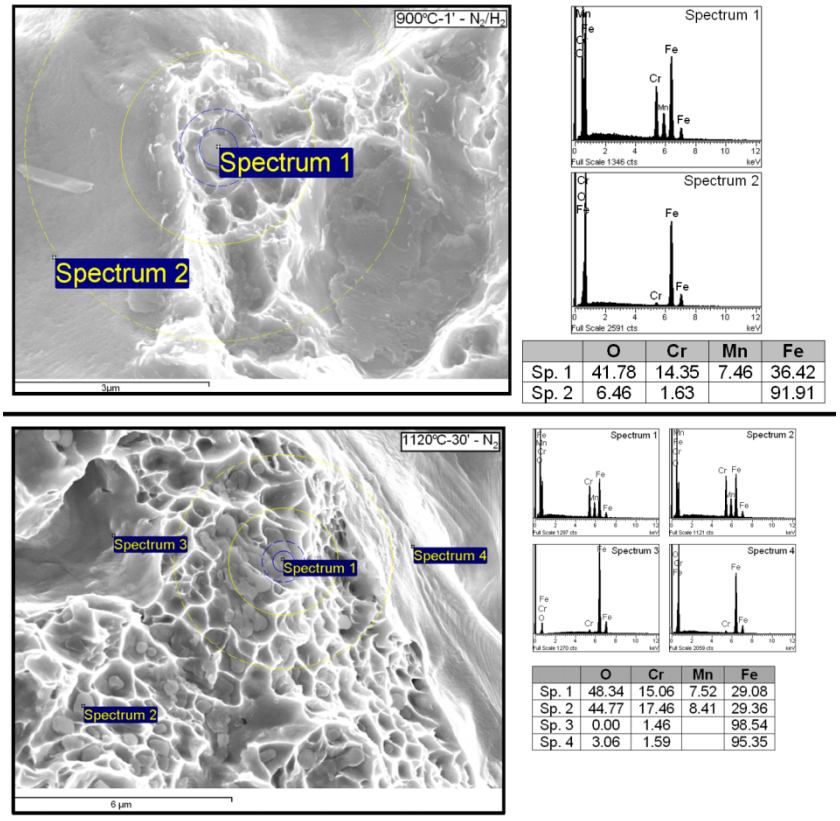

	O	Cr	Mn	Fe
Sp. 1	41.78	14.35	7.46	36.42
Sp. 2	6.46	1.63		91.91

	O	Cr	Mn	Fe
Sp. 1	48.34	15.06	7.52	29.08
Sp. 2	44.77	17.46	8.41	29.36
Sp. 3	0.00	1.46		98.54
Sp. 4	3.06	1.59		95.35

Fig. 49. *SEM and EDX analysis of particulate features and agglomerates during the heating (900°C) and sintering (1120°C-30') stage (Paper II).*

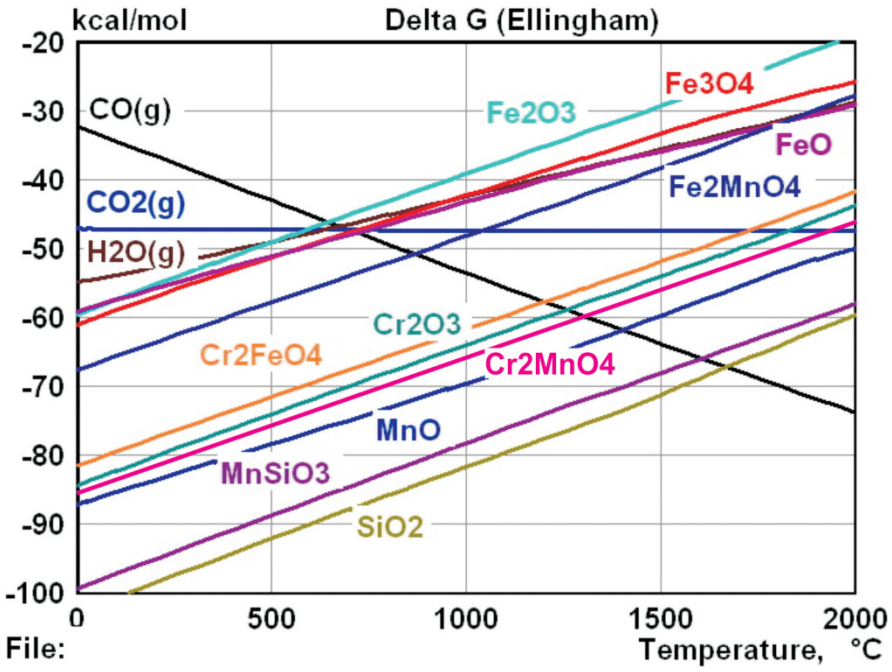

Fig. 50. *Ellingham-Richardson diagram illustrating the thermodynamic stability of selected oxides (Plotted with HSC Chemistry 7.1)-(Paper VIII).*

It was mentioned earlier that the amount of oxide inclusions in the developed necks after sintering was greatly affected by the employed heating rate. The above was verified in the experiments performed with varying heating rate in a $N_2/3\%H_2$ atmosphere (Paper VIII). It was observed that the optimum heating rate was $30°C \cdot min^{-1}$

which was high enough in order to pass through the critical temperature range 800-1000°C and have sufficient surface oxide reduction and in the same time to avoid extensive re-oxidation (as for the 10°C·min^{-1}). Furthermore this heating rate was not excessively high (as the 50°C·min^{-1}) in order for the inter-particle necks to develop intensively after 900°C, as soon as partial reduction of the surface oxide occurred, which in turn would lead into the enclosure of a large amount of particulate oxides. The above were reflected on the impact energy values (**Fig. 51**).

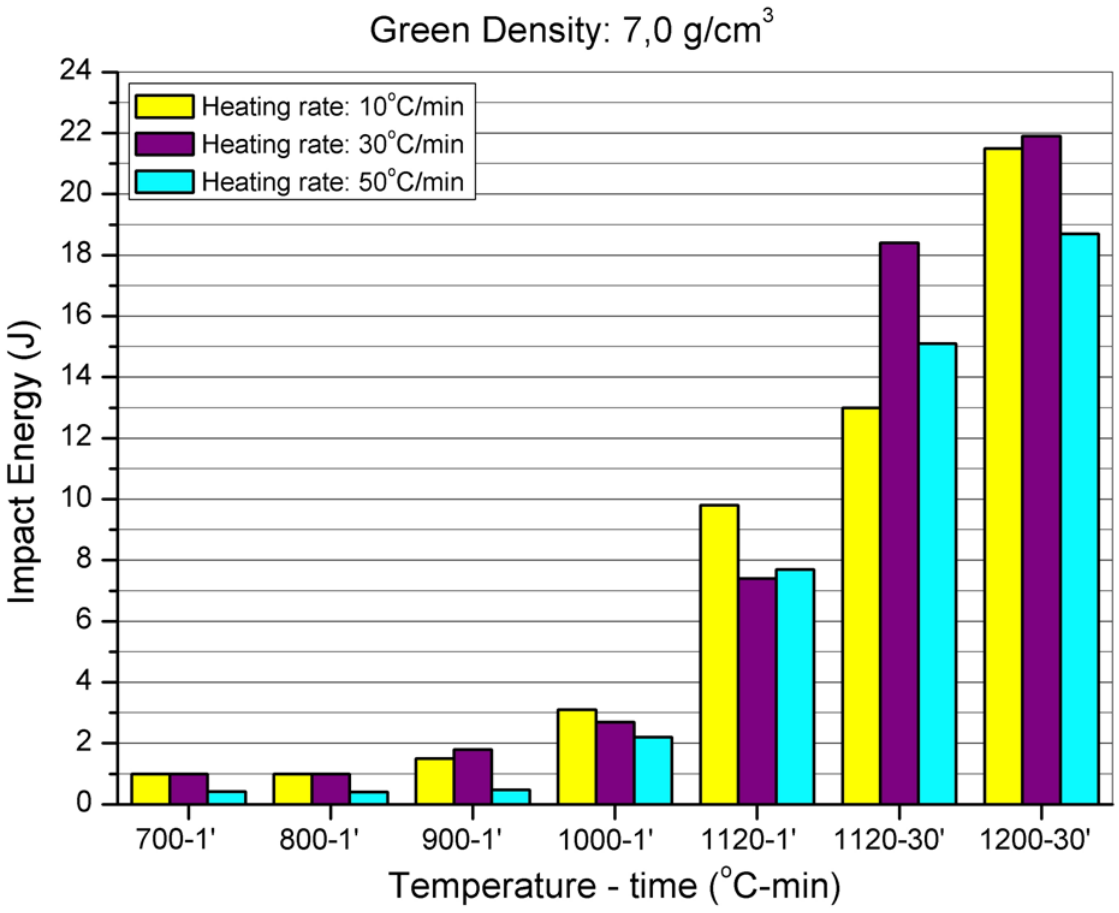

Fig. 51. *Impact energy values for samples heated/sintered in N_2/3%H_2 with different heating rates (Author's experimental results).*

Higher green density will also have an effect on the amount of residual oxides observed after sintering (Paper VIII). As explained earlier the penetration of the sintering atmosphere will be insufficient to provide efficient removal of the oxide products from the pore and thus to develop a proper reducing "microclimate". Additionally the larger amount of contact points will result from one hand to the development of more sinter-necks but on the other hand it will also lead to the enclosure of more particulate oxides during the neck development. The optimum heating rate in this case seems to be less than 30°C/min in comparison with the samples of lower density. The above must be taken into consideration when sintering high density components and necessary adjustments must be made in the heating rate and/or apply higher atmosphere flows.

6.3 Main Conclusions and Contribution to the Field

The use of alloying elements such as chromium in water atomized steel powders has been met with skepticism due to its high sensitivity to oxygen which can lead to the formation of thermodynamically stable oxides which will be difficult to reduce during the sintering process. The present research work has complemented and added new knowledge on previous studies in the field of powder characterization of Cr-pre-alloyed steel powders. Furthermore deep understanding was obtained on the phenomena which take place during the sintering process and especially during the heating stage and are related to the surface chemistry of the powders. In the long term it is possible to utilize this knowledge in order to create a process map for the efficient sintering of such powder grades which will result in manufacturing of the components with superior mechanical performance.

The most important conclusions of this research can be summarized in the following:

- The combination of the surface sensitive analytical techniques showed the presence of a heterogenous oxide on the powder surface. This oxide consisted of a thin (~6nm) Fe-oxide layer (consisting of Fe_2O_3) which covered approximately 94% of the surface and thicker particulate products rich in Cr, Mn and Si. These products were mainly oxides and were commonly encountered as "hemispherical" particulates with their diameter being <0.5μm. More rarely, larger agglomerates of the particulates mentioned before were also observed.
- In the interior of the powder particles similar particulate features were encountered. They were slightly larger oxides rich in Cr and Mn with no Si present.
- It is the efficient reduction of the Fe-oxide layer that will affect the onset of the development of inter-particle necks. Nevertheless the amount and characteristics of residual oxide inclusions inside the necks will affect the final mechanical properties of the sintered component.
- The development of a suitable local atmosphere "microclimate" in the interior of the compact is of paramount importance for the efficient sintering of the compact and is greatly affected by the atmosphere composition and purity, the heating rate and the green density of the compact.
- The presence of hydrogen – even in small amounts – has a positive effect on the reduction of the Fe-oxide because it acts as a reducing agent in the early stages of heating and it participates in the "water gas" reaction thus shifting the equilibrium into more reducing conditions.
- The temperature range during the heating stage between 800°C and 1000°C is considered to be the most critical due to the risk of enclosure of surface oxide inside the developing inter-particle connections and further transformation of Fe-based oxides into the more stable Cr-Mn-spinels which at elevated temperatures can coalesce into larger agglomerates, see **Fig. 52**. Partial reduction of the oxide inclusions and their agglomerates can be achieved at higher sintering temperatures if the necessary reducing conditions are applied

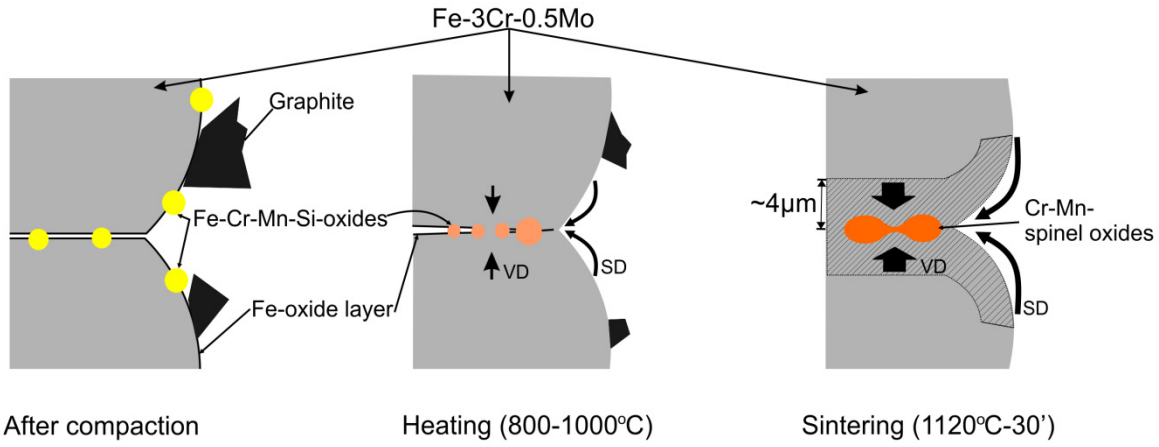

Fig. 52. *Model for the enclosure, growth and formation of oxide inclusions inside the sinter necks during the sintering process (Author's illustration – Paper VIII).*

- The heating rate is a crucial parameter in the sintering of Cr-alloyed powders since it must be enough for the reduction of the surface oxide to take place without risking extensive reoxidation and on the same time it must not be too high because otherwise, intensive sinter-neck development will take place which will result in enclosing large amounts of residual surface oxides.

7 Suggestions for Future Work

In this work special attention was given in the formation and growth of spinel oxides, especially the most stable for this composition $MnCr_2O_4$ spinel, inside the sinter necks. Additionally the coalescence and agglomeration of such individual oxide inclusion into larger agglomerates during the sintering stage has been revealed (**Fig. 53**). This in turn can be considered beneficial from mechanical performance point of view since the coverage of the neck area from inclusions is reduced (see also Paper VIII) which can be translated in improved local ductility. Therefore it is important to investigate the mechanism of the agglomeration and study the driving force behind it. Additionally their effect on mechanical properties, especially fatigue, for high density components should be investigated.

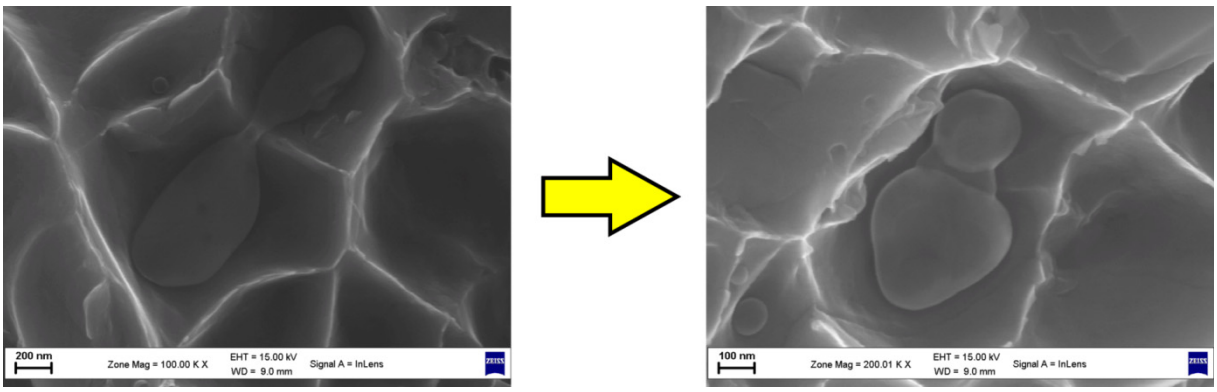

Fig. 53. *Coalescence and agglomeration of inclusions during sintering at 1120°C (Author's experimental results).*

Another very interesting issue from both scientific and technological point of view is the mechanisms of reduction of inclusions inside sintered necks. It is already observed (Papers II, IV-VI and VII) that sintering at higher temperature reduces the amount of oxide inclusions and their agglomerates inside the sinter necks. The most feasible reduction mechanism is presumably through carbothermal reactions involving dissolved carbon. It is therefore important to clarify this reduction mechanism and how the mass-transfer of the different reaction products from the neck volume, is taking place. A decisive factor for reaching the understanding of this mechanism is the local conditions around such inclusions – if these oxides are incoherent inclusions inside the metal matrix or there is space (void) around them (**Fig. 54**).

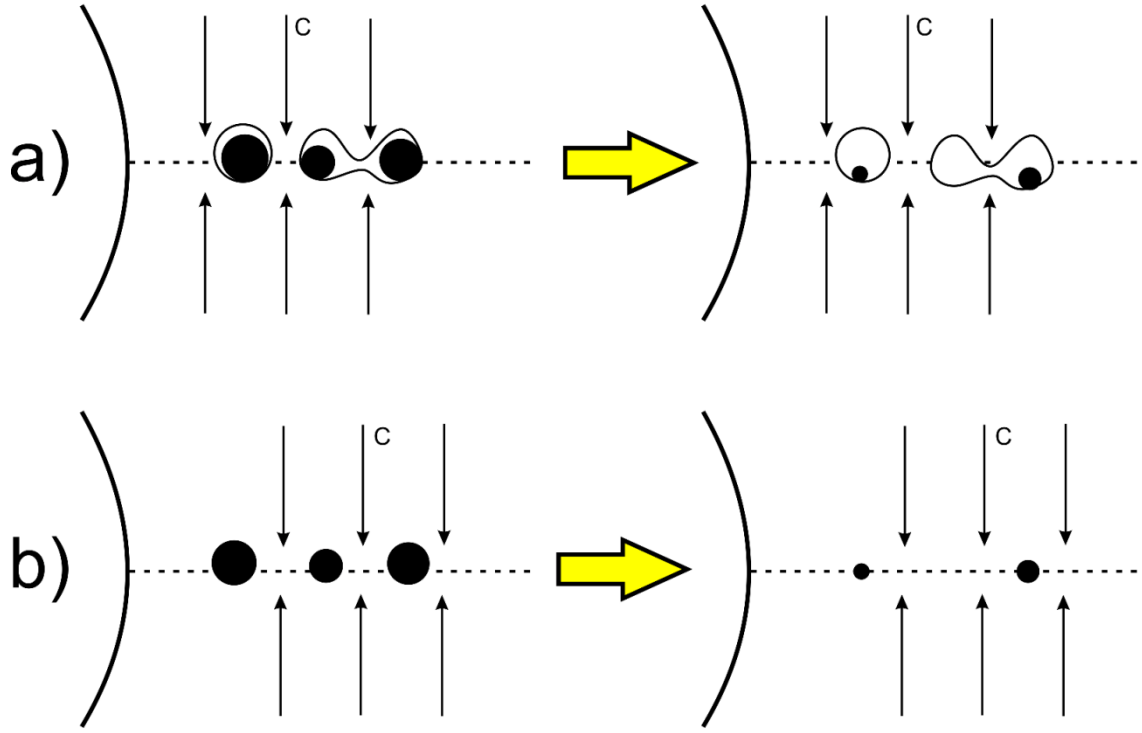

Fig. 54. *Reduction of oxide inclusions in the sinter neck a) with and b) without some space around them (Author's illustration).*

Finally, since carbon is identified as the main agent for the reduction of surface oxides, it would be very interesting to investigate how different graphite grades can affect the reduction during different temperature intervals. Hence, considering the effect of the presence of graphite and the powder size on oxide reduction, the question is if it would be technologically feasible to combine some of them in order to tailor carbon activity at different temperature intervals.

8 Appendices

Appendix A – Oxide surface coverage calculations

In the case of XPS, the recorded intensity I from a surface layer of thickness α and unit area is given according to [88] by:

$$I = Y \cdot D \cdot \lambda \cdot cos\theta \cdot \left[1 - exp\left(-\frac{\alpha}{\lambda cos\theta}\right)\right] \quad (27)$$

Where Y is the relative photoelectron yield, D is the atomic density, λ is the electron mean free path and θ is the angle between the axis normal to the surface of the specimen and the spectrometer axis, which in the experimental setup of the study is 45° (**Fig. 55**)

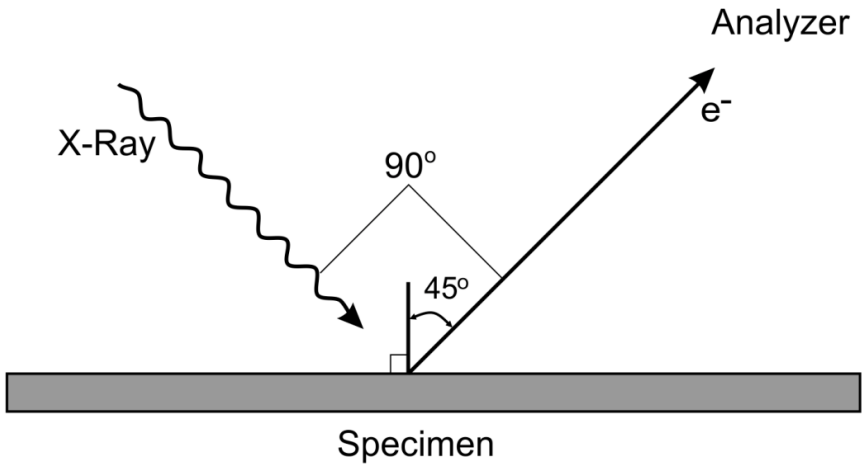

Fig. 55. *Experimental of the XPS analysis in the present study.*

Since 95% of the intensity of the signal is originating from a depth of 3λ [88, 89] as evidenced from **Eq. 27**, then any layer thicker than 3λ can be considered as infinitely thick and thus **Eq .27** is simplified to:

$$I = Y \cdot D \cdot \lambda \cdot cos\theta \quad (28)$$

The relations above do not take into consideration the spherical shape of the powder and the analyzed area is treated as flat [64, 66-71].

For the surface coverage calculations the following model [68-71] was considered:

- The surface oxide layer is inhomogenous in thickness consisting of thick oxide islands and thin Fe-oxide layer in between
- The analyzed surface is considered flat, which is a valid approximation for the calculations to follow since factors accounting for powder shape will cancel in the final surface coverage expression
- The contribution from the metal phase underneath the oxide particles can be neglected since their thickness is supposed to be larger than the attenuation length of the photoelectrons $t_{ox} \gg 3\lambda_{ox}$
- The area between the oxide particles is considered as oxide free, which is valid after the removal of the Fe-oxide layer with ion etching (~6 nm)

The measured intensity from a metallic element M in its cation state (I_M^{OX}) for an oxide particle on the powder surface is given by:

$$I_M^{OX} = Y_M^{OX} \cdot D_M^{OX} \cdot \lambda_M^{OX} \cdot A_M^{OX} \cdot cos\theta \quad (29)$$

The element in its metallic state from the uncovered surface will give the signal with intensity:

$$I_M^{met} = Y_M^{met} \cdot D_M^{met} \cdot \lambda_M^{met} \cdot A_M^{met} \cdot cos\theta \quad (30)$$

Where Y_M^{OX} and Y_M^{met} are the relative photoelectron yields for the oxide and metal respectively; D_M^{OX} and D_M^{met} are the cation densities; λ_M^{OX} and λ_M^{met} are the electron attenuation depths of the emitted photoelectrons in oxide and metal, respectively; A_{MO}^{OX} is the area fraction covered by the oxide MO and A_M^{met} is the area fraction which is oxide-free.

One of the most important steps for these calculations is the determination of the relative photoelectron yields for the different elements and compounds for the experimental setup of this study. In order to achieve this it was assumed that after the final etching (~50 nm) all the surface products (oxide particles and Fe-oxide layer) are completely removed and therefore the surface coverage of the metallic Fe then is $A_{Fe}^{met} = 100\%$. Therefore (**Eq.30**) will become:

$$I_{Fe}^{met} = Y_{Fe-cor}^{met} \cdot D_{Fe}^{met} \cdot \lambda_{Fe}^{met} \cdot cos\theta \quad (31)$$

From which the only unknown now is the corrected yield Y_{Fe-cor}^{met}. After calculating Y_{Fe-cor}^{met} for metallic Fe the relative yields for the other elements and compounds can be calculated proportionally from previously published data [64, 68-71]. All the data used in the calculations are presented in **Table 5**. At this point it has to be mentioned that there is no distinction for the type of compounds of the particulate oxides on the powder surface which means that they can be simple compounds like M_xO_y as well as more complex mixed oxides like spinels. Therefore, for the sake of simplicity, it is assumed that all oxides are simple monolithic compounds.

Table 5. *XPS parameters used in this study, Y_M values refer to prior derived relative photoelectron yields [64, 68-71], $Y_{M\text{-}cor}$ represents the corrected ones derived from the present analyses.*

Element/compound	D (mol·cm^{-3})	λ (nm)	ϒ (kc·eV·cm^3·s^{-1}·Å^{-1}·mol^{-1})	
			Y_M	Y_{M-cor}
Fe	0.141	1.2	24.8	40.9
Fe_2O_3	0.066	1.5	18	29.7
Mn	0.135	1.3	22.6	37.3
MnO	0.077	1.5	27.9	46.1
Cr	0.138	1.3	21.7	35.8
Cr_2O_3	0.069	1.6	23.8	39.3

The total coverage by oxides for each etch depth will be:

$$A^{OX} = \sum_M A_{MO}^{OX} \quad (32)$$

$$A^{met} = 1 - A^{OX} \quad (33)$$

Eq. 33 is essentially valid for Fe since the other elements are present only in oxide state. The fraction of each oxide MO out of the total amount of surface oxides will be:

$$R^{MO} = \frac{A^{OX}_{MO}}{A^{OX}} \rightarrow R^{MO} = \frac{\frac{I^{OX}_M}{D^{OX}_M \cdot \lambda^{OX}_M \cdot Y^{OX}_{M-cor}}}{\sum_M \left(\frac{I^{OX}_M}{D^{OX}_M \cdot \lambda^{OX}_M \cdot Y^{OX}_{M-cor}} \right)} \quad (34)$$

The contributions of all cations to the total intensity ($\sum_M I^{OX}_M$) of oxides will be:

$$\sum_M I^{OX}_M = A^{OX} \cdot \sum_M R_{MO} \cdot D^{OX}_M \cdot \lambda^{OX}_M \cdot Y^{OX}_{MO} \quad (35)$$

Finally combining **Eqs.** (**34**) and (**35**) we calculate the overall surface coverage from oxides using:

$$A^{OX} = \frac{1}{1 + \frac{\sum_M I^{met}_M}{\sum_M D^{met}_M \cdot \lambda^{met}_M \cdot Y^{met}_{M-cor}}} \Bigg/ \sum_M \frac{I^{OX}_M}{D^{OX}_M \cdot \lambda^{OX}_M \cdot Y^{OX}_{M-cor}} \quad (36)$$

In **Table 6** the total oxide surface coverage values for AstCrM are presented. values are the average of five separate analysis and the obtained curve is shown in **Fig. 56**.

Table 6. *Oxide surface coverage values for AstCrM.*

Etch depth (nm)	A^{OX}
5	69.42
7	32.77
10	11.17
20	2.95
30	1.40
50	1.22

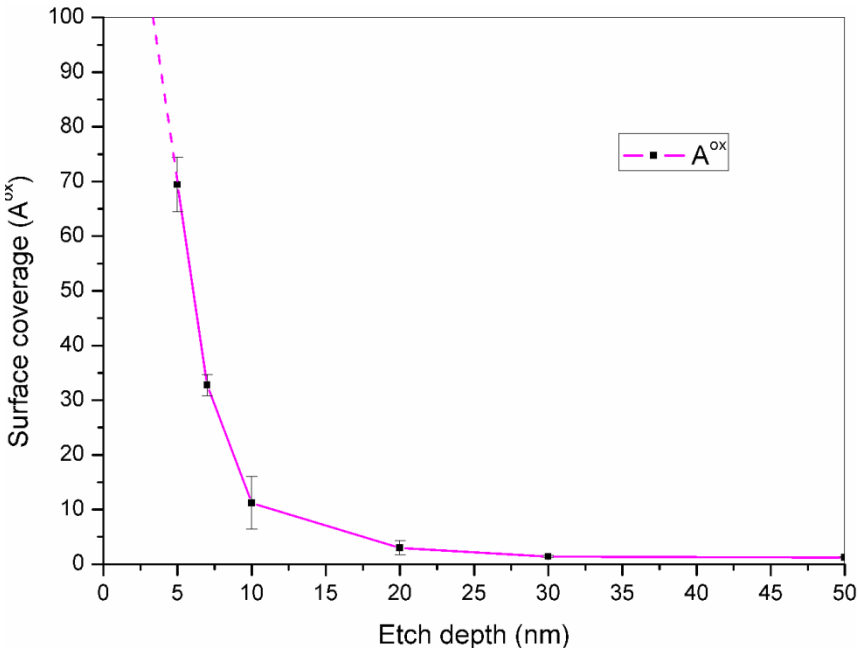

Fig. 56. *Surface coverage A^{OX} of the oxide products as a function of etch depth.*

The relative coverages of the oxides (A^{OX}_{MO}/A^{OX}) for every etch depth are given in **Table 7** and show that ~93.5% of the surface oxide is Fe_2O_3 after 1.5 nm etching. At the etch

depth of 1.5 nm, any surface carbon contamination has been removed with the slight etching that otherwise would have been necessary to account for in the calculations

Table 7. *Relative coverages of oxides for every etch depth.*

Etch depth (nm)	$R^{Fe_2O_3}$	$R^{Cr_2O_3}$	R^{MnO}
0	95.32	3.83	0.86
1.5	93.45	5.68	0.88
3	92.54	6.55	0.92
5	96.40	2.10	1.50
7	84.44	13.30	2.26
10	70.93	23.83	5.24
20	50.50	35.84	13.66
30	27.50	50.15	22.34
50	0	19.95	80.05

Appendix B – Calculation of the possible amount of $MnCr_2O_4$ spinel oxide particles inside a sinter neck

Since Cr is present underneath the surface Fe-oxide layer and its content is significant it is considered to be readily available then the possible limiting factor can be the availability of Mn which is present in the powder in low amounts (<0.1 wt.%). Therefore at first it is essential to determine the amount of Mn that could be able to be transported to the neck region. For this reason the diffusion distances of Mn in the metal phase for different temperatures and times are estimated. Similar calculations were performed for Cr as well for comparison. The data for the diffusion of Mn and Cr in austenite were taken from [99] and are presented in **Table 8**. At this point, it has to be mentioned that for this calculation, only bulk (volume) diffusion in a dislocation-free material was considered. Surface and grain boundary diffusion are significantly faster mass transport processes and especially surface diffusion should be dominant during the heating stage. Unfortunately lack of diffusion data for the case of surface diffusion of Cr and Mn in steels did not allow such calculations. Nevertheless it was assumed that if a Mn atom has reached the surface of the metal particle it would immediately move towards the neck region.

Table 8*. Diffusion coefficients of Mn and Cr in austenitic iron [99].*

	$D_{0i}\cdot10^{-5}$ ($m^2\cdot s^{-1}$)	$Q_{Di}\cdot10^{5}$ ($J\cdot mol^{-1}$)
Mn	0.55	2.495
Cr	35	2.86

Considering D_{0i} being the frequency factor and Q_{Di} being the activation energy, the expression for the temperature dependence of the diffusion coefficient (D_i) for an element is given by the expression:

$$D_i = D_{0i} \cdot exp\left(-\frac{Q_{Di}}{RT}\right) \qquad (37)$$

The calculated self-diffusion coefficients for the temperatures that are of interest for this study are given in **Table 9**.

Table 9. *Calculated diffusivities for Mn and Cr for the temperatures of interest.*

Temperature (K)	D_{Mn} ($cm^2\cdot s^{-1}$)	D_{Cr} ($cm^2\cdot s^{-1}$)
1073	$3.9\cdot10^{-14}$	$4.1\cdot10^{-14}$
1173	$4.2\cdot10^{-13}$	$6.3\cdot10^{-13}$
1273	$3.1\cdot10^{-12}$	$6.4\cdot10^{-12}$
1393	$2.4\cdot10^{-11}$	$6.5\cdot10^{-11}$
1473	$7.7\cdot10^{-11}$	$2.5\cdot10^{-10}$

The average diffusion distance (L) for a given time (t) can be estimated according to:

$$L = 2\sqrt{D_{0i}\cdot t} \qquad (38)$$

It has to be mentioned that the factor 2 in **Eq. 38** accounts for the atomic movement in one dimension which essentially means that we are underestimating the diffusion distances and consequently the considered volume, if a three dimension model is assumed then this factor must become 6 [100]. Nevertheless for the purposes of these

calculations **Eq. 38** is used and the calculated diffusion distances are given in **Table 10** for specific temperatures and times that are of interest for the purposes of this study:

Table 10. *Diffusion distance of Mn and Cr for the temperatures and times of interest.*

Temperature – time (K – min)	L_{Mn} (μm)	L_{Cr} (μm)
1073-1’	0.031	0.031
1173-1’	0.101	0.123
1273-1’	0.275	0.39
1393-1’	0.759	1.25
1393-30’	4.16	6.85
1473-30’	7.46	13.4

If now it is assumed that the metal particles are spherical with a mean diameter of 63 μm and that we consider the case of sintering at 1120°C (1393 K) for 30’ then the “effective” volume (V_{ef}) from where Mn could diffuse towards the surface is essentially the difference between the volume of the spherical metal particle (V_p) and a volume of a sphere which has a radius reduced (V_{rs}) by the diffusion distance of Mn (4.16 μm for 1120°C-30’) see **Fig. 57** and **Eq. 39** for the illustration and calculation of the “effective” volume.

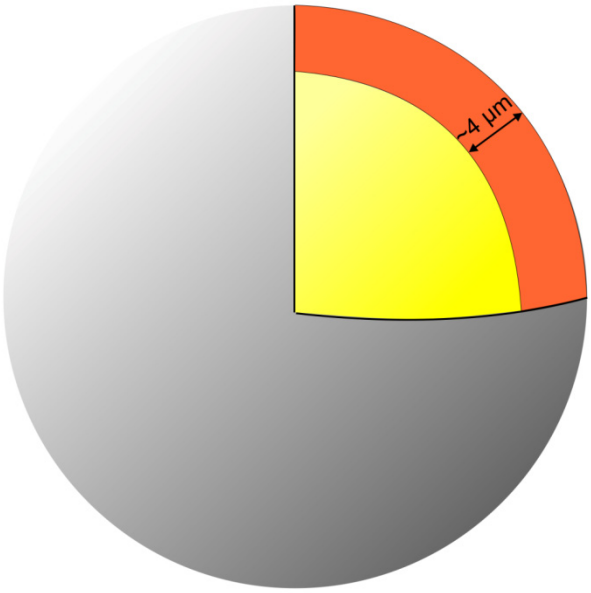

Fig. 57. *"Effective" volume (orange) from where Mn atoms can be transported to the neck region.*

$$V_{ef} = V_p - V_{rs} = \frac{4}{3}\pi\left(r_p^3 - r_{rs}^3\right) = 4.53 \cdot 10^{-8} cm^3 \qquad (39)$$

The total mass included in this “effective” volume is calculated by multiplying with the density for which only Fe was considered (ρ_{Fe}=7.87 g·cm^{-3}). Based on this estimated mass, the content of 0.1 wt.% Mn would correspond to 3.57·10^{-10} g of Mn available in the “effective” volume.

It is now assumed that each metal particle has six adjacent metal particles which of course correspond to six inter-particle necks (see **Fig. 58**). However, the mass transferred into the neck area arises from two adjacent particles (yellow arrows in **Fig. 58**). Therefore the mass calculated above is multiplied by 2/6 and thus the amount of Mn available for every neck is 1.19·10^{-10} g.

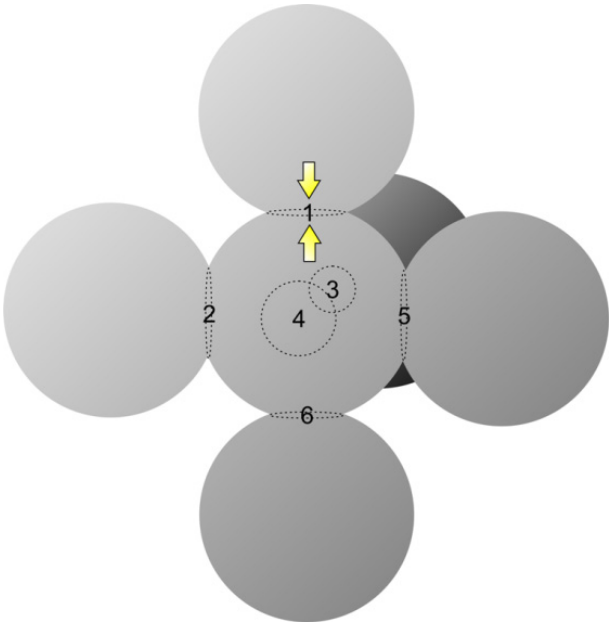

Fig. 58. *Assumed amount of contacts for a spherical metal particle in a "green body".*

Let us now assume that all the Mn that will be transferred into the neck region will form particles of $MnCr_2O_4$. This compound has molar weight of 223 $g \cdot mol^{-1}$ and theoretical density of 4.85 $g \cdot cm^{-3}$ according to [101], which in turn corresponds to a molar volume of 46 $cm^3 \cdot mol^{-1}$. The formed $MnCr_2O_4$ inclusions are considered spherical with a diameter of 0.5 μm which correspond to a volume of $6.5 \cdot 10^{-14}$ cm^3. Each spherical oxide inclusion will contain $3.15 \cdot 10^{-13}$ g of $MnCr_2O_4$ of which 24.6% is Mn. Therefore in each spherical particulate spinel oxide $0.78 \cdot 10^{-13}$ g of Mn is contained.

Finally by considering the amount of Mn required for every spherical $MnCr_2O_4$ it is estimated that the total amount of Mn available for every neck in the “effective” volume is enough to form approximately 1500 spherical particulates of $MnCr_2O_4$ of 0.5 μm in diameter. Hence, availability of Mn is not a limiting factor and then neither that of Cr is an issue considering the higher Cr-content (e.g. 3 wt%).

9 Acknowledgements

While writing these lines I realized that a trip of almost five years is actually coming to an end...or maybe not, maybe it is just a small pause before the continuation or even before a totally new beginning...I will find out soon enough! Anyhow, these five years have been full of excitements, desperation, frustration, wrong turns and getting back on track, happiness, anger, joy, fear, stresses and so many, many strong moments and feelings! I wouldn't change absolutely anything, because in the end, after drawing the "line"... it totally worth it. In this trip though I was not alone, never alone. There have been some people to whom I am deeply and sincerely grateful.

My supervisor *Prof. Lars Nyborg* who has been an endless source of knowledge, ideas and enthusiasm and gave me the chance to stand where I am right now leading me all this time through the way, as a mentor with comments, remarks and advices (even during the deep night...). Lars, I consider you as one of the brightest people I have ever met and working with you has been a huge privilege and honour.

My co-supervisor *As. Prof. Eduard Hryha* with whom we basically started together at Chalmers and with his knowledge and experience in the PM field he has been guiding me through the PM world ever since. My gratitude for his contribution to this work cannot be expressed easily. Apart from a brilliant scientist he has also been my office mate and close friend throughout all this time.

My working group from Höganäs AB: *Dr. Ola Bergman*, *Ola Litström* and *Dr. Sven Bengtsson* who first of all along with Lars, gave me this opportunity to work in PM and during this project, especially Dr. Ola Bergman who has been my industrial "alter-ego", provided excellent collaboration, many fruitful discussions and approximately 540 specimens and an equally large amount of chemical analyses and impact tests.

My colleagues and friends from the Department of Materials and Manufacturing Technology for collaboration, support. I need to thank especially *Doc. Mats Norell* for the AES analyses and the collaboration for the last article related to surface analysis as well as *Urban Jevlestam, Göran Fritze, Dick Olofsson* and for the past year *Roger Sagdahl* for their endless support in technical matters and their patience and help with issues related to experimental techniques. I am grateful to all for creating a good working atmosphere with the coffee brakes, lunches, discussions, jokes, overnight and weekend "shifts".

I also had the privilege to supervise two Spanish diploma students, *Irene de Diego Calderon* and *Elena Bernando Quejido*. Their studies on sintering have been an important part of this project and I am thankful for their contribution. I would like to believe that their work here at Chalmers had a small but important part in their careers afterwards.

This work has carried out in co-operation with *Höganäs AB* which is gratefully acknowledged for financial, technical and scientific support. *KK foundation* within the framework of *CAPE (Centre of Advanced Production Engineering)* industrial PhD school is also acknowledged for financial support.

My dear friends who in terms of distance some have been very, very close, others further away and others really far away…Nevertheless, all of you have been close and "dominated" the corner couch in the MoT during coffee time, carried "tired" people into bed and took their shoes off, came from England for just a barbeque, complained about sauna and then stayed in there for 4hrs, called in the middle of the night saying there is a strange animal in the bathroom, helped in endless movings and so many more moments which I will always cherish. If I start writing all the names I am afraid that I might forget someone…therefore, very simply, thank you all!

Sofia who has been at my side nearly from the very beginning and with extreme patience and love undertook and still does, this whole trip with me. I thought it would have been easier to express all my feelings for you with words but as you very well know, I am not very good at it, therefore I will just say that…I love you so much!

The scientist I am today I owe it to all the people related to my education and research, the person I am today though I owe it completely to my beloved family. I become very emotional when writing these lines since the people I care the most are far away and especially considering the tough times all of them are going through! My parents *Ελένη* and *Χρήστος* have given me infinite love and support and even though I know that is difficult for them as well to be far away, they are always on my side! My sister and brother *Βιολέττα* and *Αλέξανδρος* who will face more and more challenges from now on in their lives and I am sure that they will make the right choices, as the older brother I will be always here for you. My grandparents, *Δήμητρα-Μίμης* and *Βιολέττα-Δημήτρης* who even though some of them are not "present" anymore…I know that they are watching and I want them to be proud. *Όλια, Νίκο, Αναστασία, Νικήτα* and my younger cousins you always have my thoughts and love following you in every step. I wish all of you to be well and to continue loving each other so much!

It is possible that I forgot some of you…Therefore, Thank you all!!!

Dimitris Chasoglou
Göteborg, May 9th 2012

10 References

1. Schatt, W. and K.P. Wieters, *POWDER METALLURGY, Processing and Materials*. 1997, Shrewsbury, European Powder Metallurgy Association. 492.

2. *ASM Handbooks*. Classification and Designation of Carbon and Low-Alloy Steels, Properties and Selection: Irons, Steels, and High-Performance Alloys. Vol. 1. 1990, U.S.A, ASM International.

3. Bergman, O., K. Frisk, and L. Nyborg, *Analysis of Oxide Reduction during Sintering of Cr-alloyed Steel Powder through Photoacoustic Spectroscopy Measurements*, in *Euro PM2009 International Powder Metallurgy Congress and Exhibition*2009, Copenhagen, Denmark. p. 239-245.

4. Bocchini, G.F., *Influence of Controlled Atmospheres on the Proper Sintering of Carbon Steels.* Powder Metall. Prog., 2004. **4**(1): p. 1-33.

5. Chasoglou, D., E. Hryha, and L. Nyborg, *Effect of Sintering Atmosphere on the Transformation of Surface Oxides during the Sintering of Chroimum alloyed Steels.* Powder Metall. Prog., 2009. **9**(3): p. 141-155.

6. Danninger, H. and C. Gierl, *Processes in PM steel compacts during the initial stages of sintering.* Mater. Chem. Phys., 2001. **67**(1-3): p. 49-55.

7. Danninger, H., et al., *Degassing and Deoxidation Processes during Sintering of Unalloyed and Alloyed PM Steels.* Powder Metall. Prog., 2002. **2**(3): p. 125-140.

8. Fuentes-Pacheco, L. and M. Campos, *Bonding evolution with sintering temperature in low alloyed steels with chromium.* Sci Sinter, 2009. **41**(2): p. 161-173.

9. Kremel, S., H. Danninger, and Y. Yu, *Effect of Sintering Conditions on Particle Contacts and Mechanical Properties of PM Steels Prepared from 3%Cr Prealloyed Powder.* Powder Metall. Prog., 2002. **2**(4): p. 211-221.

10. Ortiz, P. and F. Castro, *Thermodynamic and experimental study of role of sintering atmospheres and graphite additions on oxide reduction in Astaloy CrM powder compacts.* Powder Metall., 2004. **47**(3): p. 291-298.

11. Beiss, P., *Sintering atmospheres for PM steels*, in *Höganäs Chair in Powder Metallurgy Workshop "Sintering Atmospheres"*1999, Vienna, Austria. p. 23.

12. Bergman, O., *Influence of oxygen partial pressure in sintering atmosphere on properties of Cr-Mo prealloyed powder metallurgy steel.* Powder Metall., 2007. **50**(3): p. 243-249.

13. Danninger, H., et al., *Chemical Reactions During Sintering of Mn and Mn-Cr Prealloyed Steels in Inert versus Reducing Atmospheres.* Mater Sci Forum, 2011. **672**: p. 203-206.

14. Hryha, E., L. Cajkova, and E. Dudrova, *Study of Reduction/Oxidation Processes in Cr-Mo Prealloyed Steels during Sintering by Continuous Atmosphere Monitoring.* Powder Metall. Prog., 2007. **7**(4): p. 181-197.

15. Hryha, E., E. Dudrova, and L. Nyborg, *On-line control of processing atmospheres for proper sintering of oxidation-sensitive PM steels.* J Mater Process Tech, 2012. **212**(4): p. 977-987.

16. Mitchell, S.C. and A. Cias, *Carbothermic Reduction of Oxides during Nitrogen Sintering of Manganese and Chromium Steels.* Powder Metall. Prog., 2004. **4**(3): p. 132-142.

17. Mosca, E., *Controlled Atmospheres in Powder Metallurgy*, in *Sintering, Theory and Practice*. 1996, EPMA, Torino, Italy. p. 97-125.

18. *ASM Handbooks*. Powder Metal Technologies and Applications. Vol. 7. 1998, ASM International.

19. German, R.M., *Powder Metallurgy Science*. 1994, Princeton, New Jersey 08540-6692, U.S.A, Metal Powder Industries Federation. 472.

20. Salak, A., *FERROUS POWDER METALLURGY*. 1995, Cambridge CB1 6AZ, England, Cambridge International Science Publishing. 453.

21. *PM2 Industry, Vision and Technology Roadmap, Powder Metallurgy and Particulate Materials*, 2001.

22. *Höganäs Handbook for Sintered Components*. 2004, Höganäs, Sweden, Höganäs AB, Sweden.

23. *Introduction to Powder Metallurgy - The Process and its Products*. 2008, Shrewsbury, U.K., European Powder Metallurgy Assocation (EPMA).

24. Tunberg, T., *Powder Surface Oxidation During Production of High Alloy PM Steels*, in *Department of Engineering Metals*1995, Chalmers University of Technology, Göteborg.

25. *ASM Specialty Handbook*. Carbon and Alloy Steels. 1996, U.S.A, ASM International.

26. Bergmark, A., J. Andersson, and S. Bengtsson, *Cromium pre-alloyed PM steel for high structural performance*, in *Euro PM2005 International Powder Metallurgy Congress and Exhibition*2005, Prague, Czech Republic.

27. Engstrom, U., et al. *Efficient Low-alloy Steels for High Performance Structural Applications*. in *PM2TEC 2005*. 2005. Montreal, Canada.

28. Frykholm, R. and O. Bergman. *Cromium pre-alloyed PM steels sutitable for high performance applications - Frykholm, Bergman*. in *PM2TEC 2005*. 2005. Montreal, Canada.

29. Lindqvist, B. and K. Kanno, *Considerations When Sintering Oxidation-Sensitive PM Steels*, in *World PM 2002: International Conference in Powder Metallurgy*2002, MPIF, Orlando, U.S.A. p. 278-290.

30. Hryha, E., E. Dudrova, and S. Bengtsson, *Influence of powder properties on compressibility of prealloyed atomised powders.* Powder Metall., 2008. **51**(4): p. 340-342.

31. Bergman, O., *Key Aspects of Sintering Powder Metallurgy Steel Prealloyed with Chromium and Manganese*, in *Department of Materials and Manufacturing Technology*2011, Chalmers University of Technology, Gothenburg.

32. Shah, S., et al. *Cr-Mo PM Steels as a Cost Effective Replacement for Traditional Ni-Mo PM Steels*. in *PM2TEC 2005*. 2005. Montreal, Canada.

33. Engstrom, U., *Influence of sintering temperature on properties of low alloyed high stregth PM materials*, in *PM2Tec 2001*2001, New Orleans, U.S.A.

34. Exner, H.E. and E. Arzt, *Chapter 31 - Sintering Processes*, in *Physical Metallurgy (Fourth Edition)*, W.C. Robert and H. Peter, Editors. 1996, North-Holland, Oxford. p. 2627-2662.

35. Ashby, M.F., *First Report on Sintering Diagrams.* Acta Metall., 1974. **22**(3): p. 275-289.

36. Ashby, M.F., et al., *The Influence of a Dispersion of Particles on the Sintering of Metal Powders and Wires.* Progress in Materials Science, 1980. **25**(1): p. 1-34.

37. Chasoglou, D., E. Hryha, and L. Nyborg, *Fractographic Investigation of Chromium-alloyed PM Steels Sintered in Atmospheres with Varying Hydrogen Content.* Powder Metall. Prog., 2011. **11**(1-2): p. 32-41.

38. Dudrova, E. and M. Kabatova, *Fractography of Sintered Iron and Steels.* Powder Metall. Prog., 2008. **8**(2): p. 59-75.

39. Hryha, E., S. Karamchedu, and L. Nyborg, *Delubrication of PM Components Based on Cr-Prealloyed Steel Powder - Chances and Risks*, in *Euro PM2011 Congress and Exhibition*2011, EPMA, Barcelona, Spain. p. 105-111.

40. Karamchedu, S., E. Hryha, and L. Nyborg, *Influence of Process Parameters on the Delubrication of PM Steels.* Powder Metall. Prog., 2011. **11**(1-2): p. 90-96.

41. *Sintering of steels*, in *Furnace atmospheres*. 2011, The Linde Group

42. Bergman, O. and L. Nyborg, *Evaluation of Sintered Properties of PM Steels based on Cr and Cr-Mn Prealloyed Steel Powders.* Powder Metall. Prog., 2010. **10**(1): p. 1-19.

43. Jaliliziyaeian, M., et al., *Fracture Surfaces Studied on PM Steels Prepared From Prealloyed Steel Powders and Sintered in Different Atmospheres.* Powder Metall. Prog., 2008. **8**(2): p. 128-134.

44. Marcu, T., et al., *Microstructure and tensile properties of 3%Cr-0-5%Mo high carbon PM sintered steels.* Powder Metall., 2005. **48**(2): p. 139-143.

45. Marcu, T., et al., *Tensile properties of vacuum-sintered dual-phase steels.* Int J Powder Metall, 2004. **40**(3): p. 57-64.

46. Bergman, O., B. Lindqvist, and S. Bengtsson, *Iinfluence of Sintering Parameters on the Mechanical Performance of PM Steels Pre-alloyed with Chromium*, in *World PM2006*2006, Busan, South Korea.

47. Chasoglou, D., E. Hryha, and L. Nyborg, *Surface Interactions During Sintering of Chromium-alloyed PM Steels in Different Atmospheres*, in *PM2010 POWDER METALLURGY World Congress & Exhibition*2010, Florence, Italy. p. 3-12.

48. Chasoglou, D., E. Hryha, and L. Nyborg, *Effect of Atmosphere Composition on the Surface Interactions during Sintering of Chromium-alloyed PM Steels*, in *Euro PM2011 Congress and Exhibition*2011, Barcelona, Spain. p. 111-117.

49. Cias, A., et al., *Tensile Properties of Fe-3Mn-0.6/0.7C Steels Sintered in Semiclosed Containers in Dry Hydrogen, Nitrogen and Mixtures thereof.* Powder Metall., 2003. **46**(2): p. 165-170.

50. Danninger, H., C. Xu, and B. Lindqvist, *Oxygen removal during sintering of steels prepared from Cr-Mo and Mo prealloyed powders.* Progress in Powder Metallurgy, Pts 1 and 2, 2007. **534-536**: p. 577-580.

51. Hrubovcakova, M. and E. Dudrova, *Influence of the Purity of the Sintering Atmosphere on the Reduction of Oxides during Sintering of Fe-Cr-Mo Steels.* Powder Metall. Prog., 2010. **10**(2): p. 71-80.

52. Hryha, E., E. Dudrova, and L. Nyborg, *Critical Aspects of Alloying of Sintered Steels with Manganese.* Metall Mater Trans A, 2010. **41A**(11): p. 2880-2897.

53. Hryha, E. and L. Nyborg, *Changes in oxide chemistry during consolidation of Cr/Mn water atomized steel powder.* Powder Metall. Prog., 2011. **11**(1-2): p. 42-50.

54. Karlsson, H., L. Nyborg, and O. Bergman, *Surface Interactions during Sintering of Water-atomised pre-alloyed Steel Powder*, in *World PM2004: World Congress and Exhibition on Powder Metallurgy* 2004, EPMA, Shrewsbury, U.K, Vienna, Austria. p. 23-28.

55. Momeni, M., C. Gierl, and H. Danninger, *Study of the oxide reduction and interstitial contents during sintering of different plain carbon steels by in situ mass spectrometry in nitrogen atmosphere.* Mater. Chem. Phys., 2011. **129**(1-2): p. 209-216.

56. Ortiz, P. and F. Castro, *Influence of carbon activity and oxygen potential of sintering atmospheres on the microstructural characteristics of low alloy P/M steels.* Thermec'2003, Pts 1-5, 2003. **426-4**: p. 4337-4342.

57. Youseffi, M., et al., *Sintering, microstructure, and mechanical properties of PM manganese-molybdenum steels.* Powder Metall., 2000. **43**(4): p. 353-358.

58. Engstrom, U., D. Milligan, and A. Klekovkin, *Mechanical Properties of High Performance Chromium Materials*, in *PowderMet 2006*2006, San Diego, U.S.A.

59. Youseffi, M., C.S. Wright, and F.M. Jeyacheya, *Effect of carbon content, sintering temperature, density, and cooling rate upon properties of prealloyed Fe-1 center dot 5Mo powder.* Powder Metall., 2000. **43**(3): p. 270-274.

60. Hrubovcakova, M. and E. Dudrova, *Effect of Green Density on Oxide Reduction during Sintering of Chromium Pre-alloyed Steel*, in *Euro PM2011 Congress and Exhibition*2011, EPMA, Barcelona, Spain. p. 69-75.

61. Karlsson, H., L. Nyborg, and S. Berg, *Surface chemical analysis of prealloyed water atomised steel powder.* Powder Metall., 2005. **48**(1): p. 51-58.

62. Chasoglou, D., E. Hryha, and L. Nyborg, *Methodology for Evaluating the Oxide Distribution in Water Atomized Steel Powder*, in *Euro PM2009 International Powder Metallurgy Congress & Exhibition*2009, EPMA, Shrewsburry, U.K, Copenhagen, Denmark. p. 181-186.

63. Chasoglou, D., E. Hryha, and L. Nyborg, *Oxide Distribution in Prealloyed Water Atomized Steel Powder*, in *PM2010 POWDER METALLURGY World Congress & Exhibition*2010, Florence, Italy. p. 61-69.

64. Hryha, E., et al., *Surface composition of the steel powders pre-alloyed with manganese.* Appl Surf Sci, 2010. **256**(12): p. 3946-3961.

65. Norell, M., et al., *Thickness Determination of Surface Oxides on Metal-Powder by Aes Depth Profiling.* Surf Interface Anal, 1992. **19**(1-12): p. 71-76.

66. Nyborg, I., T. Tunberg, and P.X. Wang, *Surface product formation during water atomization and sintering of austenitic stainless steel powder.* Met. Powder Rep., 1990. **45**(11): p. 750-753.

67. Nyborg, L., M. Norell, and I. Olefjord, *Surface Studies of Powder Metallurgical Stainless-Steel.* Surf Interface Anal, 1992. **19**(1-12): p. 607-614.

68. Nyborg, L., A. Nylund, and I. Olefjord, *Thickness determination of oxide layers on spherically-shaped metal powders by ESCA.* Surf Interface Anal, 1988. **12**(2): p. 110-114.

69. Nyborg, L. and I. Olefjord, *Surface-Analysis of Pm Martensitic Steel before and after Consolidation .1. Surface-Analysis of Powder.* Powder Metall., 1988. **31**(1): p. 33-39.

70. Olefjord, I., W. Leijon, and U. Jelvestam, *Selective Surface Oxidation during Annealing of Steel Sheets in H2/N2.* Appl. of surf. sci., 1980. **6**(3 - 4): p. 241-255.

71. Olefjord, I. and L. Nyborg, *Surface-Analysis of Gas Atomized Ferritic Steel Powder.* Powder Metall., 1985. **28**(4): p. 237-243.

72. Danninger, H., et al., *Microstructure and Mechanical-Properties of Sintered Iron .1. Basic Considerations and Review of Literature.* Powder Metall Int, 1993. **25**(3): p. 111-119.

73. *ASM Handbooks*. Fractography. Vol. 12. 1992, U.S.A, ASM International.

74. Broek, D., *Elementary Engineering Fracture Mechanics*. 1986, Dordrecht, The Netherlands, Martinus Nijhoff Publishers.

75. Schwalbe, K.-H., *On the influence of microstructure on crack propagation mechanisms and fracture toughness of metallic materials.* Engineering Fracture Mechanics, 1977. **9**(4): p. 795-832.

76. Gaskell, D., *Introduction to the Thermodynamics of Materials*. 5th ed. 2008, New York, U.S.A, Taylor & Francis Group, LLC. 618.

77. Fast, J.D., *Interaction of Metals and Gases,*. Vol. 1 - Thermodynamics and Phase Relations. 1965, Philips Technical Library.

78. Campos, M., L. Blanco, and J. Torralba, *Thermal analysis of prealloyed Fe–3Cr–0.5Mo sintered steel.* Journal of Thermal Analysis and Calorimetry, 2006. **84**(2): p. 483-487.

79. Danninger, H., et al., *Dissolution of different graphite grades during sintering of PM steels.* Mater. Chem. Phys., 2001. **67**(1-3): p. 72-77.

80. Ellingham, H.J.T., *Reducibility of Oxides and Sulphides in Metallurgical Processes.* Journal of the Society of Chemical Industry, Traansactions and Communications, 1944: p. 126-133.

81. Hryha, E. and E. Dudrova, *The sintering behaviour of Fe-Mn-C powder system, correlation between thermodynamics and sintering process, Mn distribution, and microstructure.* Progress in Powder Metallurgy, Pts 1 and 2, 2007. **534-536**: p. 761-764.

82. Danninger, H., et al., *Comparison of Mn, Cr and Mo alloyed sintered steels prepared from elemental powders.* Powder Metall., 2005. **48**(1): p. 23-32.

83. Sulowski, M., et al., *The effect of chemical composition of sintering atmosphere on the structure and mechanical properties of PM manganese steels with chromium and molybdenum additions.* Progress in Powder Metallurgy, Pts 1 and 2, 2007. **534-536**: p. 753-756.

84. *Operating Instructions Manual for Dilatometer-DIL 402C*. 2011, Germany, Netzsch.

85. Newbury, D., et al., *Advanced Scanning Electron Microscopy and X-Ray Microanalysis*. 1986, New York, U.S.A Plenum Press.

86. Norden, H. and A. Thölen, *Electron Microscopy and Microanalysis*. 1997, Gothenburg, Sweden, Department of Physics, chalmers University of Technology - Gothenburg University.

87. *Customer Training on INCA Energy*. 2000, High Wycombe, England, Oxford Istruments Analytical.

88. D., B. and S. M.P., *Practical surface analysis. Vol. 1, Auger and X-ray photoelectron spectroscopy*. 2 ed. 1990, Wiley. 657.

89. Watts, J. and J. Wolstenholme, *An Introduction to Surface Analysis by XPS and AES*. 2003, Chichester, West Sussex PO19 8SQ, England, John Wiley & Sons Ltd. 212.

90. Wagner, C.D., et al., *Handbook of X-Ray Photoelectron Spectroscopy*. 1979, U.S.A, Perkin-Elmer Corporation, Physical Electronics Division.

91. Childs, K., et al., *Handbook of Auger Electron Spectroscopy*. 3rd ed. 1995, Minesota, U.S.A, Physical Electronic Inc.

92. Bracconi, P. and L. Nyborg, *Quantitative phase analysis and thickness measurement of surface-oxide layers in metal and alloy powders by the chemical-granular method.* Appl Surf Sci, 1998. **133**(1-2): p. 129-147.

93. *Operating Instructions Manual for Simultaneous TG-DTA/DSC Apparatus-STA 449 F! Jupiter*. 2011, Germany, Netzsch.

94. Gallagher, P.K., *Chapter 4 Thermogravimetry and Thermomagnetometry*, in *Handbook of Thermal Analysis and Calorimetry*, E.B. Michael, Editor. 1998, Elsevier Science B.V. p. 225-278.

95. Mikhail, S.A. and A.H. Webster, *Chapter 13 Thermal analysis in metallurgy*, in *Handbook of Thermal Analysis and Calorimetry*, E.B. Michael and K.G. Patrick, Editors. 2003, Elsevier Science B.V. p. 657-775.

96. Van Humbeeck, J., *Chapter 11 Simultaneous Thermal Analysis*, in *Handbook of Thermal Analysis and Calorimetry*, E.B. Michael, Editor. 1998, Elsevier Science B.V. p. 497-508.

97. In-Ho, J., *Critical evaluation and thermodynamic modeling of the Mn–Cr–O system for the oxidation of SOFC interconnect.* Solid State Ionics, 2006. **177**(7–8): p. 765-777.

98. Kjellqvist, L. and M. Selleby, *Thermodynamic assessment of the Cr-Mn-O system.* J Alloy Compd, 2010. **507**(1): p. 84-92.

99. Gamsjäger, E., J. Svoboda, and F.D. Fischer, *Austenite-to-ferrite phase transformation in low-alloyed steels.* Computational Materials Science, 2005. **32**(3–4): p. 360-369.

100. Porter, D.A. and K.E. Easterling, *Phase Transformations in Metals and Alloys*. 1992, U.S.A, Taylor & Francis Group.

101. Song, S.H., Z.X. Yuan, and P. Xiao, *Electrical properties of MnCr2O4 spinel.* J Mater Sci Lett, 2003. **22**(10): p. 755-757.